PL-TR-91-2285

CHEMICAL EXPLOSIONS AND THE DISCRIMINATION PROBLEM

P. G. Richards
W. Y. Kim
D. W. Simpson
G. Ekstrom

Lamont-Doherty Geological Observatory
of Columbia University
Route 9W
Palisades, NY 10964

26 November 1991

Final Report
1 April 1990 - 30 April 1991

PHILLIPS LABORATORY
AIR FORCE SYSTEMS COMMAND
HANSCOM AIR FORCE BASE, MASSACHUSETTS 01731-5000

SPONSORED BY
Defense Advanced Research Projects Agency
Nuclear Monitoring Research Office
ARPA ORDER NO. 5307

MONITORED BY
Phillips Laboratory
Contract F19628-88-K-0041

This technical report has been reviewed and is approved for publication.

JAMES F. LEWKOWICZ
Contract Manager
Solid Earth Geophysics Branch
Earth Sciences Division

JAMES F. LEWKOWICZ
Branch Chief
Solid Earth Geophysics Branch
Earth Sciences Division

DONALD H. ECKHARDT, Director
Earth Sciences Division

This report has been reviewed by the ESD Public Affairs Office (PA) and is releasable to the National Technical Information Service (NTIS).

Qualified requestors may obtain additional copies from the Defense Technical Information Center. All others should apply to the National Technical Information Service.

If your address has changed, or if you wish to be removed from the mailing list, or if the addressee is no longer employed by your organization, please notify PL/IMA, Hanscom AFB, MA 01731-5000. This will assist us in maintaining a current mailing list.

Do not return copies of this report unless contractual obligations or notices on a specific document requires that it be returned.

REPORT DOCUMENTATION PAGE

Form Approved
OMB No. 0704-0188

1. AGENCY USE ONLY (Leave blank)	2. REPORT DATE	3. REPORT TYPE AND DATES COVERED
	26 November 1991	Final Report (1 Apr 90 - 30 Apr 91)

4. TITLE AND SUBTITLE

Chemical Explosions and the Discrimination Problem

5. FUNDING NUMBERS

PE 62714E
PR 8A10 - TDA - WUAS

Contract F19628-88-K-0041

6. AUTHOR(S)

P. G. Richards* G. Ekstrom**
W. Y. Kim*
D. W. Simpson*

7. PERFORMING ORGANIZATION NAME(S) AND ADDRESS(ES)

Lamont-Doherty Geological Observatory of Columbia Univ.
Route 9W
Palisades, NY 10964

8. PERFORMING ORGANIZATION REPORT NUMBER

9. SPONSORING/MONITORING AGENCY NAME(S) AND ADDRESS(ES)

Phillips Laboratory
Hanscom AFB, MA 01731-5000

Contract Manager: James Lewkowicz/GEH

10. SPONSORING/MONITORING AGENCY REPORT NUMBER

PL-TR-91-2285

11. SUPPLEMENTARY NOTES

* Lamont-Doherty Geological Observatory; ** Harvard University, 20 Oxford St., Cambridge, MA 02138

12a. DISTRIBUTION/AVAILABILITY STATEMENT

Approved for Public Release: Distribution Unlimited

12b. DISTRIBUTION CODE

13. ABSTRACT *(Maximum 200 words)*

This final report is in three sections:

Section one describes empirical estimates of yield and tectonic release for 71 underground nuclear explosions conducted at the Shâgan River Test Site, Kazakhstan, from 1977 to 1989. The method is based upon teleseismic observations of fundamental mode Love and Rayleigh waves at stations of the GDSN, CDSN, RSTN, and IRIS/USGS GSN. In 1977 as few as five stations were providing data, while in the late 1980's more than 25 stations were operational.

Section two makes a case for generating lists of problem events - seismic sources whose signals cannot easily be discriminated - as a mechanism for achieving three goals: (1) encouraging seismologists to contribute data that may help to discriminate events on the list; (2) training; and (3) helping to build consensus in the technical community, on what types of problem events are truly intractable with current data.

Section three describes spectral - temporal characteristics of regional seismograms and shows how they can be used to discriminate between different types of seismic sources. We analyze the high-frequency (1-40 hz) spectra of chemical explosions and earthquakes at local and regional distances to understand the seismic signal characteristics of different types of sources and to find stable discriminators. We evaluate the application of the spectrogram technique to regional seismograms in different geologic settings using data from single explosions, multiple-hole instantaneous explosions, ripple-fired quarry blasts, and earthquakes. The effects on high frequency spectra of local source and recorder site conditions and source to receiver path are also analyzed.

14. SUBJECT TERMS

Chemical explosions
Yield estimation
Discrimination

15. NUMBER OF PAGES

106

16. PRICE CODE

17. SECURITY CLASSIFICATION OF REPORT	18. SECURITY CLASSIFICATION OF THIS PAGE	19. SECURITY CLASSIFICATION OF ABSTRACT	20. LIMITATION OF ABSTRACT
Unclassified	Unclassified	Unclassified	Unclassified

Empirical measurements of yield and tectonic release in nuclear explosions from teleseismic surface waves

GÖRAN EKSTRÖM

Department of Earth and Planetary Sciences
Harvard University

PAUL G. RICHARDS

Department of Geological Sciences
Columbia University

(Version of February 25, 1992)

INTRODUCTION

For explosions and shallow earthquakes the largest amplitudes on long-period seismograms usually correspond to the arrival of fundamental mode Rayleigh and Love waves. Because of their high amplitudes and signal-to-noise ratio, these waves were early on recognized [*Richter*, 1935; *Gutenberg*, 1945] as ideal for the purpose of determining the sizes of seismic events over a wide range of magnitudes. The surface wave magnitude M_S, calculated from amplitudes of waves with approximately 20 seconds period, is often reported in global epicentral bulletins for events with $M_S = 4.5$ and even smaller, reflecting the observability of these waves at teleseismic distances.

A second quality of surface waves, in the context of earthquake quantification, is that their generation is largely insensitive to the short-period details of the time history of moment release for moderate earthquakes and explosions. High frequency and broad band teleseismic P waves, on the other hand, are dominated by frequencies around the corner frequency of the event, and are consequently more complex. The differences between shallow earthquakes and explosions in how they excite P waves and surface waves lead to a difference in the corresponding magnitudes m_b and M_S, which has been used as a robust discriminant.

Much is known about the generation and propagation of surface waves, and while M_S is a useful estimate of event size, it is an unsophisticated measure of these waves, since it ignores the effects of source geometry and propagation path. Also, the choice of where in the seismogram to make an M_S amplitude measurement is somewhat arbitrary, and no use is made of the actual wave shape or polarity. It would therefore be natural to make use of forward or inverse waveform modeling techniques to study these waves. There are several serious obstacles to this approach. First, the amplitudes of surface waves depend strongly on the depth of the event and the elastic structure near

the hypocenter, neither of which is necessarily well known. Second, the propagation of surface waves is well understood in simple media, but in realistic structures the waves will be strongly affected by focussing and defocussing, reflection, refraction, attenuation, and scattering along the path from source to receiver. All of these processes can have a large effect on the amplitudes, and to account for them correctly would require a more detailed knowledge of the elastic and anelastic structure of the crust and uppermost mantle than is available, as well as the use of sophisticated computational techniques.

We often do observe, however, that two events close to each other write very similar surface wave seismograms at distant stations. Figure 1 shows three-component seismograms for two earthquakes in central Italy (May 5, 1990, m_b=5.3; May 26, 1991, m_b=4.7) recorded at Kevo (KEV) at a distance of 30°. The similarity in the shape of the surface waves is remarkable, when the traces are shifted to account for a small difference in path length. The amplitude of surface wave generation for the second event can be measured very precisely with respect to the first event through cross-correlation. By using the first event as an 'empirical Green's function' in this fashion, we remove the complex effects of propagation observed in the surface waves, and can attribute the correlation factor to the source, either its focal mechanism, its moment, or its depth. In general, the cross-correlation between two surface wave trains will be a function of frequency when the two events have different source geometries or depths.

In this paper we develop the empirical approch, based on relative amplitude measurements of surface waves, to determine the explosive and tectonic release of moment in a set of nuclear explosions in the Shagan River portion of the former Soviet Union's nuclear test site in Kazakhstan. It has long been known that nuclear tests generate seismic waves that cannot be explained by the explosion itself (for example *Toksoz et al.* [1965]; *Aki et al.* [1969]; *Aki and Tsai* [1972]; *North and Fitch* [1982]; *Helle and Rygg* [1984]; *Massé* [1981]; *Given and Mellman* [1986]; and many others). The part of the seismic radiation that is not due to the explosive source is generally thought to be due to tectonic strain release, and different mechanisms for this strain release have been proposed. *Archambeau* [1972] argued that the strain release occurs in the fractured rock around the explosion, while *Aki and Tsai* [1972] suggest that the strain is released through triggered motion on a preexisting fault. There are no significant differences in how these mechanisms affect the radiation of surface waves at 20 seconds or greater period. While there are observations that the tectonic release sometimes occurs within one or a few seconds after the explosion [*Rygg*, 1976; *Goforth et al.*, 1982; *Day et al.*, 1987], these time differences are small in comparison with the period of the surface waves.

There have been many previous studies aimed at determining the sizes of nuclear explosions. We believe this is the first in which empirical Green's functions exclusively have been used both to calibrate wave paths and determine relative source parameters.

THEORY

To develop the simple relationships that allow us to apply the empirical approach to the study of nuclear explosions, we need to consider how surface waves are generated by shallow sources. Following *Aki and Richards* [1980], we can write, for a particular frequency ω, the vertical component of Rayleigh wave motion due to a moment tensor source M_{ij} at depth h as

$$\begin{aligned} u^R(\omega) &= \sum_n \frac{r_2(z)}{8cUI_1}\left(\frac{2}{\pi k_n r}\right)^{1/2} \exp[i(k_n r + \frac{\pi}{4})] \\ &\times \left\{k_n r_1(h)[\frac{1}{2}(\cos 2\Phi + 1)M_{xx} - \frac{1}{2}(\cos 2\Phi - 1)M_{yy} + \sin 2\Phi M_{xy}]\right. \\ &+ \left(i\left.\frac{dr_1}{dz}\right|_h - ik_n r_2(h)\right)[\cos\Phi M_{xz} + \sin\Phi M_{yz}] \\ &+ \left.\left.\frac{dr_2}{dz}\right|_h M_{zz}\right\} \end{aligned} \tag{1}$$

and similarly for the transverse component of Love wave motion

$$\begin{aligned} u^L(\omega) &= \sum_n \frac{l_1(z)}{8cUI_1}\left(\frac{2}{\pi k_n r}\right)^{1/2} \exp[i(k_n r + \frac{\pi}{4})] \\ &\times \{k_n l_1(h)[\sin 2\Phi M_{xx} - \sin 2\Phi M_{yy} - 2\cos 2\Phi M_{xy}] \\ &+ i\left.\frac{dl_1}{dz}\right|_h [\sin\Phi M_{xz} - \cos\Phi M_{yz}]\Big\} \end{aligned} \tag{2}$$

where r_1, r_2, l_1 are vertical eigenfunctions, c and U are the phase and group velocity, and I_1 is an energy integral of the particular wave type. All of these quantities depend on ω. k_n is the wavenumber of the nth mode, and in the following we shall discuss only the fundamental ($n = 0$). These expressions hold for a laterally homogeneous medium, and we will make several assumptions and approximations when applying them to real data which are affected by inhomogeneous and otherwise complex earth structure.

First, we assume that the main surface wave arrival propagates along the geometrical minor arc path between the source and the station. This enables us to use the simple angular dependence of the excitation given by equations (1) and (2). Real rays in the earth will refract and scatter in the heterogeneous structure so that significant wave energy arrives at the station along rays which leave the source in directions other than directly towards the receiver. This is true in particular for the surface wave coda, which consists mainly of scattered waves. Our assumption is testable using polarization analysis; here we guess that for most paths the assumption is valid to within 10°.

Second, we note that the surface wave excitation of the vertical dip-slip components (M_{xz}, M_{yz}) of the moment tensor is small for shallow sources, since they correspond to shear stresses that must vanish at the Earth's surface. *Given and Mellman* [1986] have shown that for a vertical dip-slip source (M_{xz} or M_{yz}) at 1 km depth, the Rayleigh wave excitation at 20 sec period is one tenth that of a similar size strike-slip (M_{xy} or $M_{xx} - M_{yy}$) source. For shallower sources and longer

periods the excitation ratio becomes even smaller. We therefore assume that the contribution of these source components to the seismograms is insignificant. This assumption is valid provided the vertical dip-slip components do not dominate the source.

Third, we observe that for very shallow sources ($h \rightarrow 0$), since the normal stresses are then small, the excitation function for the M_{zz} component can be approximated by

$$\frac{dr_2}{dz}(h) = -\frac{\alpha^2 - 2\beta^2}{\alpha^2} r_1(h) k_n \tag{3}$$

where α and β are the compressional and shear wave speeds averaged over the depth range of the emplacement shaft (see *Aki and Richards* [1980], equation (7.26)). This approximation becomes better for longer periods and shallower source depths.

We can now rewrite equations (1) and (2) as

$$u^R(t) = G^R(t) \times [\frac{1}{2}(\cos 2\Phi + 1)M_{xx} - \frac{1}{2}(\cos 2\Phi - 1)M_{yy} + \sin 2\Phi M_{xy} - \frac{\alpha^2 - 2\beta^2}{\alpha^2} M_{zz}] \tag{4}$$

and

$$u^L(t) = G^L(t) \times [\sin 2\Phi M_{xx} - \sin 2\Phi M_{yy} - 2\cos 2\Phi M_{xy}] \tag{5}$$

where $G^R(t)$ and $G^L(t)$ represent Green's functions giving the vertical Rayleigh wave motion and transverse Love wave motion due to a moment tensor source. These functions can in general be estimated given a model of the elastic and anelastic structure at and between the source and the receiver, but here we shall use an empirical approach, noting that the shape of the Green's function is the same for the four different observable components of the moment tensor and that this shape is known from the observed seismograms. What is unknown is the sign and amplitude of the function for a particular source excitation.

We will be concerned here with studying surface wave arrivals from a set of N closely clustered seismic events observed on a global network of M stations. If the Green's functions are known, we can directly reduce the observed seismogram $S^n_{lm}(t)$ to a source radiation amplitude through cross-correlation

$$C^n_{lm} = \frac{\int G^n_{lm}(t) S^n_{lm}(t) dt}{\int G^n_{lm}(t) G^n_{lm}(t) dt} \tag{6}$$

where the subscript l indicates a vertical Rayleigh wave ($l = 1$) or a transverse Love wave ($l = 2$) trace. If the N sources are close to each other, Green's functions for different events will be similar, apart from a time shift, since dispersion due to differences in path length will have a very small effect if short time windows are correlated in equation (6). We can estimate the shape of an empirical Green's function for the path between the cluster of events to the mth station by stacking several observed seismograms or by choosing one seismogram as a reference. We will use a reference seismogram $s_{lm}(t)$ scaled by an unknown factor R_{lm} as our empirical Green's function. For each individual

event observed at the mth station we can write $G^n_{lm}(t) = R_{lm} s_{lm}(t - \delta t^n_{lm})$ where δt^n_{lm} is a time delay reflecting a small difference in path length. The product $c^n_{lm} = R_{lm} C^n_{lm}$ is estimated through cross correlation between the reference seismogram $s_{lm}(t)$ and the observed seismogram $S^n_{lm}(t)$. The time shift δt^n_{lm} is determined by maximizing c^n_{lm} within reasonable *a priori* bounds on δt^n_{lm}.

Combining equations (4), (5) and (6) gives a potentially overdetermined set of equations for the source parameters and scaling of the Green's functions.

$$R_{lm} \sum_{j=1}^{3} A_{lmj} U^n_j = c^n_{lm} + \epsilon^n_{lm} \tag{7}$$

where U^n_j represents combinations of moment tensor elements for the nth explosion

$$\begin{aligned} U^n_1 &= \frac{1}{2}(M_{xx} + M_{yy}) - (\frac{\alpha^2 - 2\beta^2}{\alpha^2}) M_{zz} \\ U^n_2 &= \frac{1}{2}(M_{xx} - M_{yy}) \\ U^n_3 &= M_{xy}, \end{aligned} \tag{8}$$

the geometrical coefficients for Rayleigh waves at the mth station are

$$\begin{aligned} A_{1m1} &= 1 \\ A_{1m2} &= \cos 2\Phi_m \\ A_{1m3} &= \sin 2\Phi_m \end{aligned} \tag{9}$$

and for Love waves at the mth station

$$\begin{aligned} A_{2m1} &= 0 \\ A_{2m2} &= \sin 2\Phi_m \\ A_{2m3} &= -\cos 2\Phi_m \end{aligned} \tag{10}$$

and ϵ^n_{lm} is the misfit between observation and model. Each event is in general not recorded by more than a subset of the M stations so the total number of equations is less than $2MN$.

A solution to this set of equations is obtained by minimizing the misfit between the model and the observed correlations

$$\Phi(R_{lm}, U^n_j) = \sum_{l=1}^{2} \sum_{m=1}^{M} \sum_{n=1}^{N} \epsilon^n_{lm} \epsilon^n_{lm} \tag{11}$$

It is clear that, as stated, the problem has a trivial solution with all R_{lm} and all U^n_j equal to zero. This results from our having formulated the problem entirely in terms of relative measurements. We remove this ambiguity by fixing one R_m to be unity. The other path and source parameters then scale directly with this one parameter. There is a remaining scaling ambiguity which we can resolve only by introducing some additional information about one or several source parameters. It can also

be shown that if all sources have the same excitation ratios, that is if U_1^n/U_2^n, U_1^n/U_3^n, or U_2^n/U_3^n is constant for all events n, equation (7) will not have a unique solution.

For each event, we can estimate only 3 combinations of 6 moment tensor elements. This ambiguity is a direct consequence of the approximations that we made for the shallow source depth and frequency content of our observations. In particular, there is no possibility of determining the isotropic component ($M_{xx} = M_{yy} = M_{zz}$) of the source independently from a vertically oriented compensated linear vector dipole source, ($M_{xx} = M_{yy} = -\frac{1}{2}M_{zz}$), since both these combinations contribute only to U_1. In order to interpret the U_j^n in terms of an isotropic and a deviatoric moment tensor, we therefore have to introduce additional assumptions. We will assume that the total moment tensor $\mathbf{M}$ is a sum of the explosion described by an isotropic source $M_I = \frac{1}{3}(M_{xx}+M_{yy}+M_{zz})$, and tectonic release described by a double-couple source $\mathbf{M}_{DC}$, corresponding to a shear dislocation with strike Φ_S, dip δ, rake λ, and moment M_0. Using relationships given by *Aki and Richards* [1980, page 117] we find that

$$U_1 = \frac{1}{2}(M_{xx} + M_{yy}) - \frac{\alpha^2 - 2\beta^2}{\alpha^2}M_{zz} = \frac{2\beta^2}{\alpha^2}M_I - \frac{3\alpha^2 - 4\beta^2}{2\alpha^2}M_0 \sin 2\delta \sin\lambda \tag{12}$$

$$U_2 = -M_0(\sin\delta\cos\lambda\sin 2\Phi_S - \frac{1}{2}\sin 2\delta \sin\lambda \cos 2\Phi_S) \tag{13}$$

$$U_3 = M_0(\sin\delta\cos\lambda\cos 2\Phi_S + \frac{1}{2}\sin 2\delta \sin\lambda \sin 2\Phi_S). \tag{14}$$

It is clear from equation (12) that M_I is maximized assuming a fixed value of M_0 if $\sin 2\delta = \sin\lambda = 1$, that is for a pure thrust with $\delta = \pi/4$ and $\lambda = \pi/2$. There is no *a priori* reason why the maximum possible value of M_I consistent with U_1, U_2, U_3 should be consistent with a pure thrust, since all of $(\Phi_s, \delta, \lambda, M_0)$ may be varied. Nevertheless, the result is true, but the maximum M_I can also be derived from other combinations of δ and M_0 and the key variable affecting M_I is Φ_S. To see this, note that

$$U_2\cos 2\Phi_S + U_3 \sin 2\Phi_S = \frac{1}{2}M_0 \sin 2\delta \sin\lambda \tag{15}$$

and

$$U_2 \sin 2\Phi_S - U_3 \cos 2\Phi_S = -M_0 \sin\delta\cos\lambda \tag{16}$$

which can be rewritten as

$$U_2\cos 2\Phi_S + U_3 \sin 2\Phi_S = \sqrt{U_2^2 + U_3^2}\cos[2(\Phi_S - \Phi_U)] = \frac{1}{2}M_0 \sin 2\delta \sin\lambda \tag{17}$$

$$U_2 \sin 2\Phi_S - U_3 \cos 2\Phi_S = \sqrt{U_2^2 + U_3^2}\sin[2(\Phi_S - \Phi_U)] = -M_0 \sin\delta\cos\lambda \tag{18}$$

where the angle Φ_U is determined from the observations by $\tan 2\Phi_U = U_3/U_2$. It follows then that

$$M_I = \frac{\alpha^2}{2\beta^2} U_1 + \left(\frac{3\alpha^2}{2\beta^2} - 2\right) \sqrt{U_2^2 + U_3^2} \cos[2(\Phi_S - \Phi_U)]. \quad (19)$$

To maximize M_I we must require $\Phi_S = \Phi_U$. Then $\lambda = \pi/2$ and $M_0 \sin 2\delta = 2\sqrt{U_2^2 + U_3^2}$. These choices describe a pure thrust with fixed strike, but various combinations of M_0 and δ will satisfy the last equality, all leading to the same maximum value of M_I. Of these combinations, that with $\delta = \pi/4$ will be associated with the least M_0.

DATA

We studied all seismic events in the Shagan River portion of the Soviet nuclear test site in eastern Kazakhstan since 1977 listed in the ISC (1977–August 1987) and PDE (September 1987–1990) bulletins. Two hours of long-period data were collected for all stations and channels available on the day of a particular event. The data were extracted from the Harvard Seismic Archive Facility which contains data from the GDSN, CDSN, RSTN, and IRIS/USGS GSN networks. In 1977 as few as five stations were providing data, while in the late 80's more than 25 stations were operational. Seismograms from 78 events were collected.

As a first step, all seismograms were normalized to the same instrument response, and rotated into vertical, longitudinal, and transverse components. The response chosen for the analysis consists of an 8-pole Butterworth lowpass filter with a corner at 18 seconds and a 4-pole Bessel highpass filter with a corner at 60 seconds. A relatively sharp corner at the high end of the passband is needed to remain within the original passband of the SRO and ASRO instruments while at the same time benefiting from the higher signal-to-noise ratio at around 20–25 seconds period. The details of the filtering do not significantly influence the results.

An initial viewing was made of all events recorded at a particular station. For each station, one vertical and one transverse component seismogram with high signal-to-noise ratio were selected as reference seismograms. A number of stations were discarded when the data appeared to be too noisy for analysis for all of the events. Vertical Rayleigh wave reference seismograms were selected for 29 stations and transverse Love wave reference seismograms for 18 stations (Figure 2).

The correlation coefficients (c_{lm}^n) were calculated by systematically processing all events recorded on the vertical or transverse component at a particular station. Figure 3 shows an example of the correlation procedure for one explosion. A time window was selected, approximately 100 sec long, in which the correlation between the traces was calculated. The selection of this window is governed mostly by the arrival of the highest amplitude portion of the surface wave train. The correlation processing is interactive, allowing for modifications of the window when the data in the initial window is noisy or disrupted by glitches or other problems.

In order to estimate the uncertainty in our derived source parameters, we assign standard deviations σ_{lm}^n to each data point c_{lm}^n. Our assumption is that the error is primarily due to the specific

choice of correlation window and that this error is proportional to the value of the measurement. That is, we have a contribution ${}^{(1)}\sigma^n_{lm} = fc^n_{lm}$, where f is a factor assigned by visually evaluating the quality of correlation of the two waveforms. We use four classes of quality of fit: 'A' indicates an estimated uncertainty f in c^n_{lm} of 10%, 'B' 20%, and 'C' 40%. Data points which are questionable due to a suspicion of some malfunction of the instrument (mostly polarity reversals and multiplexing errors) are kept but given a quality label 'S', and are not used in the inversion. Using only proportional errors ${}^{(1)}\sigma^n_{lm}$ would lead to an emphasis on fitting small amplitudes at nodal stations. While nodal observations are important for constraining the radiation pattern, they are also most affected by deviations from the assumption that the surface waves travel along great circle paths. We attempt to account for this source of error by adding a second term ${}^{(2)}\sigma^n_l$ which is the average of ${}^{(1)}\sigma^n_{lm}$ for a particular event calculated from all records that are used in the inversion. The total *a priori* error in each data point is thus ${}^{(1)}\sigma^n_{lm} + {}^{(2)}\sigma^n_l$.

The time shift δt^n_{lm} is determined by calculating the correlation for different time shifts between the observed and reference waveforms. An expected timeshift is estimated by calculating the delay caused by the difference in epicentral distance between the reference event and the current event. An optimal δt^n_{lm} is sought within 5 sec of this predicted value.

RESULTS

Equation (11) was solved by minimizing $\Phi(R_{lm}, U^n_j)$ with respect to $R_{lm}, l = 1, 2; m = 1, \ldots, M$ and $U^n_j, j = 1, 2, 3; n = 1, \ldots, N$. Our approach was to search for the global minimum by generating random perturbations in the R_{lm} and then calculating the total misfit $\Phi(R_{lm}, U^n_j)$ by solving equation (7) in a least squares sense for each individual event, and summing the total misfit. When the random perturbation leads to an improved fit, the path parameters are updated, and new perturbations are generated. Due to our assignment of data variances, each observation contributes approximately an equal amount to the overall misfit.

The result of the minimization is a set of path parameters and source parameters for 71 events (Table 1). Seven events of the 78 had fewer than 6 observations, and we did not calculate source parameters for these. Included in Table 1 are the standard uncertainties in U^n_1, U^n_2, and U^n_3, as well as the resulting goodness of fit parameter $Q(\nu/2, \chi^2/2)$ where ν is the number of degrees of freedom (*number of stations* - 3 *source parameters*) and χ^2 is the sum of squared errors normalized to unit variance.

We can also evaluate the quality of the results by comparing the radiation amplitudes $C^n_{lm} = c^n_{lm}/R_m$ with the predicted radiation patterns $\sum_{j=1}^{3} A_{lmj} U^n_j$. Figure 4*a*–*f* show examples for several different events.

The next step is to interpret the results in terms of an explosive and tectonic component using equation (19) and assuming the geometry which maximizes M_I and minimizes M_0. In order to use

equation (19), we need to know the relative wave excitation of $M_{xx} + M_{yy}$ compared with that of M_{zz}, which depends on the compressional and shear velocities at the source. We will use the values assumed by *Given and Mellman* [1986] for the Shagan test site, $\alpha = 5.0$ km/sec and $\beta = 2.7$km/sec.

We calculate uncertainties in our derived parameters (M_I^{max}, M_0^{min}, and Φ_S) by generating a large number of realizations of the source parameters (U_1, U_2, U_3) assuming normal distributions of these with the variances listed in Table 1. We then calculate the mean and variance of the derived parameters and present the range corresponding to the one-sigma distribution.

In order to scale our results in terms of moment release or explosive yield, we need to introduce one or several known source parameters in the calculation. We shall use the yield of the Joint Verification Experiment (JVE) performed at the Shagan River test site on September 14, 1988, for which we have excellent data. The yield of this explosion was carefully measured by the Soviet Union and the U.S. using on site techniques (CORRTEX). The actual measurements are known to the two governments, but remain classified. The agreement was that the yield of the JVE explosion was to be between 100 and 150 kT. *New York Times* [1988] stated that the American and Soviet measurements were 115 and 122 kT, and we will here use the average of these two unconfirmed values, 118.5 kT, as our calibration point for all other explosions that we have studied. If and when a more authoritative yield is made available, our yield estimates may be scaled up or down slightly, using the new information. Note that in our calculations we assume that 118.5 kT corresponds to the maximum isotropic moment release (M_I^{max}) for the JVE.

Table 2 shows our results. We do not have any direct way of scaling the yield with moment, so we list the yields Y and the equivalent quantity for the shear dislocation Y_S.

DISCUSSION

Figure 5 shows our calculated yields over the time period that we have considered. Only one event (030487) is estimated to have a yield greater than 150 kT in our analysis. A large number of explosions have yields very similar to that of the JVE. *Given and Mellman* [1986] analyzed a subset of the explosions in our study using similar data and a technique based on cross-correlation with synthetic seismograms. The results of that study were presented in terms of moments (since a calibration event was not available) and Figure 6 shows a comparison of the yields determined in this study with those moments. The agreement is very good, which shows that the two methods of calibrating the paths and estimating the source parameters U_1, U_2, U_3 are robust. For many events we used a larger number of stations than *Given and Mellman*, but most of the data are the same in the two studies. We can also compare the F-ratio (here we use the definition $F = M_0/M_I$) obtained in the two studies in Figure 7, which again are very similar. There is a systematic difference between the two studies in the strike of the thrust fault (Figure 8). We believe this is due to a different choice of 'normal Love wave polarity' for one of the stations in *Given and Mellman*'s study. We found that

the addition of the CDSN stations for later events allowed us to constrain the strike of the radiation pattern better for all events.

While the results of these two surface wave studies correlate very well, neither correlates particularly well with other estimates of explosive yield. Figure 9 shows a comparison between $\log Y$ and $m_b(Lg)$ calculated by *Ringdahl and Marshall* [1989]. The scatter is very large. Similarly, if we compare the $\log Y$ with carefully measured $m_b(P)$ [*Ringdahl and Marshall*, 1989], the scatter is also large (Figure 10). On the other hand, if we compare the scatter between $m_b(Lg)$ and $m_b(P)$ from *Ringdahl and Marshall* [1989] for events that are common to our study, we get a much better correlation (Figure 11).

If we accept that $m_b(Lg)$ is a good measure of explosive yield, we must seek an explanation to why our analysis yields poorer results. We argue that it is improbable that the large discrepancies arises from some errors in the determination of the radiation amplitudes L_1, L_2, L_3. The data points C_{lm}^n are well fit by the source models (Figure 4), and the agreement with the results of *Given and Mellman* [1986] is very good. A more likely source of error is in the mapping of the radiation amplitudes into an isotropic and a double-couple component.

One possibility is that the assumption of a double-couple type mechanism for the tectonic release is incorrect. There is no reason why slip on just one single fault should be triggered by the explosion [*Aki et al.*, 1969; *Aki and Tsai*, 1972; *Wallace et al.*, 1983], and if two faults of different orientations experience slip, the summed moment tensor will in general not be a double-couple, even though the trace of the tensor will be zero. Similarly, the shattering model for tectonic release [*Archambeau*, 1972; *Stevens*, 1980; *Day et al.*, 1987] contains no physical requirement for the strain release to have double-couple geometry. In fact, *Day et al.* [1987] present the result

$$M_{ij} = \sigma_{ij} R^3 \frac{20\pi\alpha^2}{9\alpha^2 - 4\beta^2}$$

for the deviatoric moment tensor due to stress relaxation in a rock with prestress σ_{ij} in a shattered zone of radius R. In the context of this model there are good reasons not to expect σ_{ij} to have a double-couple geometry.

REFERENCES

Aki, K., and P. G. Richards, Quantitative Seismology: Theory and methods, W. H. Freeman, San Francisco, 1980.

Aki, K., P. Reasonberg, T. De Fazio, and Y. B. Tsai, Near-field and far-field seismic evidence for triggering of an earthquake by the Benham explosion, *Bull. Seism. Soc. Am. 59*, 2197–2207, 1969.

Aki, K., and Y. Tsai, The mechanism of Love wave excitation by explosive sources, *J. Geophys. Res.*, 77, 1452. 1972.

Archambeau, C. B., The theory pf stress wave radiation from explosions in prestressed media, *Geophys. J. R. Astron. Soc., 29*, 329–366, 1972.

Day, S. M., T Cherry, N. Rimer, and J. L. Stevens, Nonlinear model of tectonic release from underground explosions, *Bull. Seism. Soc. Am.*, 77, 996–1016, 1987.

Given, J. W., and G. R. Mellman, Estimating explosions and tectonic source parameters of underground nuclear explosions from Rayleigh and Love wave observations, Final Report–Part 1, AFGL-TR-86-0171(I), 79 pages, 1986, ADB110040.

Goforth, T., B. Rafipour, and E. Herrin, Anomalous Rayleigh waves from nuclear explosions in the USSR Shagan River test site, in AFOSR Semiannual Technical Report edited by E. Herrin and T Goforth, Geophysical Laboratory, Southern Methodist University, 1982.

Gutenberg, B., Amplitudes of surface waves and magnitudes of shallow earthquakes, *Bull. Seism. Soc. Am., 35*, 3–12, 1945.

Helle, H. B., and E. Rygg, Determination of tectonic release from surface waves generated by nuclear explosions in Eastern Kazakhstan, *Bull. Seism. Soc. Am., 74*, 1883–1898, 1984.

Leith, W., Tectonics of Eastern Kazakhstan and implications for seismic source studies in the Shagan River area, manuscript prepared for DARPA/AFGL Seismic Research Symposium, June 15–18, 1987, GL-TR-90-0300, ADA229025.

Massé, R. P., Review of seismic source models for underground nuclear explosions, *Bull. Seism. Soc. Am., 71*, 1249–1268, 1981.

New York Times, article by M. R. Gordon, October 30, **137**, page A15, 1988.

North R. G., and T. J. Fitch, Surface wave generation by underground nuclear explosions, Semiannual Technical Summary, March 31, No. ESD-TR-81-84 (Lincoln Laboratory, MIT, Cambridge, Mass.), 47-55 ADA109/84, 1982.

Richter, C. F., An instrumental earthquake magnitude scale, *Bull. Seism. Soc. Am., 25*, 1–32, 1935.

Ringdahl, F., and P. D. Marshall, Yield determination of Soviet underground nuclear explosions at the Shagan River Test Site. in NORSAR Semiannual Technical Summary, 1 October 1988–31

March 1989, NORSAR Sci. Rept. 2-88/89, NTNF/NORSAR, Kjeller, Norway, 1989.

Rygg, E., 1979, Anomalous surface waves from underground explosions, *Bull. Seism. Soc. Am., 69*, 1995-2000, 1979.

Stevens, J. L, Seismic radiation from the sudden creation of a spherical cavity in an arbitrarily prestressed elastic medium, *Geophys. J. R. Astron. Soc., 61*, 303-328, 1980.

Toksoz, M. N., A. Ben-Menahem, and D. G. Harkrider, Determination of source parameters of explosions and earthquakes aby amplitude equalization of seismic surface waves; release of tectonic strain by underground nuclear explosions and mechanisms of earthquakes, *J. Geophys. Res., 70*, 907–922, 1965

Toksoz, M. N., and H. H. Kehrer, Tectonic strain release by underground nuclear explosions and its effect on seismic discrimination, *Geophys. J. R. Astron. Soc., 31*, 141-161, 1972.

Wallace, T. C., D. V. Helmberger, and G. R. Engen, Evidence for tectonic release from underground nuclear explosions in long-period *P*-waves, *Bull. Seism. Soc. Am., 73*, 593-613, 1983.

FIGURE CAPTIONS

Figure 1. Similarity of surface waves from two earthquakes in central Italy recorded at KEV in Finland. Traces 1, 3, and 5 from the top show transverse, longitudinal, and vertical components of motion for the May 5, 1990 ($m_b = 5.3$) event. Traces 2, 4, and 6 show the corresponding traces for the May 26, 1990 ($m_b = 4.7$) event. Time-shifted and scaled copies of traces 1, 3, and 5 are plotted on top of 2, 4, and 6, showing the great similarity of the waveforms. The three numbers on the left show the scaling factor, expected delay, and delay that maximizes the correlation between the two traces in each pair. The expected delay contains a time offset between origin times, as well as a difference in path length.

Figure 2. Azimuthally equidistant projection centered on the Kazakstan test site, showing the distribution of stations used in the analysis.

Figure 3. Correlation of seismograms for the JVE with the reference seismograms for KONO. The reference seismograms correspond to the event 091480.

Figure 4*a–f*. Comparison of observed and predicted radiation amplitudes for Rayleigh (left circle) and Love (right circle) waves for different explosions. The solid lines and symbols correspond to positive amplitudes, and the radial distance is proportional to the absolute value of the radiation amplitude.

Figure 5. Yields calculated assuming a tectonic component to the moment release that maximizes the isotropic contribution to U_1.

Figure 6. Comparison of the maximum yields determined in this study (E & R) with the maximum isotropic moment release from *Mellman and Given* [1986] for events analyzed in both studies.

Figure 7. Comparison of F-ratios determined by *Mellman and Given* [1986] and in this study. The thin line corresponds to $F_{\mathrm{E\ \&\ R}} = F_{\mathrm{M\ \&\ G}}$.

Figure 8. Comparison of strikes determined by *Mellman and Given* [1986] and in this study. The thin line corresponds to $\Phi_{\mathrm{E\ \&\ R}} = \Phi_{\mathrm{M\ \&\ G}}$.

Figure 9. Comparison between $\log Y_I$ and $m_b(Lg)$ [*Ringdahl and Marshall*, 1989].

Figure 10. Comparison between $\log Y_I$ and $m_b(P)$ [*Ringdahl and Marshall*, 1989].

Figure 11. Comparison between $m_b(Lg)$ and $m_b(P)$ (both from *Ringdahl and Marshall* [1989]) for events also analyzed in this study.

TABLE 1. Basic Source Parameters

Event	U_1	σ_1	U_2	σ_2	U_3	σ_3	N	Q
052977	0.000	0.000	0.000	0.000	0.000	0.000	0	0.00000000
062977	0.000	0.000	0.000	0.000	0.000	0.000	0	0.00000000
090577	-0.269	0.027	-0.070	0.012	-0.159	0.019	5	0.00005800
102977	-0.262	0.040	0.073	0.022	-0.220	0.018	5	0.05351200
113077	0.161	0.060	0.034	0.009	-0.220	0.018	5	0.10075701
061178	0.547	0.042	0.031	0.027	-0.118	0.028	6	0.00000000
070578	0.031	0.036	-0.146	0.040	-0.240	0.023	6	0.59067899
082978	0.025	0.023	0.040	0.010	-0.340	0.016	9	0.02128600
091578	0.482	0.023	0.021	0.021	-0.252	0.016	10	0.62344003
110478	0.013	0.019	0.042	0.009	-0.384	0.017	16	0.00024200
112978	0.454	0.021	0.074	0.010	-0.232	0.012	13	0.00000000
020179	-0.028	0.008	0.024	0.005	-0.073	0.006	7	0.36685500
062379	0.380	0.024	0.048	0.013	-0.657	0.022	15	0.00000000
070779	-1.003	0.040	0.127	0.022	-0.967	0.043	12	0.00269500
080479	0.752	0.029	-0.047	0.015	-0.487	0.019	15	0.08128100
081879	-0.189	0.022	0.071	0.009	-0.495	0.017	14	0.00000700
102879	0.675	0.030	0.250	0.022	-0.339	0.020	12	0.07061400
120279	0.861	0.038	-0.053	0.010	-0.177	0.015	13	0.05556000
122379	0.368	0.023	-0.016	0.004	-0.205	0.011	16	0.00854600
042580	0.000	0.000	0.000	0.000	0.000	0.000	0	0.00000000
061280	0.119	0.011	0.030	0.005	-0.057	0.012	9	0.17675000
062980	0.148	0.009	0.044	0.005	-0.114	0.008	12	0.03994500
091480	0.059	0.034	0.081	0.013	-0.942	0.028	16	0.00000000
101280	0.702	0.028	0.056	0.010	-0.324	0.017	16	0.20800100
121480	0.419	0.018	-0.095	0.010	-0.326	0.013	15	0.00000400
122780	-0.385	0.022	0.051	0.015	-0.283	0.017	12	0.00000000
032981	-0.013	0.016	0.065	0.006	-0.251	0.012	12	0.12657800
042281	0.664	0.036	-0.039	0.012	-0.256	0.015	13	0.52612001
052781	0.037	0.012	-0.013	0.012	-0.036	0.009	8	0.00376300
091381	0.813	0.050	-0.019	0.018	-0.463	0.033	10	0.33089301
101881	0.631	0.042	0.067	0.012	-0.380	0.032	11	0.96205199
112981	0.335	0.026	-0.002	0.018	-0.124	0.021	12	0.30346000
122781	0.599	0.035	0.092	0.009	-0.447	0.020	15	0.36194301
042582	0.549	0.033	0.062	0.008	-0.279	0.018	18	0.00000000
070482	0.000	0.000	0.000	0.000	0.000	0.000	0	0.00000000
083182	0.192	0.031	0.021	0.029	-0.028	0.032	7	0.80144000
120582	0.396	0.024	0.015	0.009	-0.433	0.024	17	0.00000000
122682	-0.096	0.047	-0.009	0.033	-0.242	0.023	5	0.00403600
061283	1.023	0.038	0.111	0.015	-0.311	0.025	25	0.45291600
100683	0.958	0.033	-0.230	0.030	0.000	0.042	16	0.00001900

TABLE 1. (Continued)

Event	U_1	σ_1	U_2	σ_2	U_3	σ_3	N	Q
102683	0.724	0.029	0.066	0.020	-0.560	0.037	17	0.08013000
112083	0.000	0.000	0.000	0.000	0.000	0.000	0	0.00000000
021984	0.662	0.031	-0.093	0.016	-0.031	0.033	15	0.10896600
030784	0.142	0.013	-0.002	0.007	-0.179	0.013	14	0.13940200
032984	0.501	0.023	-0.062	0.016	-0.235	0.022	15	0.95793599
042584	0.974	0.045	0.224	0.028	-0.021	0.024	15	0.02877900
052684	0.000	0.000	0.000	0.000	0.000	0.000	0	0.00000000
071484	0.889	0.033	0.065	0.010	-0.391	0.021	26	0.10892400
091584	0.000	0.000	0.000	0.000	0.000	0.000	0	0.00000000
102784	0.604	0.025	0.096	0.010	-0.416	0.020	23	0.00000000
120284	-0.085	0.022	0.262	0.018	-0.412	0.022	19	0.00111400
121684	0.906	0.032	0.103	0.014	-0.493	0.023	21	0.16487600
122884	0.555	0.021	-0.081	0.008	-0.027	0.011	19	0.00000000
021085	0.817	0.033	0.008	0.015	-0.305	0.025	17	0.29335600
042585	0.497	0.025	0.032	0.018	-0.154	0.021	15	0.00001300
061585	0.376	0.016	-0.046	0.011	-0.226	0.017	20	0.00241600
063085	0.484	0.019	0.071	0.009	-0.339	0.020	19	0.11962500
072085	0.361	0.015	0.065	0.008	-0.290	0.016	23	0.33539200
031287	0.295	0.017	0.013	0.003	-0.069	0.012	17	0.65851299
040387	1.316	0.045	0.059	0.009	-0.503	0.027	26	0.40051001
041787	0.340	0.031	0.022	0.009	-0.452	0.027	18	0.76965803
062087	0.441	0.016	-0.043	0.007	-0.139	0.010	21	0.00000000
080287	0.429	0.020	-0.050	0.007	-0.313	0.017	19	0.00000000
111587	1.161	0.036	0.032	0.015	-0.227	0.011	21	0.12543100
121387	0.742	0.025	0.051	0.005	-0.422	0.018	24	0.86127001
122787	0.423	0.020	0.018	0.008	-0.343	0.018	20	0.00538200
021388	0.763	0.023	0.103	0.007	-0.229	0.009	29	0.00000000
040388	0.776	0.025	0.018	0.005	-0.366	0.015	29	0.01296700
050488	0.735	0.061	0.083	0.010	-0.472	0.061	10	0.05958800
061488	0.035	0.004	0.006	0.003	-0.018	0.004	9	0.01227800
091488	0.917	0.028	0.073	0.006	-0.319	0.014	29	0.00890300
111288	0.027	0.012	-0.006	0.001	-0.100	0.010	11	0.00000000
121788	0.627	0.023	0.085	0.009	-0.565	0.026	18	0.05963600
012289	0.870	0.031	0.029	0.005	-0.298	0.015	21	0.00045500
021289	0.900	0.037	0.004	0.012	-0.072	0.032	20	0.00001000
070889	0.306	0.012	0.055	0.003	-0.113	0.007	27	0.00000000
090289	0.118	0.006	0.008	0.002	-0.063	0.006	14	0.30166599
101989	1.074	0.032	0.071	0.011	-0.081	0.018	24	0.00000000

TABLE 2. Source Parameters

Event	Y	Y^{min}	Y^{max}	F	F^{min}	F^{max}	Φ_S	Φ_S^{min}	Φ_S^{max}	$m_{b(Lg)}$	$m_{b(P)}$
052977											5.750
062977											5.200
090577	3.9	0.8	7.4	4.09	-287.39	316.41	-57.00	-59.20	-54.80	5.870	5.730
102977	12.7	8.5	17.1	1.66	-2.04	6.08	-35.80	-38.50	-33.10	5.750	5.560
113077	44.5	38.9	49.7	0.46	0.41	0.51	-40.60	-41.80	-39.20	5.750	5.890
061178	60.2	55.6	65.8	0.18	0.16	0.22	-37.50	-44.10	-30.70	5.750	5.830
070578	42.7	38.4	48.2	0.60	0.56	0.64	-60.70	-63.90	-56.70	5.790	5.770
082978	51.0	48.0	53.8	0.61	0.59	0.63	-41.60	-42.40	-40.80	6.010	5.900
091578	73.8	71.0	77.0	0.31	0.30	0.32	-42.70	-45.00	-40.20	5.900	5.890
110478	56.4	53.4	59.2	0.62	0.61	0.65	-41.90	-42.60	-41.20	5.690	5.560
112978	70.3	68.1	72.7	0.32	0.31	0.33	-36.10	-37.40	-35.00	5.970	5.960
020179	8.7	7.7	9.7	0.80	0.74	0.86	-35.90	-37.70	-34.10	0.000	5.290
062379	124.1	120.6	128.0	0.48	0.47	0.49	-42.90	-43.50	-42.30	6.060	6.160
070779	61.4	54.8	68.0	1.45	1.35	1.57	-41.30	-41.90	-40.50	5.960	5.840
080179	128.9	125.2	132.4	0.35	0.34	0.36	-47.80	-48.70	-46.90	6.100	6.130
081879	56.8	53.9	59.7	0.80	0.78	0.82	-40.90	-41.40	-40.40	6.120	6.130
102879	113.0	109.3	116.9	0.34	0.33	0.35	-26.80	-28.30	-25.30	6.050	5.980
120279	93.8	90.2	97.4	0.18	0.17	0.19	-53.20	-55.00	-51.60	5.920	5.[illegible]
122379	58.2	55.6	60.6	0.32	0.31	0.33	-47.30	-47.80	-46.80	6.030	6.130
042580											5.450
061280	18.4	16.7	20.1	0.32	0.29	0.35	-31.10	-31.10	-27.50	5.620	5.520
062980	29.0	27.8	30.4	0.38	0.37	0.39	-34.60	-35.90	-33.10	5.700	5.690
091480	140.0	135.2	144.6	0.62	0.61	0.63	-42.50	-42.90	-42.10	0.000	6.210
101280	101.9	98.8	105.0	0.29	0.28	0.30	-40.10	-41.00	-39.20	5.920	5.880
121480	81.4	79.0	83.6	0.38	0.37	0.39	-53.10	-53.90	-52.10	5.930	5.930
122780	11.1	8.3	14.1	2.36	1.72	3.32	-39.90	-41.30	-38.30	5.930	5.870
032981	36.2	34.2	38.2	0.65	0.64	0.68	-37.80	-38.60	-37.00	5.540	5.490
042281	89.0	85.9	92.7	0.27	0.26	0.28	-49.30	-50.70	-47.90	5.920	5.490
052781	8.4	7.1	10.3	0.42	0.37	0.49	-55.00	-63.50	-45.70	5.450	5.300
091381	129.8	123.6	136.0	0.32	0.31	0.35	-46.10	-47.30	-45.10	6.100	6.060
101881	104.5	99.0	110.2	0.34	0.32	0.36	-40.00	-41.00	-39.00	5.980	6.000
112981	43.9	40.3	47.5	0.26	0.23	0.29	-45.50	-49.70	-41.30	5.580	5.620
122781	112.2	108.3	115.9	0.37	0.36	0.38	-39.20	-39.80	-38.60	6.070	6.160
042582	83.8	79.9	87.3	0.31	0.30	0.32	-38.70	-39.60	-37.80	6.070	6.030
070482											6.080
083182	20.0	18.0	26.0	0.16	0.13	0.27	-26.40	-51.10	10.50	0.000	5.200
120582	92.9	89.1	96.9	0.42	0.41	0.43	-44.00	-44.60	-43.10	5.990	6.080
122682	27.2	22.8	32.4	0.81	0.70	0.94	-46.10	-50.20	-42.20	5.660	5.580
061283	131.2	126.6	135.6	0.25	0.24	0.26	-36.00	-37.20	-34.60	6.070	6.020
100683	107.7	103.3	113.5	0.19	0.18	0.22	90.00	-87.30	84.70	5.860	5.950

TABLE 2. (Continued)

Event	Y	Y_{min}	Y_{max}	F	F_{min}	F_{max}	Φ_S	Φ_S^{min}	Φ_S^{max}	$m_{b(Lg)}$	$m_{b(P)}$
102683	137.2	131.2	142.8	0.37	0.36	0.38	-41.60	-42.70	-40.50	6.010	6.040
112083											5.330
021984	65.7	63.0	69.8	0.14	0.12	0.16	-80.80	-112.20	15.40	5.720	5.770
030784	36.8	34.7	38.9	0.44	0.42	0.46	-45.40	-46.50	-41.30	5.680	5.560
032984	74.0	70.3	77.5	0.30	0.28	0.32	-52.10	-54.40	-50.60	5.900	5.860
042584	108.4	102.9	113.5	0.19	0.17	0.21	-2.60	-5.50	0.50	5.860	5.900
052684											6.010
071484	126.2	122.2	129.8	0.29	0.28	0.30	-40.30	-41.00	-39.40	6.050	6.100
091584											5.040
102784	108.4	105.1	111.9	0.36	0.35	0.37	-38.50	-39.20	-37.80	6.090	6.190
120284	63.3	60.0	67.0	0.70	0.68	0.72	-28.80	-29.80	-27.60	5.880	5.770
121684	142.9	138.5	147.1	0.32	0.31	0.33	-39.10	-39.90	-38.30	6.040	6.120
122884	55.5	53.5	57.5	0.14	0.13	0.15	-80.90	-97.10	-61.10	5.980	6.000
021085	107.5	103.3	112.3	0.26	0.25	0.27	-44.20	-45.50	-42.90	5.800	5.830
042585	61.4	58.0	65.0	0.23	0.21	0.25	-39.10	-42.40	-35.60	5.850	5.840
061585	62.4	59.6	65.2	0.34	0.33	0.35	-50.70	-52.00	-49.20	5.980	6.050
063085	87.3	84.2	90.6	0.36	0.35	0.37	-39.00	-39.90	-38.30		5.920
072085	70.8	68.5	73.5	0.38	0.37	0.39	-38.70	-39.50	-37.90	5.860	5.890
031287	33.0	31.0	35.2	0.19	0.17	0.21	-39.70	-41.40	-37.80	5.210	5.310
040387	175.3	169.8	180.6	0.26	0.25	0.27	-41.70	-42.10	-41.10	6.060	6.120
041787	91.4	86.8	95.8	0.45	0.44	0.46	-43.60	-44.20	-43.00	5.910	5.920
062087	55.2	53.4	57.0	0.24	0.23	0.25	-53.50	-55.00	-52.20	5.970	6.030
080287	55.5	52.9	58.5	0.52	0.51	0.53	-49.60	-50.20	-49.00	5.870	5.830
111587	123.8	120.3	127.3	0.17	0.16	0.18	-41.00	-42.80	-39.00	5.970	5.980
121387	118.9	115.8	122.0	0.33	0.32	0.34	-41.50	-41.90	-41.10	6.080	6.060
122787	82.3	79.2	85.4	0.38	0.37	0.39	-43.50	-44.20	-42.80	6.040	6.000
021388	95.6	93.2	97.6	0.24	0.23	0.25	-32.90	-33.80	-32.00	6.040	5.970
040388	113.1	110.0	116.0	0.30	0.29	0.31	-43.60	-44.00	-43.20	6.060	5.990
050488	126.1	116.8	135.8	0.35	0.33	0.37	-40.00	-40.90	-39.10	6.040	6.090
061488	5.4	4.7	6.1	0.31	0.27	0.35	-35.70	-40.40	-30.60		4.800
091488	118.5	115.7	121.5	0.25	0.24	0.26	-38.60	-39.20	-38.00	5.960	6.030
111288	16.4	14.7	18.1	0.55	0.53	0.59	-46.80	-47.20	-46.40		5.200
121788	130.7	126.7	134.9	0.40	0.39	0.41	-40.70	-41.20	-40.20	5.800	5.800
012289	110.8	107.4	114.0	0.25	0.24	0.26	-42.20	-42.60	-41.80		
021289	80.7	75.7	86.3	0.08	0.05	0.11	-43.40	-53.50	-30.70		
070889	42.0	40.7	43.3	0.27	0.26	0.28	-32.10	-33.10	-31.10		
090289	18.2	17.4	19.2	0.32	0.30	0.34	-41.40	-42.40	-40.40		
101989	99.4	96.3	102.7	0.10	0.09	0.11	-24.40	-28.00	-20.20		

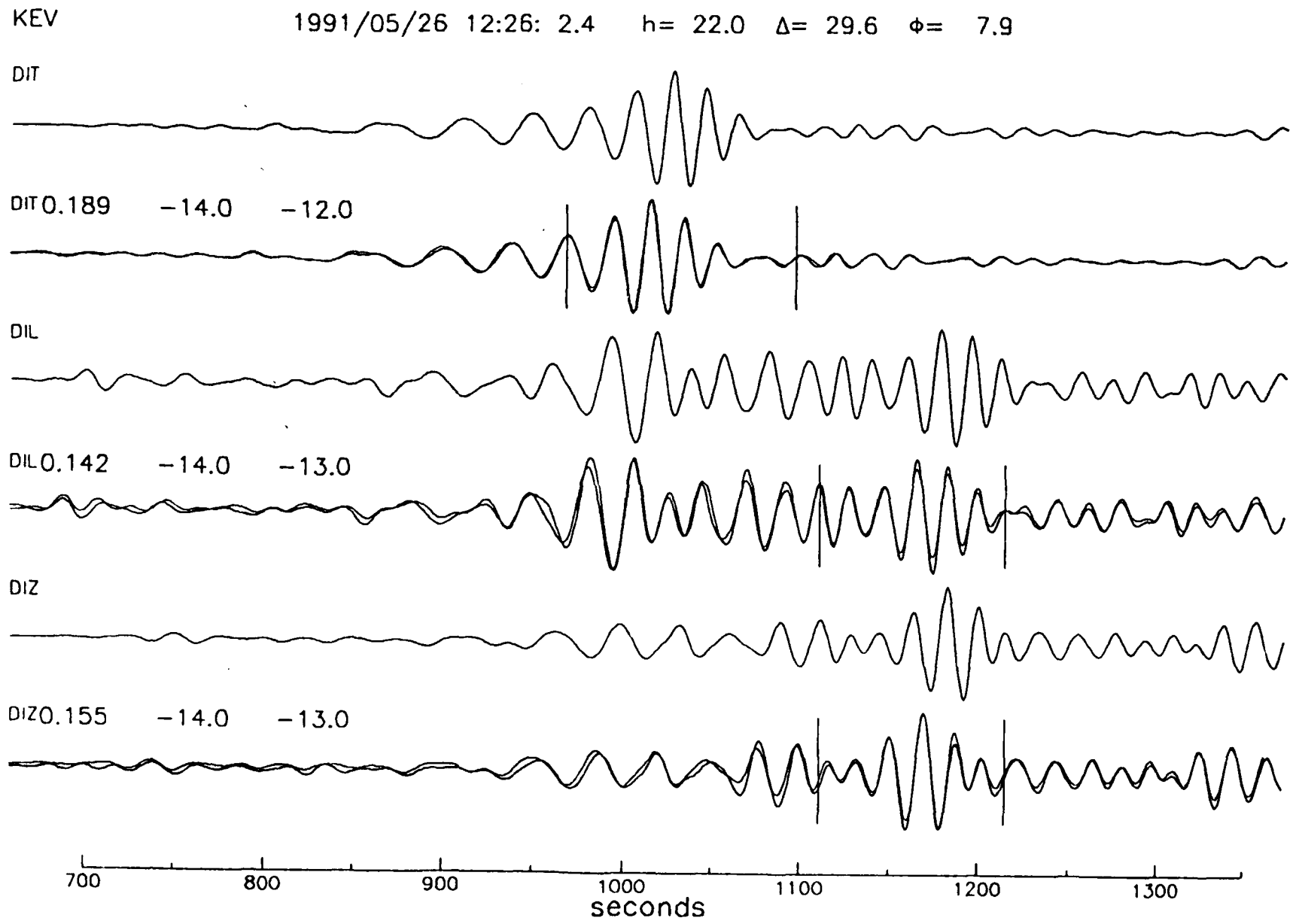
KEV
1991/05/26 12:26: 2.4 h= 22.0 Δ= 29.6 Φ= 7.9
DIT
DIT 0.189 −14.0 −12.0
DIL
DIL 0.142 −14.0 −13.0
DIZ
DIZ 0.155 −14.0 −13.0
700
800
900
1000
1100
1200
1300
seconds

Figure 1

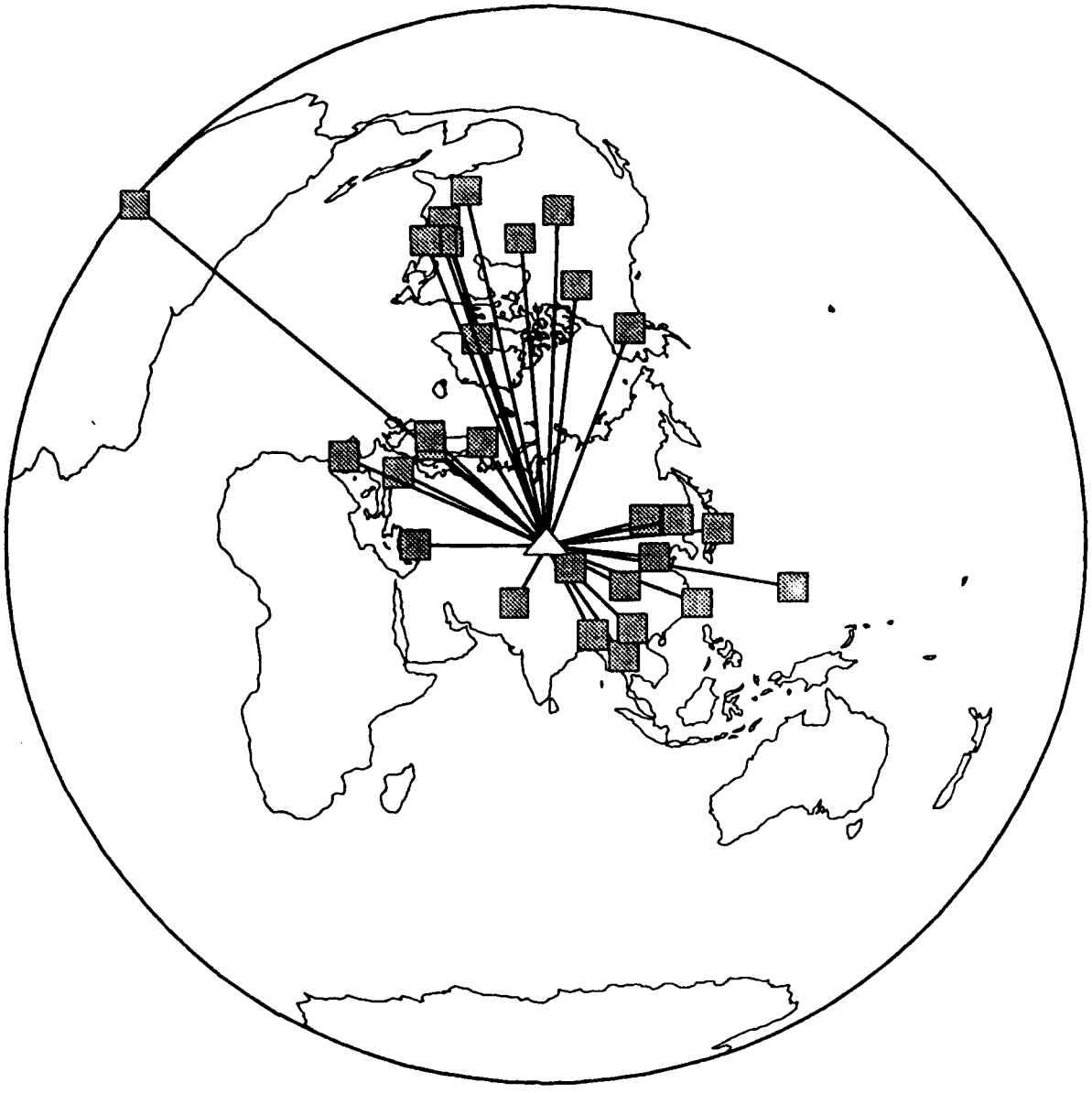

Figure 2

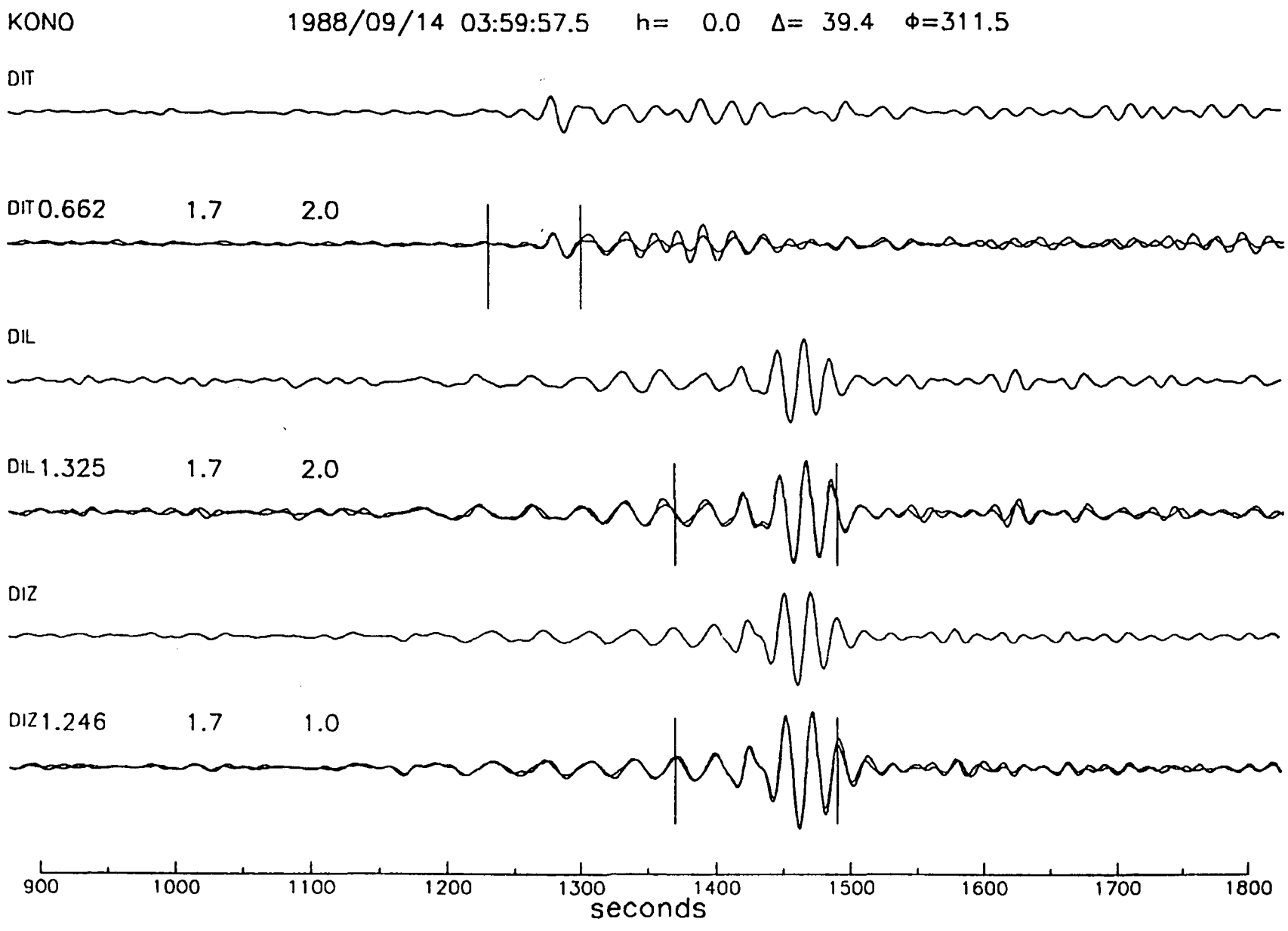
KONO 1988/09/14 03:59:57.5 h= 0.0 Δ= 39.4 Φ=311.5
DIT
DIT 0.662 1.7 2.0
DIL
DIL 1.325 1.7 2.0
DIZ
DIZ 1.246 1.7 1.0
900 1000 1100 1200 1300 1400 1500 1600 1700 1800
seconds

Figure 3

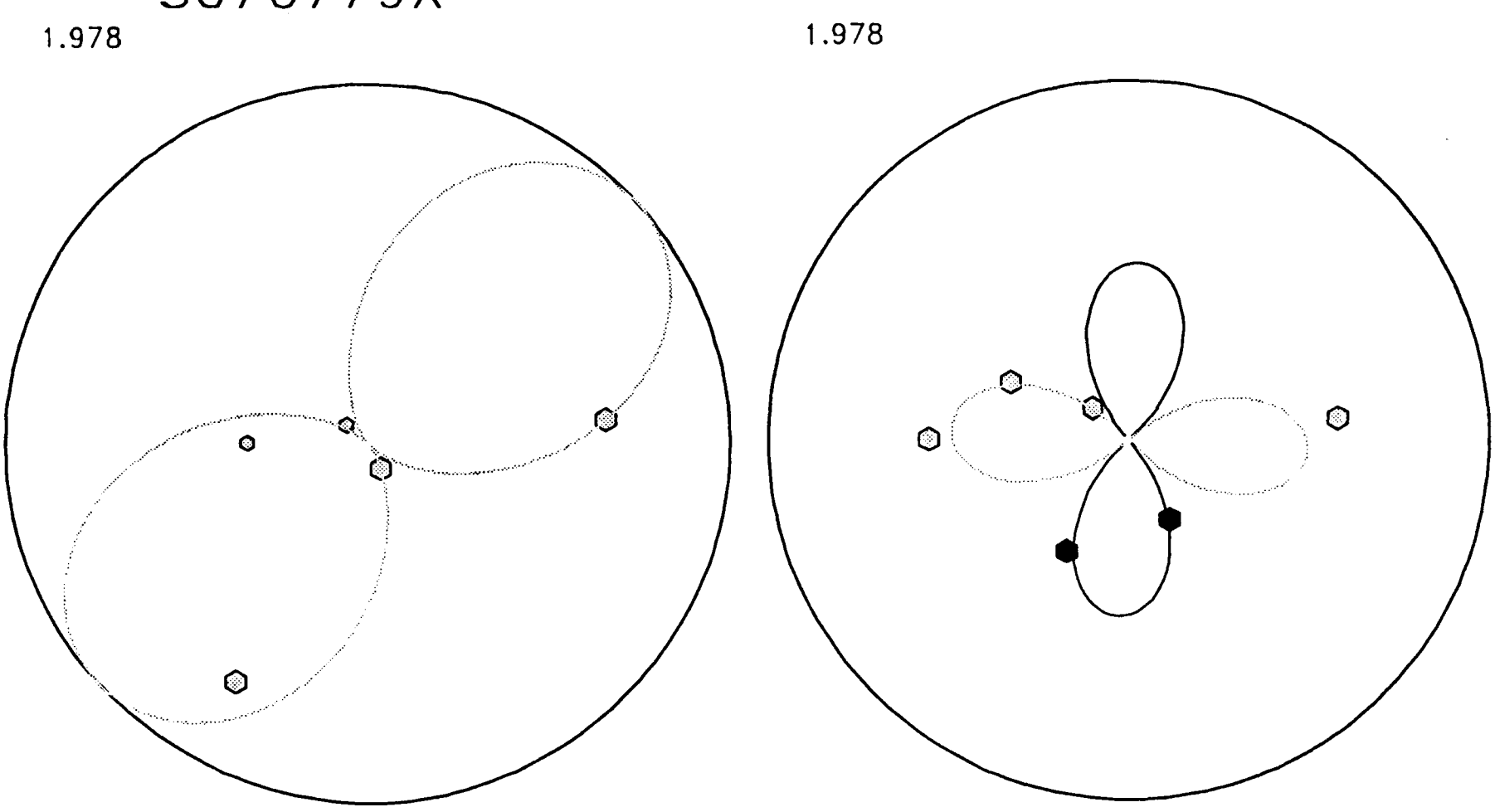

Figure 4*a*

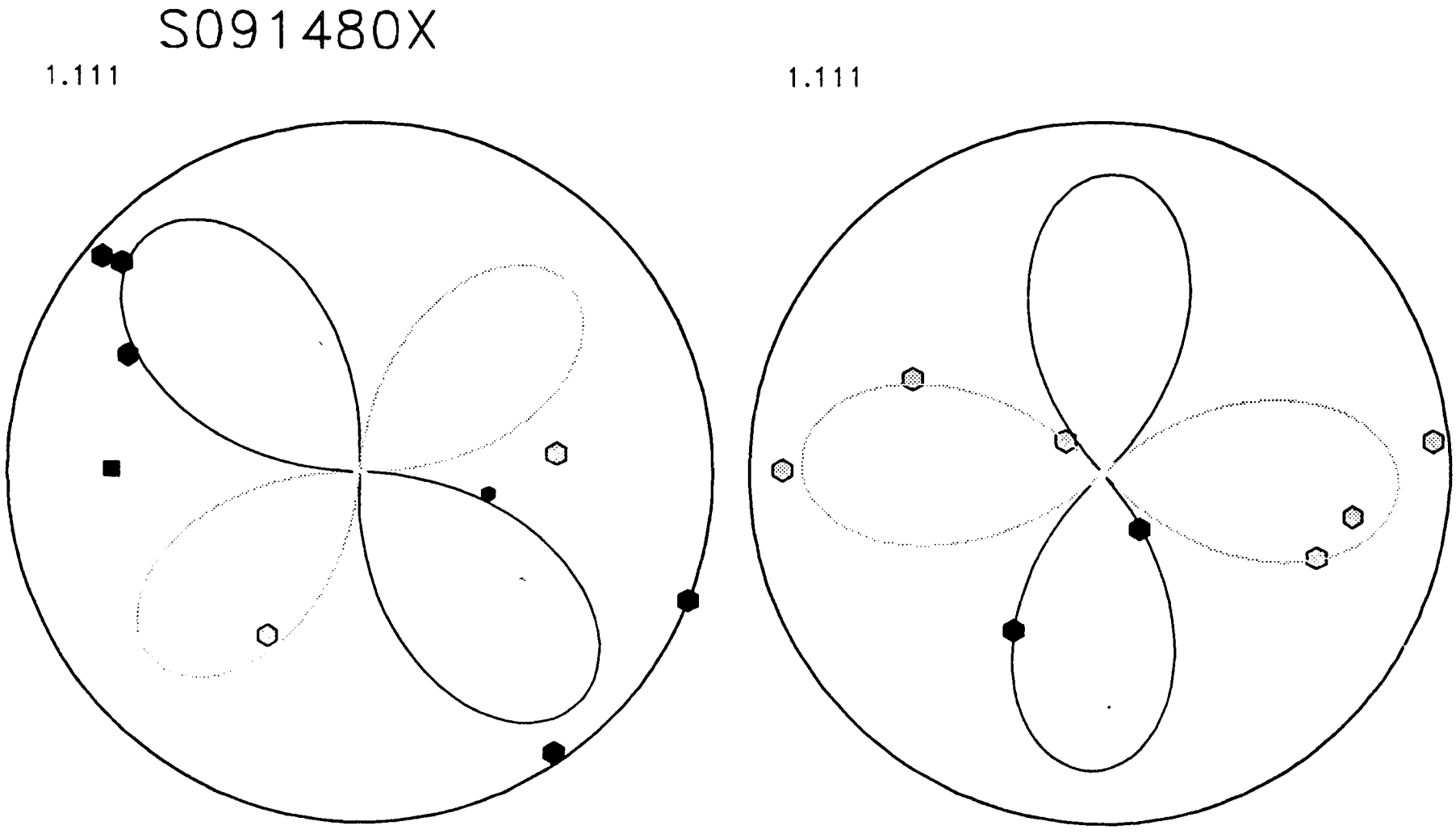

Figure 4*b*

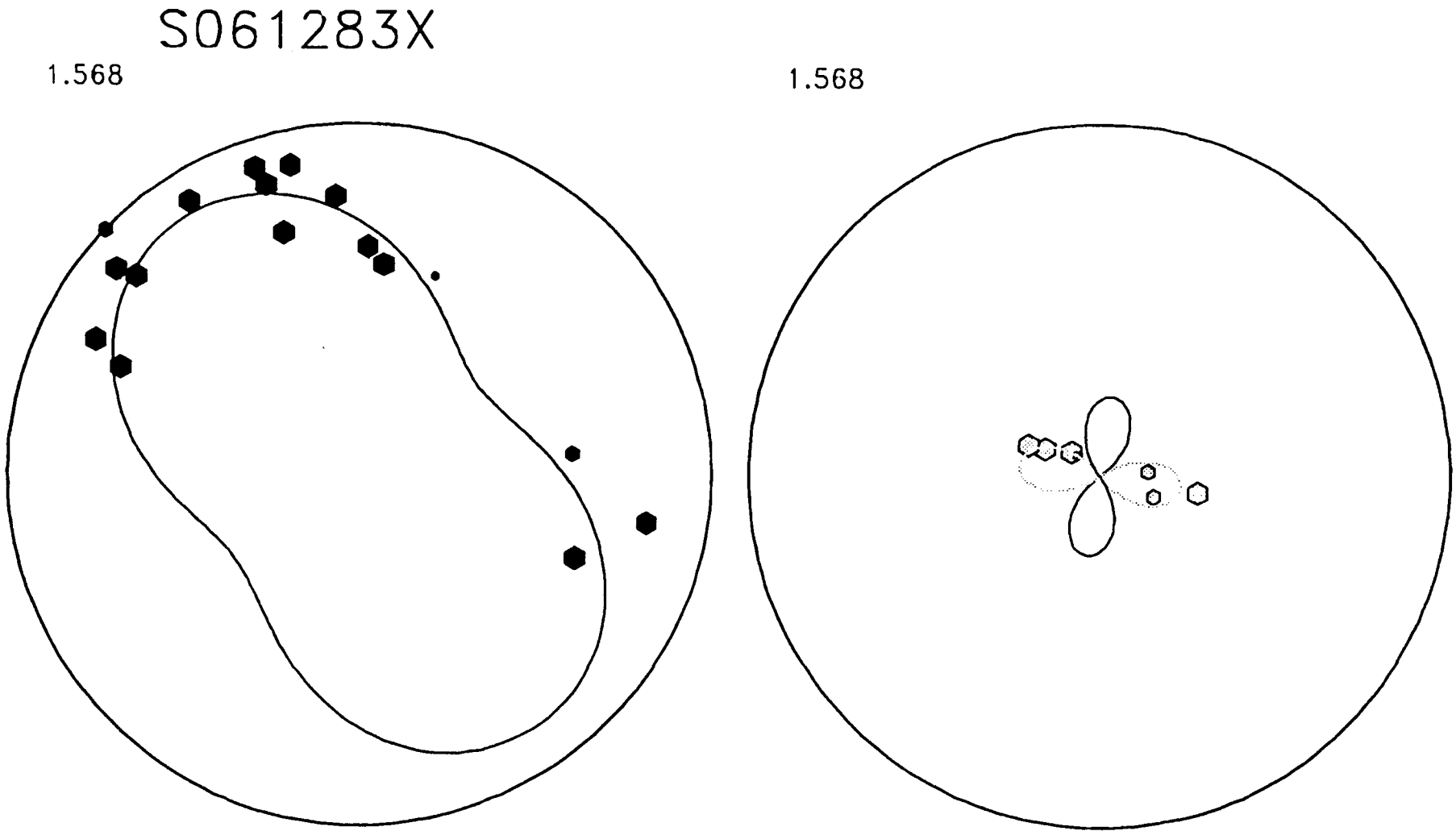

Figure 4c

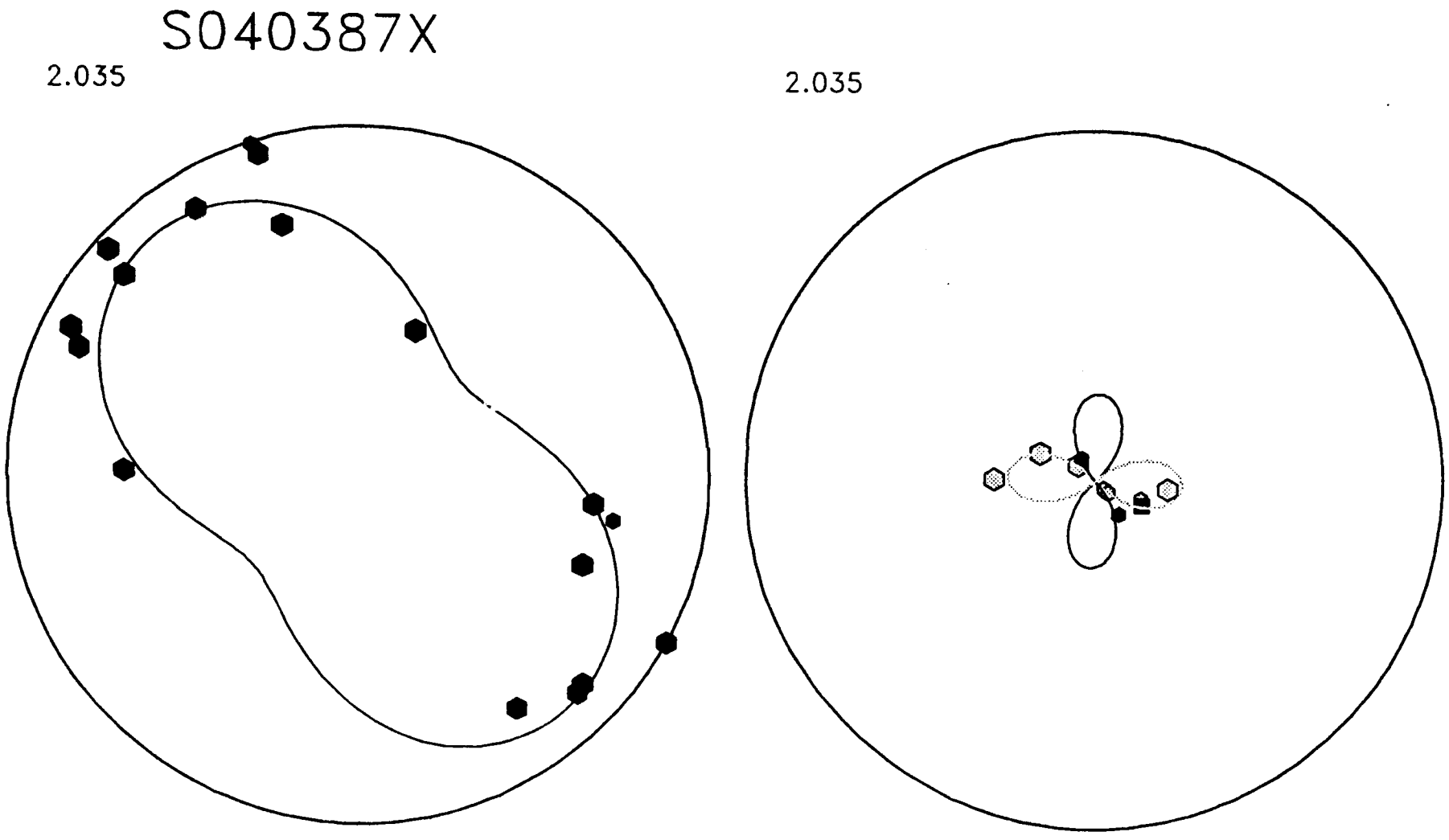

Figure 4*d*

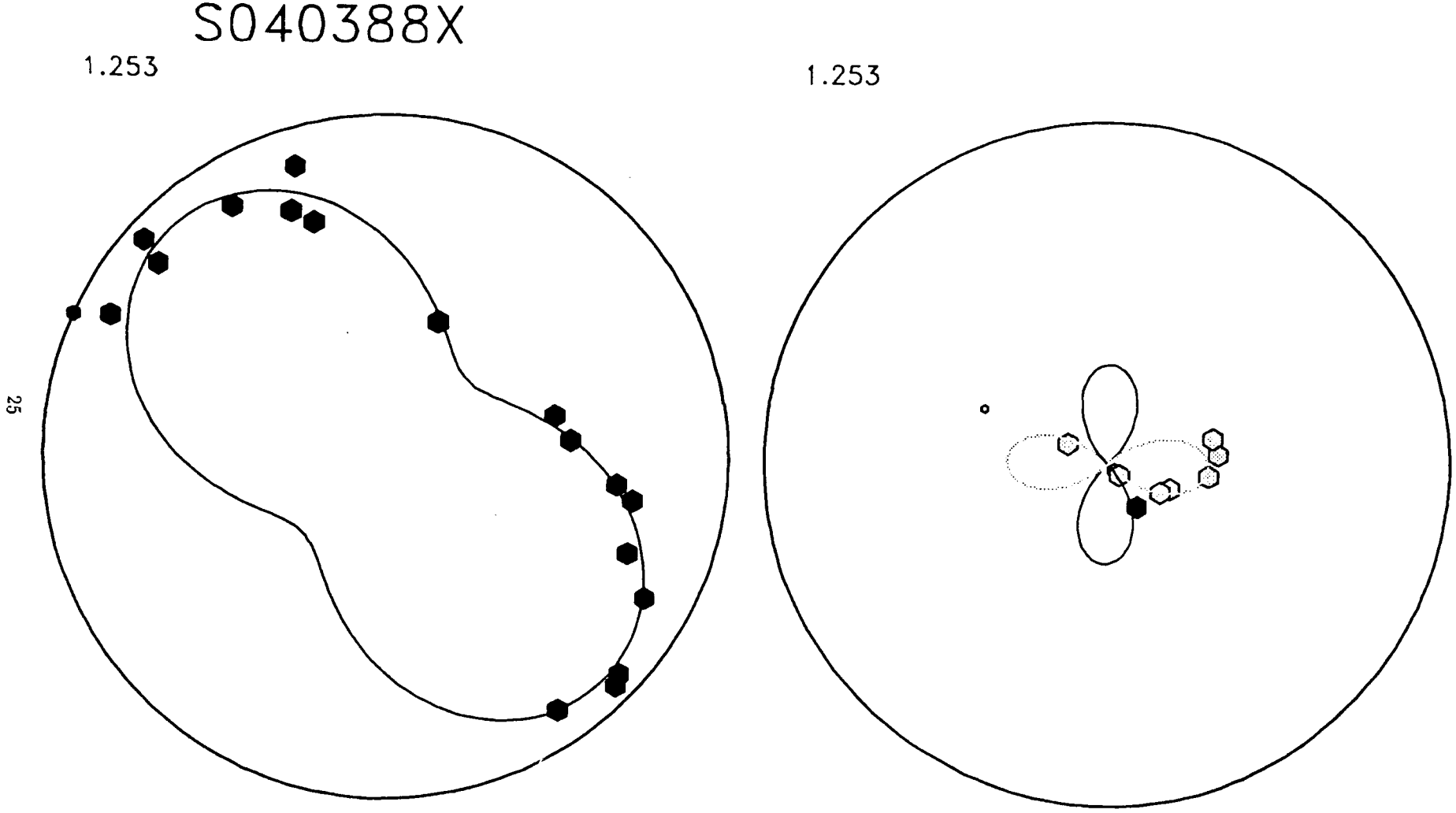

Figure 4e

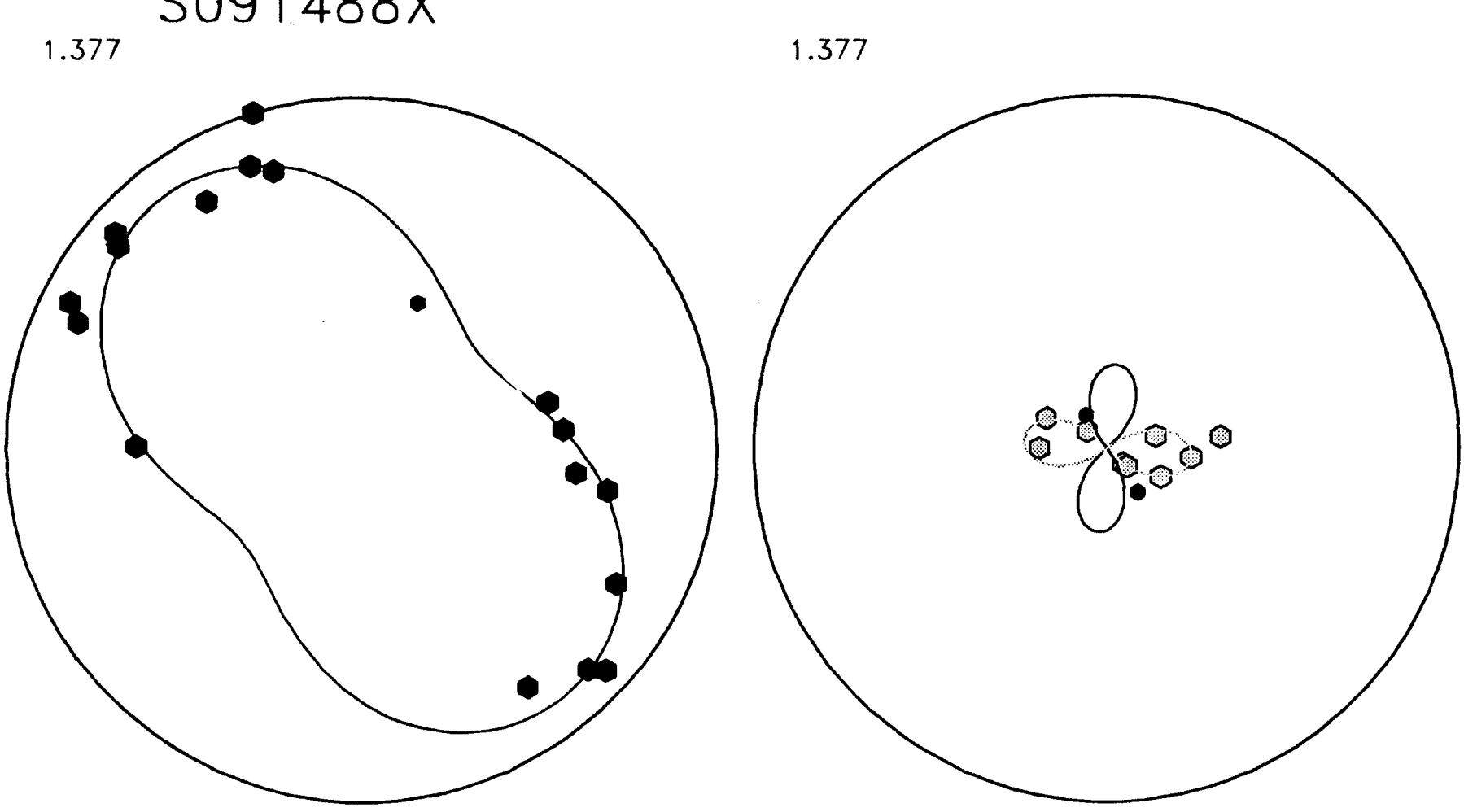

Figure 4*f*

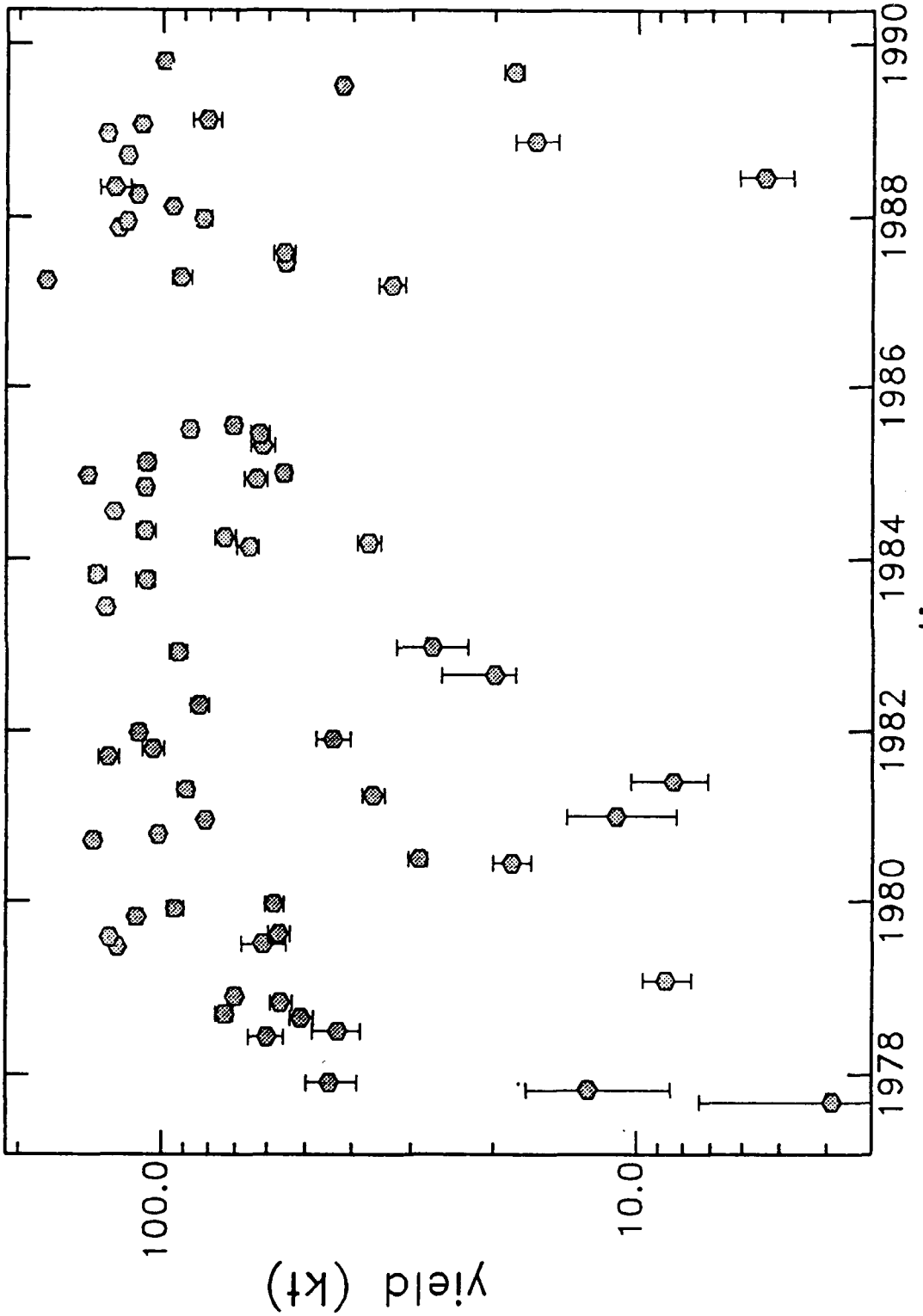

Figure 5

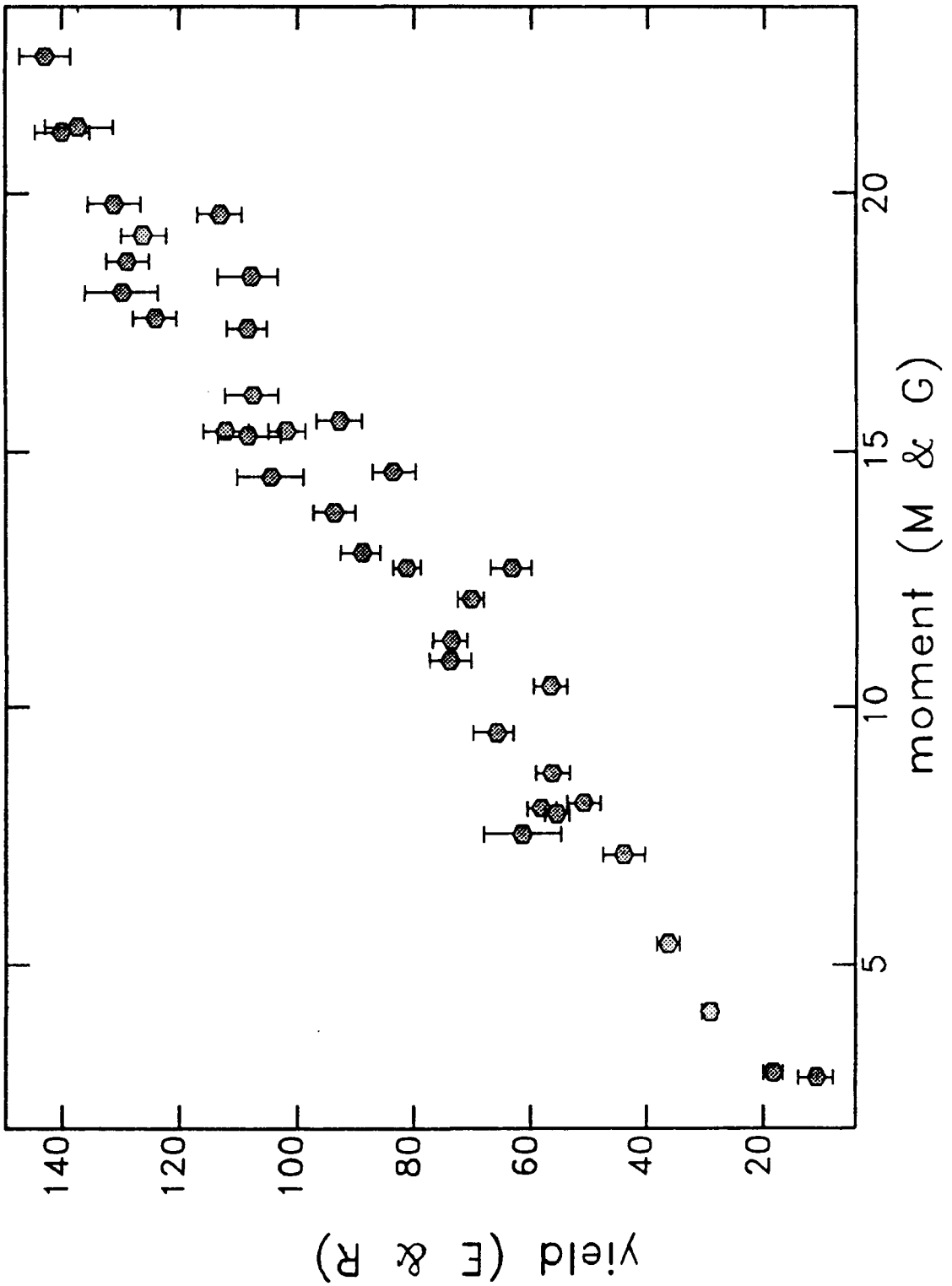

Figure 6

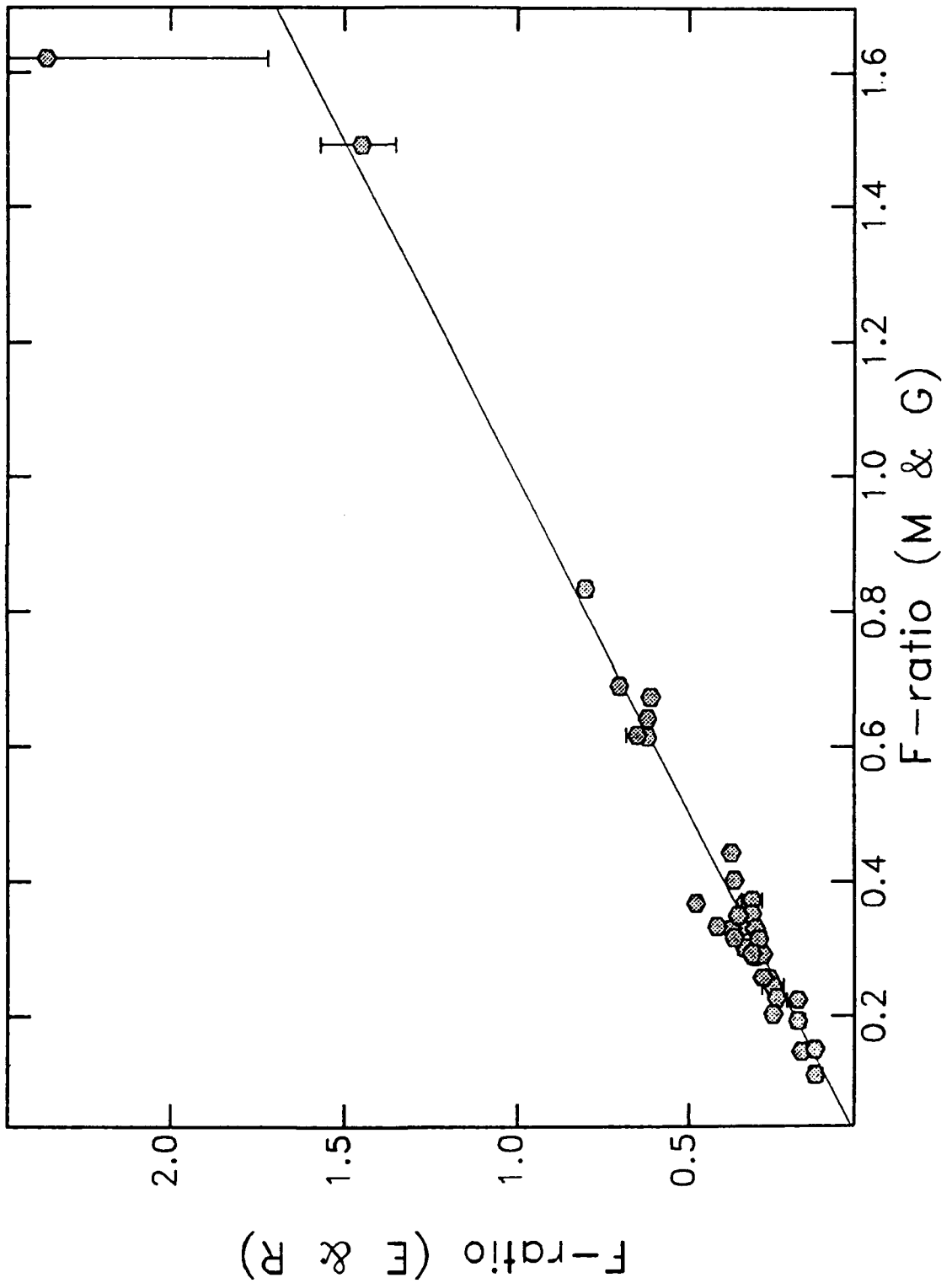

Figure 7

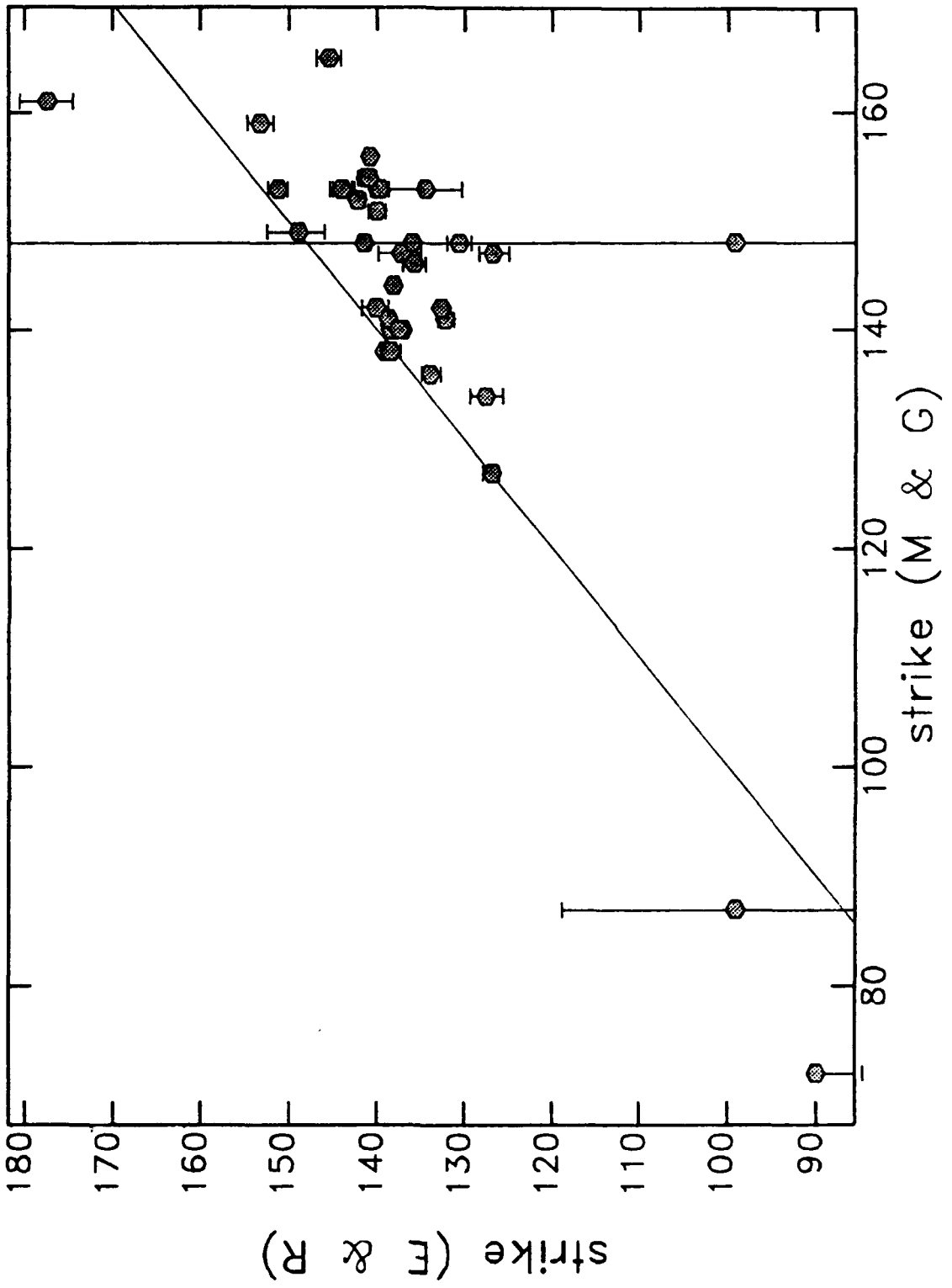
strike (E & R)
180
170
160
150
140
130
120
110
100
90
80
100
120
140
160
strike (M & G)

Figure 8

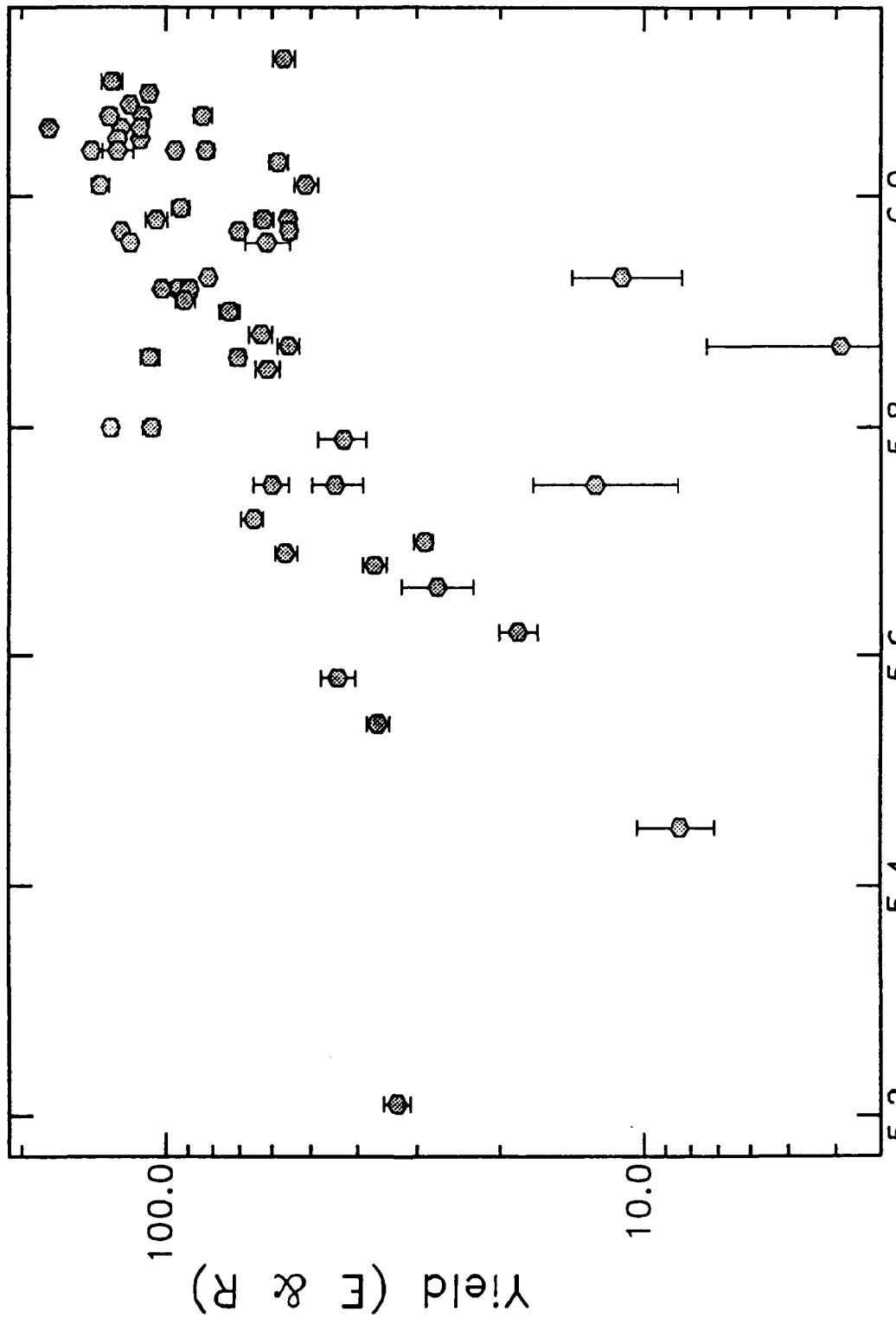

Figure 9

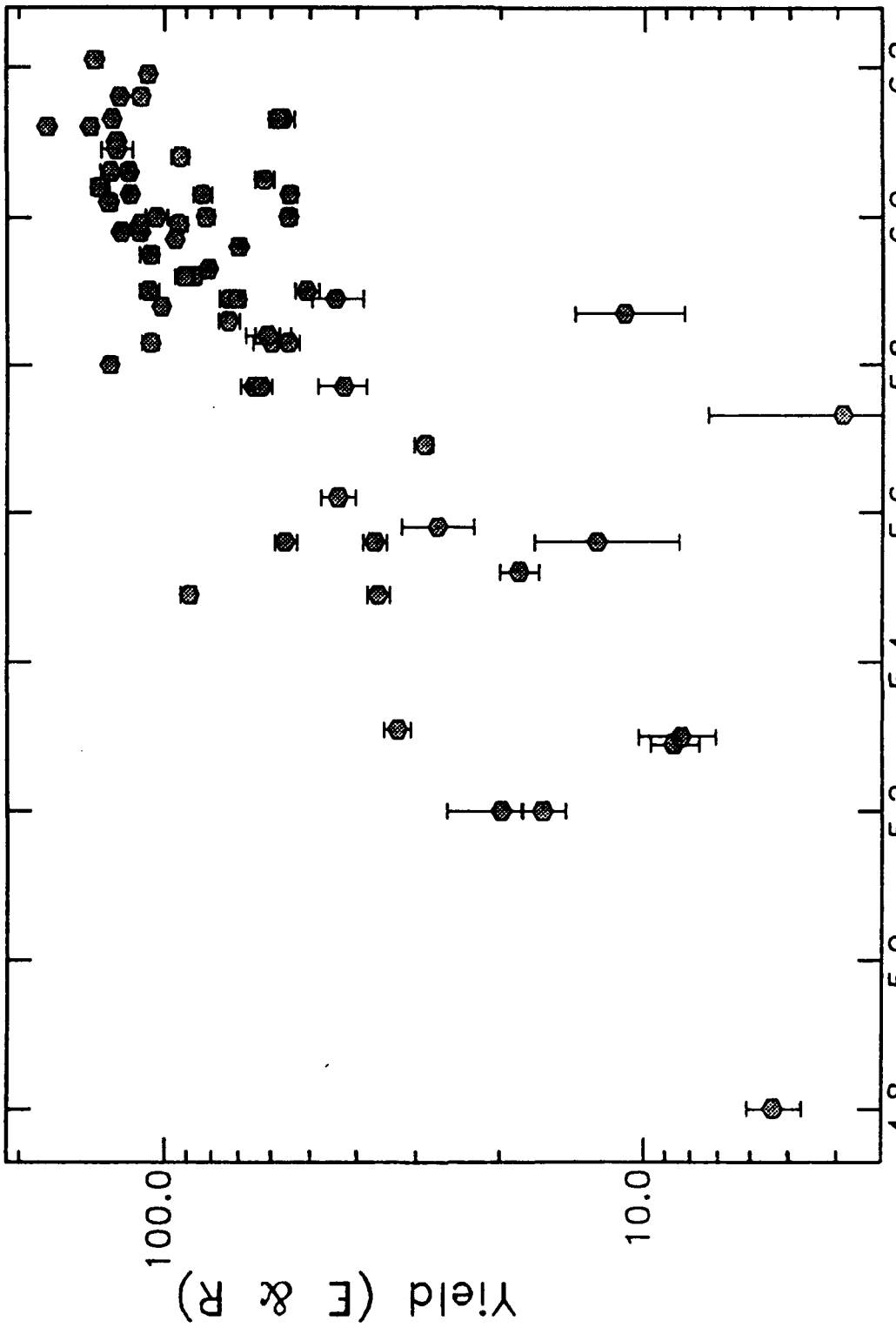

Figure 10

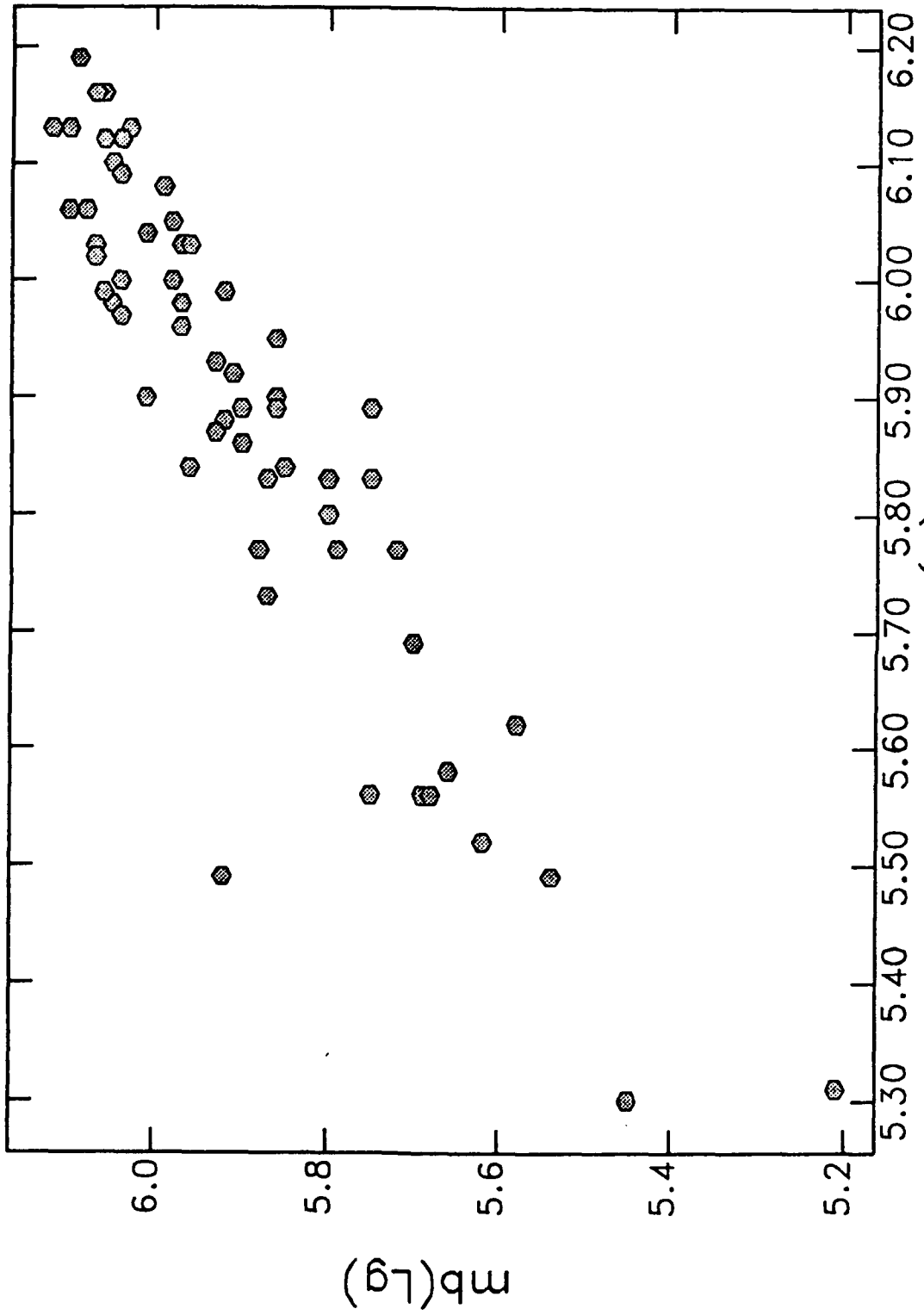

Figure 11

HOW CAN THE OPERATION OF THOUSANDS OF SEISMIC STATIONS (CARRIED OUT BY HUNDREDS OF INSTITUTIONS IN TENS OF COUNTRIES) BEST BE FOCUSSED ON DISCRIMINATION RESEARCH ?

Paul G. Richards
Lamont-Doherty Geological Observatory and
Department of Geological Sciences, Columbia University,
Palisades, New York 10964

ABSTRACT

The most important technical issue in R & D of nuclear explosion monitoring has changed recently, from yield estimation to the more traditional subject of discrimination of small events.

Yield estimation and discrimination present very different challenges in monitoring – differences that have implications for how monitoring can best be organized for different purposes. Yield estimation, whether for large or small explosions, if done well requires well calibrated stations and a coordinated effort that usually will require some type of centralized analysis. Discrimination too may best be done by a tightly directed effort, especially for those who must reach decisions promptly. But seismic stations are being installed at such a rapid rate in so many different parts of the world, and are being operated by so many different organizations, that detection and discrimination capabilities must surely vary quite substantially (and perhaps unpredictably) if *all* pertinent data can be brought to bear on a particular region after a period of a few months.

It is important to think of ways to maximize the amount of pertinent data. This paper reviews briefly the activities of many different organizations that promote deployment of new seismometers, often deployments that are for purposes other than explosion monitoring.

In answer to the title question, a case is made for generating lists of problem events – *seismic sources* whose signals cannot easily be discriminated – as a mechanism for achieving three goals: (1) encouraging seismologists to contribute data that may help to discriminate events on the list; (2) training; and (3) helping to build consensus in the technical community, on what types of problem event are truly intractable with current data.

INTRODUCTION

For the last fifteen years, nuclear explosion seismology in the U. S. has mostly concentrated on yield estimation in the context of monitoring the 150-kiloton threshold, but in the 1990's and beyond the most important issues will be linked to the more traditional questions of detection, location, and identification of small seismic events, especially in the context of non-proliferation.

I think that yield estimation and discrimination present very different challenges in monitoring; and they are different too when it comes to assessing capabilities.

Yield estimation, at least for large explosions, merely requires about 10 to 100 well-calibrated stations, and types of analysis on which there is now broad agreement. Discrimination also can be tackled with about 100 stations, preferably in quiet sites and using telemetry so that those who must make decisions promptly have the data they need. But discrimination capability in practice is likely to be significantly better than will be apparent from any assessment based on about 100 stations or less. Seismic stations are being installed at such a rapid rate in different parts of the world, that discrimination capabilities will often improve substantially and unpredictably in areas of interest, provided **all** pertinent data can be brought to bear on a particular region after a few months.

In the next section of this paper I briefly describe some of the new initiatives in seismic networks in different parts of the world. Then I argue that the way we make progress, in using these initiatives to improve monitoring capability, is to identify problem events and see if there is more data out there to solve the problem.

NEW INITIATIVES IN INSTRUMENT DEPLOYMENT AND DATA ANALYSIS

The most important new deployment of instruments for the Air Force and DARPA research program is of course the network of broadband seismometers installed in the USSR by IRIS and the USGS, beginning in 1988. Seven stations are now operational, and approval has been received for another seven sites. However, it should also be noted that GEOSCOPE has independent plans for stations in the Soviet Union, and that there are good stations operated by the USSR.

Plans are underway for modernization of the Canadian National Seismograph Network (CNSN). The goal is to achieve complete monitoring of all seismic events down to magnitude 3.

The new U.S. National Seismograph Network (USNSN) of the US Geological Survey has formally begun operations. The USNSN has as a design goal a capability for generating a bulletin that will be complete down to m_b 2.5.

In the Mediterranean-Alpine region, there is a new network known as MEDNET. Again, it is a deployment of broadband digital instruments that will consist of on the order of ten stations.

In the southern hemisphere plans are well advanced for the Global Telemetered Seismograph Network (GTSN). The US Geological Survey is to operate this network, under a plan based on cooperative agreements with agencies in Argentina, Bolivia, Botswana, Brazil, the Central African Republic, the Ivory Coast, Paraguay, and the Republic of South Africa. Considerable care has gone into choosing quiet sites, and the data from this network will be of great interest to research geophysicists as well as to those concerned with explosion monitoring.

For monitoring seismicity in the oceans, there are several initiatives. An old trans-Pacific cable, known as TPC-1, has been retired from service and is now to be managed in a partnership between IRIS and the Earthquake Research Institute of Tokyo. The plan is to use the cable for power and data transmission for seismic and other geophysical sensors on the ocean floor. Japan also has in its POSEIDON program a plan for new seismometers in Korea, Antarctica, the Philippines, Sakhalin, and Indonesia.

Of course, people can be worried that with the growth in digital seismology, the skills and even the art of seismometer reading will be lost. But a program known as the International Seismological Observing Period (ISOP) addresses this issue head on. It stems from an excellent idea of Tom Jordan's a few years ago. The purpose of this program is to provide new data for mapping the three-dimensional structure of the earth's mantle and core, using the *existing* global stations. The duration will likely be about three years, preceded by a period for organization of the program. ISOP is sponsored by several international organizations, including IASPEI, and UNESCO. It includes training courses and workshops, which are intended especially for scientists in third-world countries.

Coming closer to home there are plans being developed for a consortium of US Regional Networks (CUSRN). There are about 50 such networks now in the US, operating 1,200 seismometers in the west and 1,500 stations total. About 50,000 local earthquakes are detected each year, and about 7,000 teleseisms. Funding is at around $10 million a year from federal agencies, and about $2 million from state agencies. Much of this data (but not all) is digital, and analysis is often carried out in a sophisticated work station environment.

The U.S. Geological Survey has recently developed a list of about 7,000 seismological station locations. Table 1 is a list of perhaps bewildering names, places, programs, and acronyms, all having to do with new deployments of seismometers, or of seismic data archiving, data exchange, and analysis. I have so far mentioned only a few of the items in the Table, and to make one of the main points of this paper (that there is much more data in circulation than is generally appreciated), I have purposely emphasized programs that are not principally driven by consideration of explosion monitoring.

CDSN	POSEIDON
SAMSON	GERESS
Poland	Mongolia?
GTSN	Canada (CNSN)
MEDNET	IRIS/PASSCAL
IRIS/USGS GSN & JSP	ISOP
FDSN	N. California
TERRASCOPE	GBRN
CUSRN	ORFEUS
USNSN	SGBSN
BRV archive	USGS/NEIC/PDE/QED
GEOSCOPE	MIDAS

Table 1. A list of places and projects associated with new seismological hardware, seismic data acquisition, and data analysis.

An important point about the items in Table 1, is that no single individual knows about all of these projects in any detail. Also no single government agency is knowledgeable across the board in modern seismology. Although there may be debate on the significance of these different projects, there is one point on which I'm sure we can all agree. Quoting from the Old Testament Book of Daniel (Chapter 12, v.4, Revised Standard Version)

"Many shall run to and fro, and knowledge shall increase."

The quotation begs the question:

What shall we do with this new knowledge?

USES OF NEW DEPLOYMENTS/DATA SETS - LESSONS FROM THE PAST

For purposes of discrimination, one way to proceed is to assemble sets of seismological data without much pre-analysis, without using much seismological knowledge, and then try to locate the underlying seismic events.

As an example of this approach, it is of interest to look at the Final Event Bulletin of the second GSE Technical Test conducted earlier this year (1991) in a project known as GSETT2.

Figure 1 was tabled by the United Kingdom in Geneva this summer. It shows the locations obtained from analyzing the data contributed by 56 stations, as reported in the Final Event Bulletin, and there are a number of surprises. The known seismic regions of the world are shaded in the figure, and in the six-week period of the the technical test it appears that a large number of events were located in aseismic areas. Figure 2, also tabled by the UK in Geneva, shows for the same period the locations obtained by the USGS's Branch of Global Seismology and Geomagnetism, in what is known as the Preliminary Determination of Epicenters (PDE). The USGS does not include the large number of very small magnitude events included in GSETT2. Figure 2 demonstrates that the USGS locations (based on far more stations than those used by GSETT2 for Figure 1), give only a few events in aseismic regions. Other problems with Figure 1 include an event more than 600 km deep in Germany that has a surface wave magnitude of 6.7. A Rayleigh wave reported in Scotland is associated with a magnitude 3.7 event in the Kermadec Islands. There is a large event in Ireland, unrecognized by seismologists in Scotland. And

earthquakes, known to Australian seismologists as being in the Banda Sea, have in the Final Event Bulletin been put back on the Australian continent.

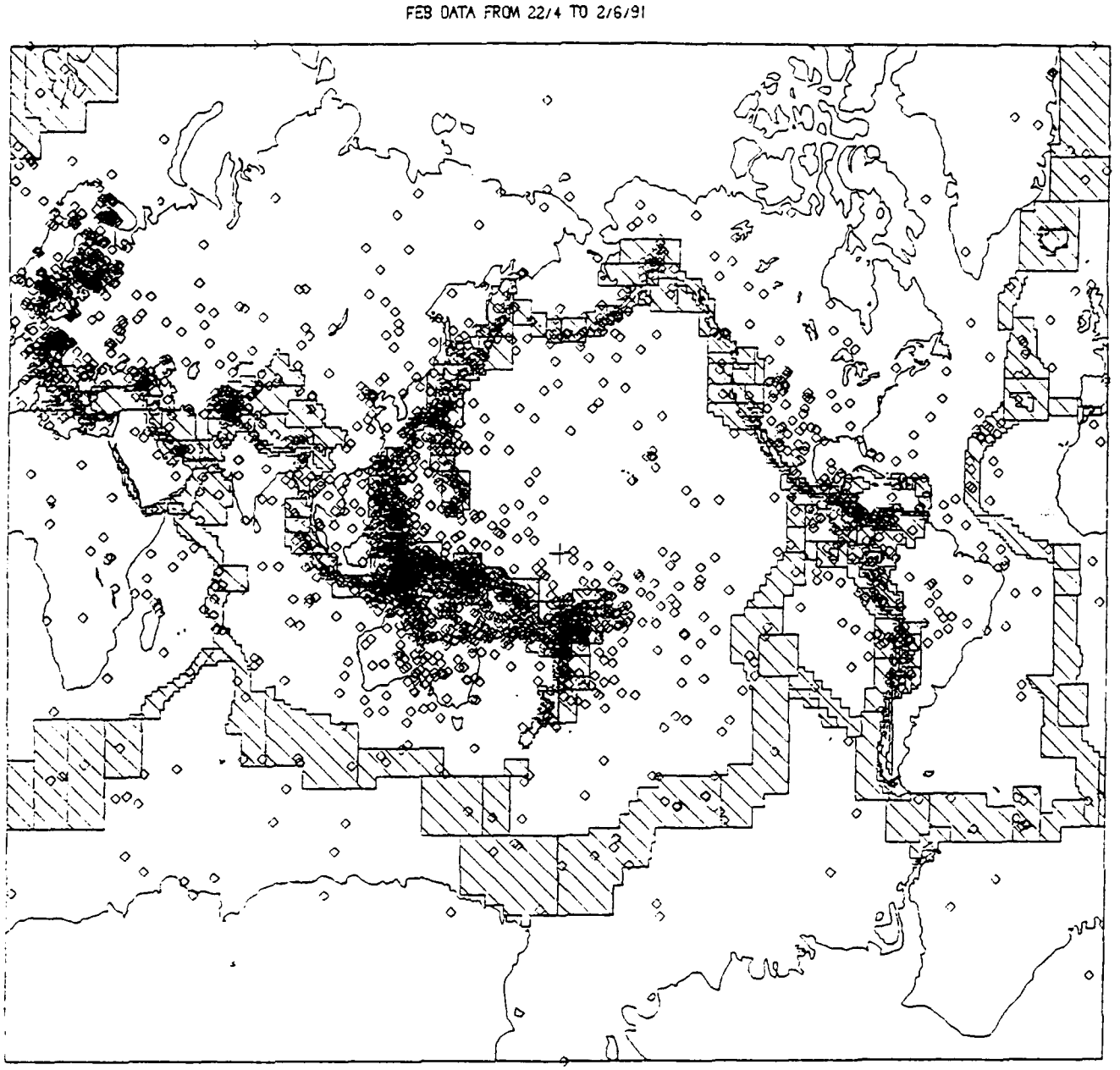

Figure 1. GSETT2 events compared with seismic regions: epicenters from Final Event Bulletin (figure from paper GSE/UK/53 tabled in Geneva, summer 1991).

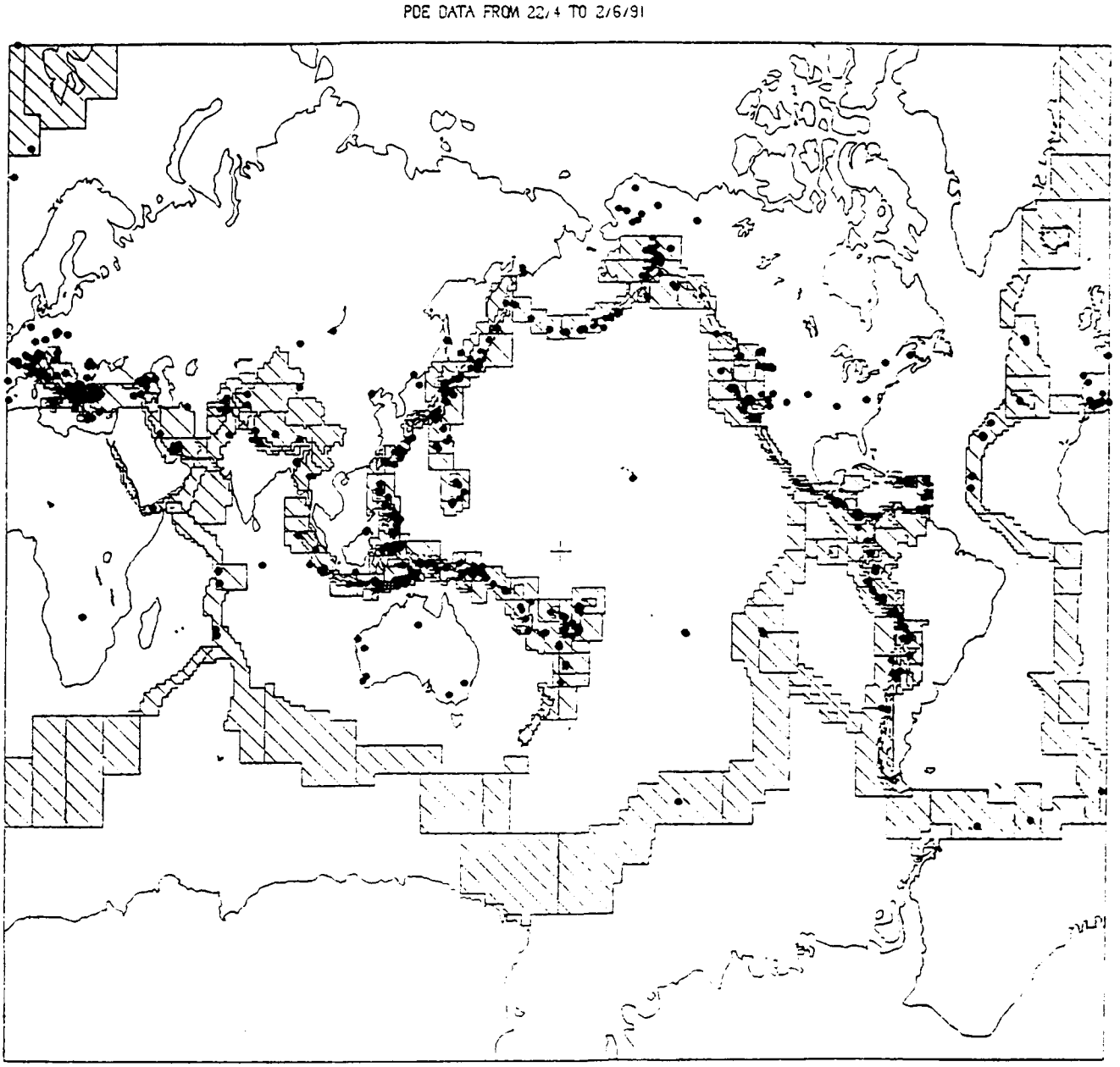

Figure 2. GSETT2 events compared with seismic regions: epicenters from PDE (USGS/NEIC) (figure from paper GSE/UK/53 tabled in Geneva, summer 1991).

I am sure that GSETT2 has taught the community some very useful lessons in data exchange, and the Final Event Bulletin has been useful as illustrative of what happens when large amounts of data have to be processed in a short time. But let all of us refrain from allowing Figure 1 of GSETT2 to be used as an example of the best that can be achieved in detection and location.

Nearly twenty years ago, in an exercise known as the International Seismic Month (ISM), coordinated by Lincoln Lab, seismic arrival time data for 150 stations around the world were analyzed to produce as good a catalog of seismicity as then possible, for the period February 20 – March 19, 1972. The stations included two arrays, LASA and NORSAR. Detections and locations were subsequently compared with those derived from a subset of 32 stations selected to provide good geographical distribution and high detection efficiency. The conclusion of this experiment was that "carefully analyzed data from a few but well-selected stations are considerably more effective in a seismic identification context than those reported less meticulously from a much larger network". It therefore appears that a possible framework for future study is use of a good global network, reporting teleseismic data, as a first cut at generating the global catalog, followed by additional studies using regional data (perhaps from additional stations) in regions of particular interest.

This framework introduces the subject of problem events. In 1972, the United States tabled a CCD paper in Geneva with statistics on some earthquakes in Tibet that were claimed to be anomalous on an M_S:m_b diagram, because they looked like explosions. As an exercise in challenging the community to do better, these Tibetan earthquakes were very useful. A group at Lamont looked at a hundred earthquakes in the area, including the problem events, and showed how to do a better job of measuring M_S, and also of m_b. In part, they did their work by getting more data and they showed all the events were in the expected position of earthquakes on an M_S:m_b diagram.

The 1972 CCD paper, concerning anomalous events, also noted that "such events have been noted on some occasions to occur in some other regions as well." The reference included a 1969 event in Kazakhstan, for which a 1972 publication out of MIT's Lincoln Lab gave the M_S:m_b diagram shown in Figure 3. The most obviously problematic event is KA. At the time, the depth was estimated as about 50 km, and this problem event stimulated Alan Douglas, Robert Pearce and colleagues to several special studies using teleseismic data. One problem with the 1969 event is that it occurred at a time similar to an earthquake in Tonga that put larger surface waves at Asian stations such as Kabul, so that the surface wave magnitude for the smaller Kazakhstan event was hard to estimate.

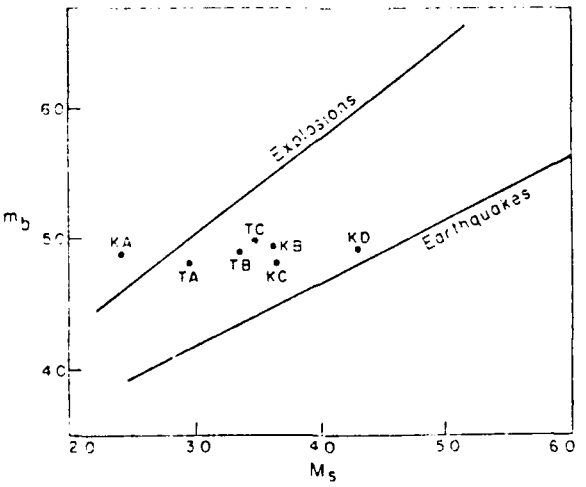

Figure 3. An early example of an M_S:m_b diagram, for anomalous seismic events in Central Asia (taken from Landers, Geophysical Journal, v 31, page 334, 1972).

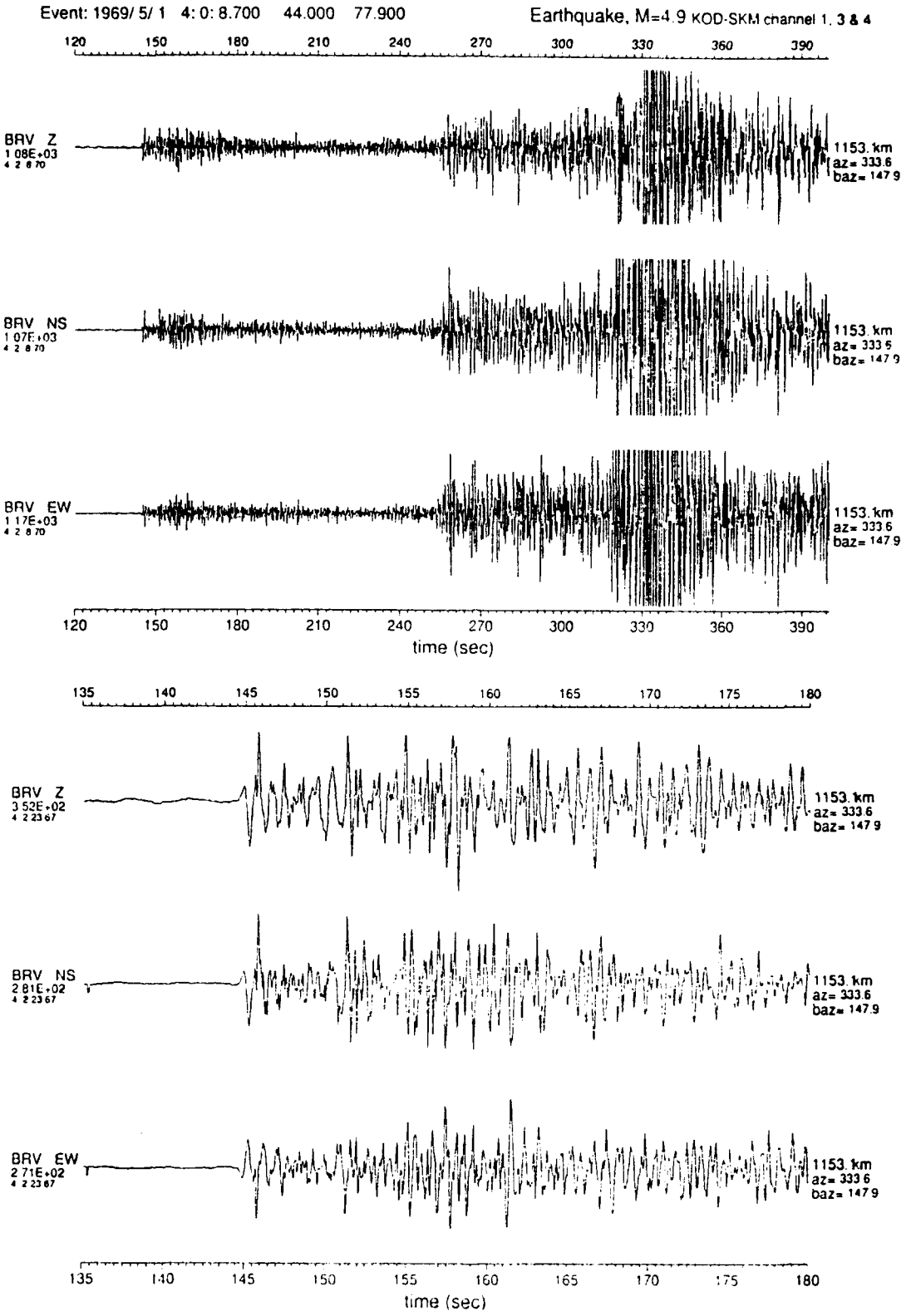

Figure 4. Three-component digital seismograms at stations Borovoye (53° 3' 29"N, 70° 16' 58"E) for a 1969 earthquake in East Kazakhstan (event KA of Figure 3) at a distance of about 1,100 km. Upper and lower displays have different time scales.

I thought of this 1969 event last year, when I was told by Soviet seismologists of their best observatory, which is in Borovoye, North Kazakhstan. We had not heard of this observatory before but I was told that it had a digital archive going back to 1966, and I should be able to get the data. Borovoye is about 700 km northwest of Shagan River and 1,100 km from the problem event of 1969. I made a data request and received a tape in March, 1991 that has digital data for the 1969 event (see Figure 4), and for 42 other interesting seismic events in the region (including data for many large nuclear explosions at the Semipalatinsk test sites). For the 1969 event we can see the regional waves *Pn*, *Sn*, and *Lg*. Won-Young Kim and I, at Lamont, are currently working with regional synthetics to get a depth estimate.

Another interesting Kazakhstan event occurred on March 20, 1976, that puzzled many seismologists for a while because it appears to be an earthquake close to the Semipalatinsk test sites, yet in some respects it looked like an explosion. For example, the teleseismic first motions are all compressional, presumably because the focal mechanism is a thrust. It is reassuring that the data at Borovoye, at a regional distance, show a dilatation, as noted in Figure 5.

I am in danger of digressing on the wonders of the Borovoye data, but that story should be told in a different paper. I introduced it here, as a special example of the idea that new data can come along later, and help solve old problems. (In these cases, the earthquakes occurred years ago. There were few digital stations in operation, and the "new data" came along much later.)

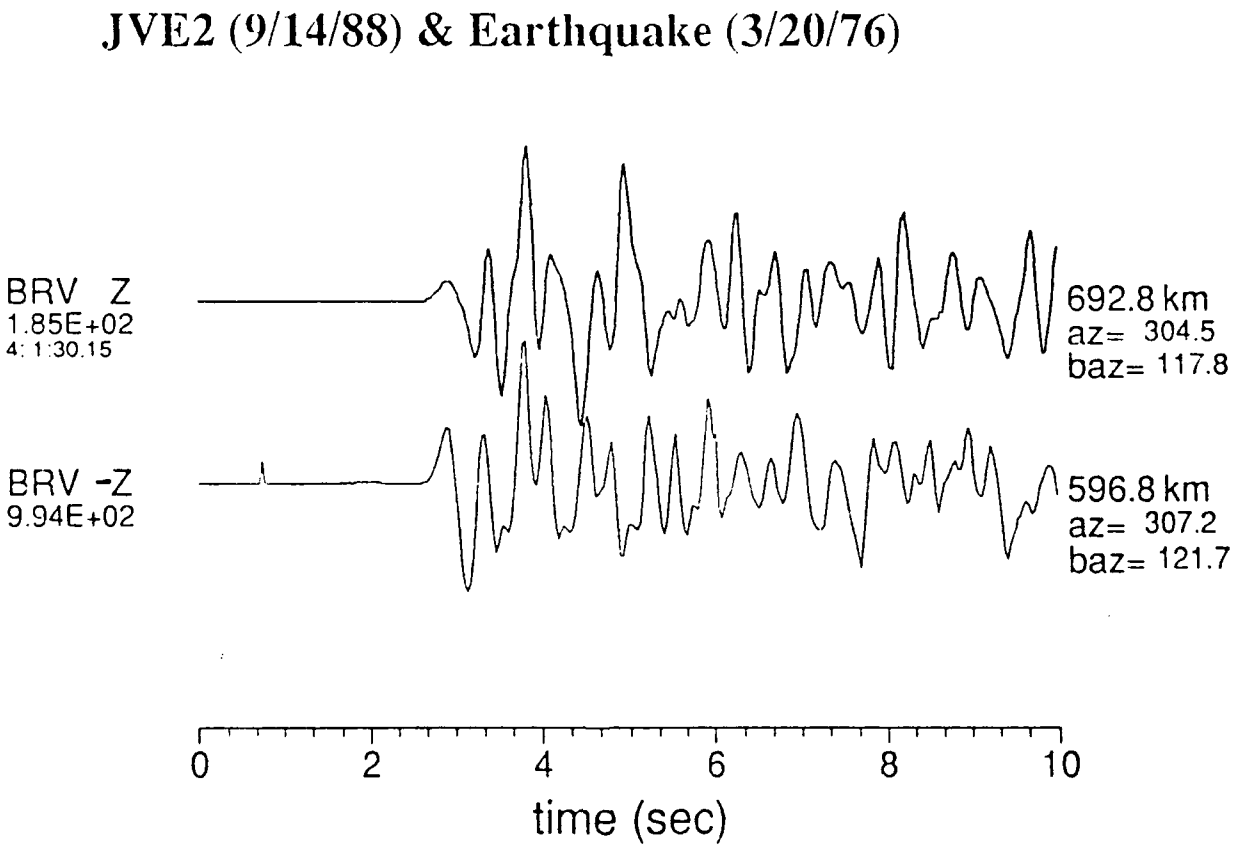

Figure 5. A comparison of the vertical first motions recorded at Borovoye, Northern Kazakhstan, for two seismic events in Eastern Kazakhstan. The upper trace shows the JVE2 nuclear explosion of 14 September 1988; the lower trace (which has reversed polarity) shows the earthquake of 20 March 1976, with a dilatational arrival.

DISCUSSION AND CONCLUSIONS

There are three good reasons for publicizing and studying Problem Events:

(1) to encourage seismologists to contribute relevant data;

(2) training (in techniques of detection and discrimination); and

(3) helping to build consensus, on what types of event are truly intractable with current data.

The third reason is less obvious than the first two, but in my opinion the third reason is the most important. We are a long way from consensus on what constitutes problem events. Part of the difficulty is that seismologists often publish the outcome of special studies in which a particular detection or discrimination algorithm is applied to a particular dataset – and the conclusions of such special studies are often summarized, quite appropriately, in terms of a type of failure. For example, one preliminary conclusion of a study of the GSETT2 data was that for events in the South Pacific, if one wants to achieve locations better than to 20 km, the events have to be bigger than magnitude 6. However, *the danger is that such failures can be taken as representative of monitoring capability as a whole*, when they are merely a comment on the particular experiment in which the failure emerged. If one wants to do a better job of locating some problem events in the South Pacific, an obvious step would be to request data from the regional networks operated by New Zealand.

A useful way to treat the Final Event Bulletin of GSETT2, may be to regard it as a large number of problem events. If additional data is sought, and combined with better interpretation of regional data already available, then perhaps the GSE can publish a set of locations that improves considerably on that shown in Figure 1.

The community engaged in seismic monitoring R & D would be well served, if mechanisms were developed to bring out problem events for general discussion, and thus to focus efforts on trying to define the bottom line: what is our capability to monitor small nuclear explosions?

Unfortunately, there is a danger that discussion of problem events can easily become a somewhat hostile procedure. We need to develop mechanisms in the research community, for bringing problem events into the open in a constructive way.

ACKNOWLEDGEMENTS

I thank Bob Crosson for supplying details on CUSRN; Bob Engdahl for ISOP plans; and several participants in the GSE for information on GSETT2.

High-Frequency Spectra of Regional Phases from Earthquakes and Chemical Explosions

W. Y. Kim, D. W. Simpson and P. G. Richards[1]

Lamont-Doherty Geological Observatory
Palisades, N.Y., 10964
[1]also Department of Geological Sciences
Columbia University

ABSTRACT

The spectral - temporal characteristics of regional seismograms can be used to discriminate between different types of seismic sources. We analyze the high-frequency (1 - 40 hz) spectra of chemical explosions and earthquakes at local and regional distances to understand the seismic signal characteristics of different types of sources and to find stable discriminators. We evaluate the application of the spectrogram technique to regional seismograms in different geologic settings using data from single explosions, multiple-hole instantaneous explosions, ripple-fired quarry blasts and earthquakes. The effects on high-frequency spectra of local source and recorder site conditions and source to receiver path are also analyzed.

Spectrograms of regional seismograms provide discrimination of most ripple-fired quarry blasts from other types of seismic sources. An advantage of the spectrogram method over other discriminators is its use of the complete seismogram rather than isolated phases, such as Pn, Pg and Lg. High-frequency spectra from ripple-fired quarry blasts show clear time-independent frequency bands due to the repetitive nature of the source and are distinctively different from the spectra of single blasts or earthquakes. However, like other discriminators based on spectral estimates, the spectrogram method requires data with high signal-to-noise ratio at high frequencies for unambiguous discrimination. The method is limited in cases where there is low signal-to-noise ratio and for irregular delay shooting pattern or near instantaneous shooting.

While the banding observed in the high frequency spectra from ripple fired blasts distinguishes them from earthquakes and single explosive shots, it is harder to discriminate single explosions from earthquakes on the basis of their frequency content alone. The P to S spectral amplitude ratio at high frequencies (above 10 hz) provides a complementary tool in discriminating between single explosions, multiple-hole instantaneous shots and earthquakes. Single explosions in competent rock usually generate strong P waves with higher frequency content than S waves. Earthquakes at similar distances show stronger S waves with richer high frequency content than P waves. In areas with substantial sedimentary cover, P and S waves from single explosions have comparable frequency content, but S waves are usually more energetic than P waves. P to S spectral amplitude ratios at high-frequencies (above 10 hz) separate most single and multiple-hole instantaneous explosions from earthquakes.

INTRODUCTION

We present spectrograms of ground velocity recorded at regional distances from ripple-fired quarry blasts, from single-shot explosions, and from earthquakes. Our goal is to contribute to the evaluation of spectrograms as a basis for discriminating between these three types of seismic sources.

We recognize that a number of special studies have pointed out the utility of spectra and spectrograms for discrimination, including the occurrence of time-independent bands in spectrograms (Baumgardt and Ziegler, 1988; Smith, 1989; Hedlin *et al.*, 1989, 1990). In addition to applying our methods of computation to published data for chemical explosions in Kazakhstan, USSR, we have sought to evaluate where problems arise in applying spectrogram methods of discrimination to seismic data routinely acquired in Norway and the Northeastern U.S. In this way, we are able to report on a variety of practical experiences with using available frequency ranges to achieve discrimination. Thus, we are interested in: (1) the effect of different signal-to-noise ratios; (2) the effect of different delay times (for ripple firing), compared to the sampling interval (for recording seismic motion); and (3) consequences of different geological conditions, especially in the vicinity of the source.

We find that fairly good discrimination capability can be demonstrated in several different regions, with a variety of delay time patterns and diverse geological settings. However, for purposes of evaluating the method and as an essential part of delineating where it works well, it is necessary to pay particular attention to failures. In some cases, these failures will provide a guide to what new types of data may be needed for more successful discrimination.

Thus, in the spirit of emphasizing the negative, we find discrimination based on spectrograms is inadequate or questionable in the following cases: (1) for blasts with delay times shorter than about four times the sampling interval of the recording system; (2) for blasts with very irregular delay times; (3) for recordings with an inadequate signal-to-noise ratio; and (4) for shots in rocks of low rigidity. In addition, spectral banding can develop from factors other than a multiple source (e.g.,. resonances along path as shown by Sereno and Orcutt (1985).or near the recording site; electronic noise in the recording system). It is important that the ambient spectral characteristics of the recording site and the near receiver path be well known.

In sections that follow, we describe applications of the spectrogram technique to regional seismic waves recorded from chemical explosions in three different parts of the world: Kazakhstan, USSR; Northeastern US; and Norway. For the Northeastern US we show spectrograms of ripple-fired and single-shot chemical explosions, and earthquakes, obtained from standard recordings acquired by the New York State Seismic Network. A final section discusses the underlying causes of success and failure of the spectrogram method of discrimination. Various source models for chemical explosions are briefly described in Appendix A. In Appendix B, we provide some details of our multitaper procedure for obtaining spectrograms (i.e., spectra of a moving window).

A Note on Terminology - We use *P wave* to denote all first arrival P waves on the records with a group velocity of greater than about 4 km/s without further classification and likewise *S wave* is used to denote all S waves arriving with group velocities of about 3.6 km/s. *Frequency content* is used to indicate that there is substantial energy above background level in the frequency band of interest. The term *time dependent spectral peaks* is used to describe the typical earthquake spectrogram with peaks of high amplitude, limited in temporal extent and associated with the arrival of characteristic phases such as P and S. *Time independent spectral peaks* are prominent spectral bands, limited in frequency content, that extend throughout the duration of the seismogram.

Chemical explosions may be classified into single explosions, multiple-hole instantaneous explosions and ripple-fired explosions, depending upon the time delays and shooting patterns

used. *Multiple hole instantaneous explosions* are distributed single explosions designed to be detonated within a very short time interval (an 8 msec interval is one standard used for regulatory and practical purposes in the mining industry). *Ripple-fired explosions* typically consist of 20 to 50 such instantaneous explosions with separate and larger delays between them. Almost all chemical explosions above about one ton are ripple-fired (Richards et al., 1991).

DATA ANALYSIS

Frequency-time displays (spectrograms) of seismograms are useful tools to study the frequency content of entire seismic waveforms observed at local and regional distances (e.g., Hedlin et al., 1989; Smith, 1989). They are especially helpful when contrasting the time dependent peaks in the spectrograms typical of most earthquakes with the presence of time-independent spectral bands observed in spectrograms from many ripple-fired mining blasts.

In this study, the following steps were taken to calculate spectrograms of regional seismograms:

1) Record segments were selected starting from about 10 sec prior to the first arrival P waves in order to obtain estimates of the back-ground noise.

2) Data were demeaned and band-pass filtered using a third order Butterworth filter over the pass band where the instrument response is not more than 6 db below the peak response.

3) Spectral estimates were calculated for each time window (usually about 4 sec) by applying the adaptive multitaper spectral estimation method of Thomson (1977; 1982).

4) Spectral estimates for the whole seismogram were achieved by moving the time window with offset of about 0.75 of the window length between each successive time window.

5) Final spectral estimates of all time windows were displayed in time-frequency space using a continuous curvature surface gridding algorithm (Smith & Wessel, 1990).

We experimented with various methods of presenting the three dimensional (time, frequency, amplitude) spectral data, including spectra of short time segments, contours of spectral amplitude and wire line (perspective) views. No single visualization draws out the relevant features in all cases. To provide a consistent presentation of all analyses, we present all spectrograms as wire-line diagrams. In some cases, we describe, in the text, features which may not be conspicuous in the wire line figures alone; these are usually features which were observed more clearly on contour plots of spectral amplitude or on individual spectra.

CHEMICAL EXPLOSIONS IN EASTERN KAZAKHSTAN, USSR

We first test applicability of the spectrogram calculation as a discriminator between ripple-fired chemical explosions and single- or multiple-hole instantaneous shots by using data from eastern Kazakhstan, USSR collected during 1987 by the Natural Resources Defence Council and Soviet Academy of Sciences (Figure 1). Detailed information regarding the stations is given in Berger et al. (1988) and Gurrola et al. (1990). Five events were analyzed, two of which (*c* and *d*, Table 1) were also analyzed by Hedlin et al. (1989). The events are near the eastern Kazakhstan nuclear test site and include two chemical explosions (Chemex 1 and 2; see Given et al., 1990), and three other events suspected to be mining blasts (Thurber et al., 1989). Seismograms used were recorded by 3-component seismometers both at the surface and in 90 m deep boreholes. The seismographs have flat response to ground velocity between 0.3 - 65 hz and 1.2 - 65 hz for the surface and borehole instruments, respectively. The data were sampled at 250 samples/sec. Spectrograms were calculated for 4 sec time windows with offset of 3 sec (0.75 times window length) between successive windows.

Chemex 1 consisted of a linear array of 30 boreholes with about 10 m spacing between each hole. Each borehole was drilled to a depth of about 25 m in water-saturated clay and filled with

equal amount of TNT for all boreholes. Total charge weight of 10,000 kg was used and all holes were detonated simultaneously (Given et al., 1990). Subshot time errors were better than about ± 10 msec and all subshots were contained underground. Thus, the event was a typical multiple-hole instantaneous shot.

The spectrograms from Chemex 1 (Figure 2) are characterized by strong time-dependent spectral peaks associated with the arrivals of P and S waves. A broad spectral band at about 5-6 hz which extends through the P and S wave coda is observed on all three components at both stations and suggests that it must be a characteristic of the propagation path. There are no clear time-independent spectral bands at high frequencies. Note that the initial P waves are stronger than S waves and have higher frequency content (maximum of 14 hz vs. 8 hz).

Another controlled explosion, Chemex 2, was detonated at the western boundary of the Kazakh test site. It was a 20 t shot in a 17 m deep horizontal mining tunnel in granitic bedrock (Given et al., 1990). The P waves at BAY are weak compared to the P waves at KKL, which is at a similar distance, and the records are dominated by strong S waves (Figure 2). This explosion was not well-contained and blew out to the surface along the shafts (Given et al., 1990), which may account for the weak P wave excitation.

The seismograms for event c (Figure 3) are characterized by strong P and S wave arrivals and at KKL a clear Rg phase is observed. There are clear spectral bands at about 5, 22 and 33 hz on all three components at both stations, as well as a set of weak spectral bands at about 11, 17 and 28 hz. The broad spectral peak near 5 hz is very similar to that observed from Chemex 1 and Chemex 2 (Figure 2) which seems to be the ambient spectral band for efficient propagation in this region. The clearer and more consistent spectral bands indicate that the event was a ripple-fired blast with subshot delay times of about 90 msec (for Δf=11 hz) or 167 msec (Δf= 6 hz) (see Appendix A).

Event c was also analyzed by Hedlin et al. (1989). While their spectrogram techniques are similar to ours, there are differences in window length, overlap etc. In addition, they used ground acceleration, whereas we have used the raw data (ground velocity) in all of our calculations. In order to provide a direct comparison of the two methods, we present in Figure 4 the spectrogram of ground acceleration for event c at station BAY, which can be compared with Figure 5 of Hedlin et al. (1989).

The spectrograms calculated for event *d* on both the surface and borehole instruments at BAY and KKL also yielded consistent spectral bands at 8, 14-16, and 22-24 hz (Figure 5). This event generated strong P waves but weak S waves on the vertical components at both stations. For event *m* (Figure 6) only a single, rather broad high-frequency spectral band at about 20-25 hz is observed at BAY ($\Delta \approx 100$ km). The frequency content of the seismic waves from this event is quite different from the other events, c and d, and the records are dominated by longer period Rg and Lg phases.

In order to assess the effect of near surface site response on the observed spectral bands, we calculate spectral amplitude ratios between the signal at the surface and at the borehole for event *d* at the stations BAY and KKL (Figure 7). The spectral ratios are almost constant at frequencies below about 12 hz on the Z-component, while the spectral ratios are flat only up to 7-8 hz on both horizontal components. The spectral ratios of both horizontal components at KKL show considerable quasi-frequency bands between 8 and 15 hz (Figure 7). Otherwise, the spectral ratios at higher frequencies show no coherent bands and vary randomly along the wave train. This might be expected if part of the seismic energy at high frequencies consists of randomly scattered waves between the borehole level and the surface.

Note that the spectral ratios as well as raw time series suggest that the signals from the surface sensors have slightly higher frequency content than the signals from the borehole sensors at both stations. This is contrary to most previously reported comparisons between surface and borehole sensors. Hauksson et al. (1987) reported significantly lower frequency content at the surface compared with the signals at depth in a 1500 m deep borehole in the Los Angeles basin, California, which they explain as due to due to stronger near surface attenuation (see also Blakeslee

& Malin, 1991). Cranswick (1988) argues that the fractured and jointed near-surface material at a "hard rock" site excites resonant modes which are characterized by a frequency content higher (above 20 hz) than the frequencies of the modes themselves. Shearer and Orcutt (1987) showed an example of signals from a borehole (124 m) and ocean bottom seismometer (OBS) in an oceanic environment. In their Figure 13, it is clear that the signal from the ocean bottom instrument has higher frequency content than the signal from the borehole, due to destructive interference of waves reflected at the sediment-basement interface on the borehole signal and strong reverberation of shear wave energy in the sediments for the OBS signal. Thus, if the seismograph responses of the KKL and BAY given in Berger et al. (1988) are correct, then the near-surface weathered and fractured portion of bedrock (Paleozoic/early Mesozoic granite) at the KKL site has a response which enhances the frequency content on the surface sensor relative to the borehole signal, in particular at about 8-15 hz. It also suggests that there is very small difference in Q between near-surface and at depth of 90 m. At BAY there is no sign of such site resonance.

EXPLOSIONS AND EARTHQUAKES IN NEW YORK

The New York State Seismic Network (NYSSN) has been operated by Lamont-Doherty Geological Observatory since the early 1970's (Sbar & Sykes, 1977). The NYSSN consists of about 25 short-period, high-gain seismographs, including three 3-component sensors at some stations (Figure 8). Data are telemetered in analog mode and recorded digitally. The NYSSN spans the main structural provinces of the eastern U.S., including the Precambrian Grenville North American shield (~1.2 b.y.) exposed in the Adirondack Mountains, the St. Lawrence rift in northern New York, the Paleozoic Appalachian platform in the western and central part of the state, the Appalachian front and crystalline overthrust sheets in eastern New York and western Vermont, the Newark Mesozoic rift basin and the Cretaceous-Cenozoic Coastal Plain of northeastern New Jersey (Stanley & Ratcliffe, 1985; Taylor, 1989; Yang & Aggarwal, 1981). The area covered by the NYSSN has numerous active quarries and mines and has a moderate level of seismicity. Thus, seismic data from the NYSSN provide an excellent opportunity to study high-frequency regional seismic wave propagation in diverse geologic settings and to test several discriminators between ripple-fired quarry blasts, instantaneous (single-hole or multiple-hole) chemical explosions and earthquakes.

The stations of the NYSSN have either 1 or 2 hz seismometers (HS-10) and their response to ground velocity is flat from the seismometer natural period to 25 hz (6 db level). Data are recorded at a sampling rate of 100 samples/sec and provide useful information up to at least 25 hz.

NYNEX Explosions

We start our analysis using data recorded on the NYSSN for controlled explosions from the Ontario-New York-New England Seismic Refraction Experiment (NYNEX) conducted by the USGS, the Air Force Geophysics Laboratory and the Geological Survey of Canada during September, 1988 (Luetgert et al. 1990, Mangino & Cipar, 1990). A total of 35 single-hole shots were detonated at 23 shot points almost equally spaced on a 640 km long profile trending roughly east-west (Figure 8). For most shots, the explosives were loaded into a single 0.2 m diameter drill hole cased to bedrock that varied in depth from 49-55 m. A few shots were detonated in water and in sediments. Ammonium nitrate was used as explosive and the charge size in each shot ranged from 270 to 2100 kg, with the majority of shots near 1000 kg (Mangino and Cipar, 1990). Most of the shots were fairly well recorded by NYSSN stations in the Adirondack Mountains and adjacent western Vermont. Two of the largest shots (the largest shot of 2100 kg in hard rock and an especially well-coupled shot of 1360 kg in water) were also recorded at most of the more distant stations of the NYSSN.

The NYSSN seismic record section from NYNEX single-hole shot #20 is displayed in Figure 9. Note that Figure 9 is a group velocity section, in which seismograms are plotted as a function of group velocities (distance/time), instead of more conventional time sections. Thus, time

scales, which remain linear for each seismogram, are increasingly compressed with distance, giving the impression of higher frequency content at greater distances. The group velocity section emphasizes seismic energy traveling with constant group velocities and the section reveals the local variation of seismic velocities across the whole network more clearly than a conventional time section. Over the distance range 150 to 230 km, major first P energy arrives with group velocities of about 6.1 to 6.3 km/sec. For the distance range between 260 and 380 km, the group velocity increases to 6.5 km/s. The stations at the shorter ranges are all located in or near the St. Lawrence rift, while the stations at the greater ranges are all in the Adirondack Mountains. At the station TBR (Δ=462 km), waves traveling in the top of the mantle, Pn and Sn, arrive with group velocities of 7.2 and 4.3 km/sec. At distances less than 400 km, Lg waves arrive with group velocities between 3.5 and 3.7 km/sec across the whole section. At TBR in southern NY (Figure 8), the relative amplitude and duration of Lg in the wave train have decreased substantially. This station is at the New York - New Jersey border, suggesting that Lg propagation is disrupted by the Appalachian platform lying along the path. Thus, the section shows effects caused by lateral velocity and structural variations associated with major geologic provinces in the region.

The observed data from the simple sources of single-hole shots of the NYNEX experiment provide us with basic information regarding the source areas and paths in this region. We then proceed to analyze other types of more complex seismic sources, such as quarry blasts and earthquakes.

Single-hole shots fired in competent bed rock - Spectrograms observed at HBVT, FLET and WNY from a single-hole shot in competent bed rock (NYNEX shot #7) are displayed in Figure 10. For this and other records from shots in competent rock, the spectrograms are characterized by time-dependent spectral energy distribution (i.e. the seismic signals show strong energies associated with the arrivals of P and S wave, otherwise the seismic energy is distributed fairly randomly in both frequency and time). P waves have higher amplitude at higher frequencies (above 10 hz) than S waves at all stations in the distance range 10-200 km. At distances greater than 100 km, spectrograms at some stations appear to show apparent spectral bands, but these are not uniform through the whole seismogram trace and are not shown consistently at all stations. Thus, these spectral bands appear to be due to propagation path effects.

Single-hole shots in water filled quarry sites - Spectrograms at stations MEDY, PTN, ECO and WNY for shot # 20 (Figure 8) are shown in Figure 11. Although this explosion is a single shot, the spectrograms in Figure 11 show clear spectral bands centered at about 5 and 7.5 hz and a weaker band at 11 hz. These spectral bands are present at all stations. This shot was detonated in a water-filled quarry (Mangino & Cipar, 1990) and so the spectral bands are likely due to a combination of an odd harmonic series with fundamental $f_0 = v/4h$ (where v = speed of sound in the water, h=water depth), an odd harmonic series with fundamental $f_1 = v/4d$, (d=detonation depth) and the complete harmonic series with fundamental $f_2 = 1/t$, where t=first bubble pulse period (Weinstein, 1968). For this shot, $h \approx d \approx 195$ m (Luetgert, per. comm, May, 1991), which gives f_0 of 1.9 hz. If the observed spectral bands are related to the 3rd, 5th and 7th harmonic series, respectively, then $f_0 = f_1 \approx 1.6$ hz. Assuming v=1.509 km/s at 25°C (Press, 1966), the detonation depth, d, is estimated to be about 236 m which is about 20% higher than the known depth. It is noted that higher order harmonics are not apparent in the observed spectrogram mainly due to increasing attenuation at the higher frequencies. Based on the banding revealed in the spectrograms, this event could be identified as a multiple shot source; however, our knowledge of the source shows that the multiplicity results from reverberations in a water column, rather than a ripple-fired explosion.

The observed amplitudes from this shot are an order of magnitude higher than the amplitudes from other shots with similar charge size at similar distances, showing the much more efficient coupling of seismic energy for underwater shots compared to boreholes. It is also interesting to note that the frequency content of S waves (1-15 hz) at most of the stations from this shot is higher than or comparable to P waves (1-12 hz); whereas, the opposite is observed on records from the largest NYNEX explosion, shot #1 (Table 2) at similar ranges.

Single-hole explosion in a sedimentary layer - The presence of a strong Rg phase on regional seismograms has been claimed to be indicative of a shallow focal depth and the existence of shallow, low velocity zones near the surface (e.g.,., Kafka, 1990). Events at such shallow depths are usually presumed to be explosions. NYNEX shot #10 was detonated in sediment at the southern end of the Lake Champlain Valley (Figure 8; Table 2). This shot provides a good example of the effects of a source in a sedimentary layer. Seismograms from this shot are characterized by arrivals of two distinct packets of energies for both the P and S waves at many stations, and by the presence of a strong Rg phase with group velocity of about 2.9 km/s and large amplitude to distances of at least 80 km (Figure 12). At most of the stations, two packets of P waves arrive with group velocities of 6.4-6.5 km/s and 5.6-6.1 km/s, respectively, while S waves have group velocities of 3.6 km/s and 3.1-3.3 km/s, respectively. Typical spectrograms are displayed in Figure 13. P waves at most stations have a spectral peak at about 5-10 hz, while the S waves have a broader frequency content of between 2 and 10 hz. Rg phases are confined to a frequency band below about 2 hz.

Sedimentary layers along the path produce apparent time-dependent arrivals of packets of P and S waves; however, there is no discernable time-independent spectral banding. The seismograms from this shot show that P waves have lower frequency content than the other shots detonated in more competent rock (cf. Figure 10), and that S waves have frequency content comparable to P waves at most of the stations. The strong S waves with higher frequency content may be due either to the more efficient excitation of S for a explosive source in the sediment or because much of the P wave energy is trapped in the sedimentary layer and progressively converted to S as the wave propagated from the source to receiver.

Quarry blasts

There are several active mining areas in upstate New York and western Vermont (see Table 3; Figure 8). We analyzed seismogram data recorded on the NYSSN from about 100 quarry blasts in the area and compared them with single-hole shots of the NYNEX experiment.

Comparison between single-hole shots & quarry blasts. Seismogram data from a quarry (R1) in Washington County, Vermont (Table 3, Figure 8), which is close to the NYNEX shot points #7 and #8, provided the opportunity to compare quarry shots with single-hole shots for almost identical source receiver paths (Figure 14). Spectrograms for the blasts at R1 show that there are weak but clear spectral bands at about 4-5, 7.5-8, 10, 12.5 and 15 hz with equal spacing of about 2.5 hz. These spectral bands are observed at all stations recording this and three additional events from R1. These clear spectral bands suggest that these quarry blasts were ripple-fired and that there was about 400 msec time delay between subshots or groups of subshots.

A comparison of the quarry blasts at R1 with single-hole shots in the distance range 50-220 km indicates that the overall frequency content of both P and S waves is lower for the quarry blasts than for a single-hole shot at comparable distances. The most striking differences are above 10 hz, where the P waves from the single hole shots are much stronger than S, whereas for the quarry blasts, the S waves are stronger than P over a broad frequency band. Thus, the quarry blasts appear to generate S waves more efficiently than P waves.

Quarry blasts with strong Rg excitation. Figure 15 shows spectrograms from three stations for four of the eight blasts we studied from mining area R2 (Table 3; Figure 8). Seismograms from the blasts in this area show a strong Rg spectral peak below 2 hz (cf. Figure 13). Many of the spectrograms (especially those for 11/28/89) show clear banding with frequency spacing of 2.5 - 3 hz, corresponding to predominant delay times about 330-400 msec. While these events are all from the same quarry, there are striking differences in the character of the waveforms recorded at the same station (especially MIV) from one event to another. These differences in waveform and spectral banding suggest that there are considerable fluctuation in delay times and sub-charge sizes. A strong and relatively broad spectral peak at about 15-20 hz for the events on 06/10/89 and 10/07/89 may be produced by interference between irregular delay times or caused by spatial extent

of the blast pattern. This accentuation of the high frequencies is in sharp contrast to the spectral form observed from R1 (Figure 14).

Quarry blasts with apparent single hole nature: Fifteen quarry blasts from the area R3 (Table 3; Figure 8) were analyzed. In the examples shown in Figure 16, there is no clear spectral banding and the spectral shapes are similar to those observed from the single hole NYNEX shots (Figure 10). Seismograms from these events are characterized by very strong high frequency P waves and relatively weak S waves at frequencies higher than 10 hz. We suspect that these blasts are multiple-hole instantaneous shots or shots with very short time delays between subshots (shorter than 30 msec, since the maximum frequency we can analyze with confidence is about 35 hz). While there is little doubt that these are quarry blasts (based on their location and origin times and since all 15 events which occurred over a two year period had similar characteristics) they cannot be identified as such based on spectral character alone.

Earthquakes in the Adirondack Mountains

Many ripple-fired quarry blasts can be identified by using the presence of spectral bands as a discriminator. However, discrimination between earthquakes and instantaneous (single- or multiple-hole) shots is not possible using this method alone, since neither type of seismic source would be expected to show spectral banding. In the following sections, to find a reliable discriminator for earthquake sources, we analyze known earthquakes and compare them with our results for explosions in the same regions.

Comparison of single-hole shots and earthquakes NYNEX shot #13 is within a few km of the epicenters of several aftershocks of the October, 1983 Goodnow earthquake (m=5.2, h=7.5 km). Although the source depths are different, their paths to most of the more distant stations are nearly identical. A comparison of the NYNEX shot with one of the Goodnow aftershocks is shown in Figure 17. The NYNEX records are characterized by initial strong P waves with high frequency content (5-25 hz) followed by S waves with slightly lower frequency content (between 1-20 hz) at most of the stations in the range 20-135 km. Therefore, for the explosion there is a distinct difference in the frequency content between P and S waves. The aftershock shows a weak initial P wave compared to S. The frequency content of both P and S waves (about 1-20 hz) is comparable at most of the stations in the ranges out to 135 km. In contrast to the explosion, therefore, the earthquake shows little difference in frequency content between P and S, but a strong difference in amplitude.

The difference between the earthquake and explosion is most pronounced at frequencies above 10 hz. In this band, the P/S spectral ratio is higher for the explosion than for the earthquake. At lower frequencies, the ratio is small for both sources because of the strong S wave generation in this band. Therefore, the P/S spectral amplitude ratio in the frequency band 10-25 hz can discriminate these aftershocks from single-hole shots. Other earthquakes and explosions in the region the show consistent P/S spectral amplitude ratios at high frequencies.

Quarry blasts and earthquakes in Southern New York & New Jersey

Earthquakes and numerous quarry blasts in southern New York and northern New Jersey provide an important test of the spectrogram method in seismic discrimination, since a large part of the area is covered by the thick sediments of the Newark Basin, raising the possibility that time-independent spectral bands can be acquired during propagation through highly reverberating, shallow, low velocity horizons.

Simple chemical explosion in sedimentary basin in New Jersey: The accidental explosion at a surface chemical storage facility near Newark, New Jersey (S1, Table 5) can be treated as a single hole instantaneous shot, though the source characteristics should be different from high-velocity explosives. The explosion was well recorded by 15 stations in the distance range 13 to 260 km (Figure 18). Strong Rg phases are observed at distances out to about 100 km. The frequency content of both P and S wave onsets is extremely low and confined to below about 7-8 hz. This

low frequency content may be due to a low corner frequency as expected from a large elastic radius due to low rigidity subsoil surrounding the source (Sharpe, 1942), or slow velocity of the explosion, or both. S wave excitation is much more efficient than the P waves from this explosion, suggesting strong P to S conversion.

Spectrograms calculated for this event show clear spectral bands at 1.5-2 hz from the initial onset into the later coda, due to resonances in the shallow, low velocity horizon. The stations in the NW quadrant have another weak but still undeniable spectral band at about 4.5 hz (e.g, TBR) and we interpret this band as due to an S wave resonating in the upper sedimentary layer. In this direction, a basaltic flow is exposed on the surface and it is thought that the basin has the form of sandwiched layers of Jurasic and Triassic terrestrial sediments interbedded with the basaltic layers. Spectral peaks should occur as an odd harmonics series with fundamental $f_1 = n/4T$, where T = P or S wave travel times in the resonating layer (Haskell, 1962). For S wave velocity of 3.5 km/s, the thickness of the layer is estimated to be about 0.6 km. Seismograms from this event show that the spectral bands below about 5 hz can be easily acquired during propagation through reverberating layers, such as the Newark Basin.

Quarry blasts in southern New York & New Jersey Among numerous quarry blasts in this area, we show examples from two blasts at quarry S2 (Table 5; Figure 19). Spectral bands at 1.5-2, 11, 15 and 21 hz are observed for both blasts at all available (seven) stations. The spectral band at 1.5-2 hz and at 5 hz at some stations can be interpreted as due to path effects as discussed earlier. The spectral bands for the event on 12/30/87 show a more regular pattern and sharper spectral peaks, suggesting longer total duration of the blast and more uniform delay times. From the clear spectral banding, there is little doubt that these events are ripple-fired quarry blasts, with source time delays of about 200 msec.

These events show that high frequency spectral bands can still be recognized in the spectrograms from ripple-fired quarry blasts even when the paths cross a large portion of a reverberating sedimentary basin. The lower frequency part of the spectrograms (below about 5 hz) is not useful for identifying different types of source in this environment, due to apparent spectral bands arising from layer resonances.

Earthquakes in southern New York & New Jersey: Although a large part of the region is covered with thick sediments, seismograms from earthquakes in this region do not show clear Rg phases, due probably to the deeper depth of the earthquakes. Seismograms from earthquakes that occurred in four different locations were analyzed (Table 4, Figures 8 and 20). There are no clear spectral bands in the spectrograms and the energy is more or less randomly distributed in time and frequency. Note that the P/S spectral amplitude ratio in the high frequency band (10-25 hz) successfully discriminates all events as earthquakes rather than instantaneous explosions.

RIPPLE-FIRED MINING EXPLOSIONS IN NORWAY

As a final example of the use of the spectrogram method, we test the ability to identify spectral banding in a very poor signal-to-noise ratio environment, but where we have good specification of the explosion and hence the expected banding characteristics.

Seismogram data recorded at the Norwegian seismic array (NORESS) have been extensively used by many researchers for detecting and discriminating earthquakes and chemical explosions (e.g., Baumgardt and Ziegler, 1988; Hedlin et al., 1990). Previous studies were mainly conducted for quarry blasts from two large mining area, Titania and Blåsjø in southern Norway. These studies used data recorded on the conventional NORESS short-period channels with sampling rate of 40 sample/sec, thus they were able to interpret spectral modulation only up to 20 hz (Ringdal et al., 1986).

We use data recorded on the special 3-component high-frequency seismic element at NORESS which has nearly flat response between 10-55 hz and a sample rate of 125 samples/sec (Ringdal et al., 1986). The spectrograms are calculated with a time window length of 6 sec. Detailed information on the events analyzed are listed in Table 6 and locations are depicted in

Figure 21. Note that since all of the delay times are 45 msec, the frequency spacing of the spectral peaks should be about 22 hz (1/45 msec), so that any spectral banding may not have been observed using the conventional NORESS short-period seismogram data. All of the explosions are at large distances from NORESS for their size and the signal-to-noise ratios are very low. The major portion of seismic energy arrives in the frequency band between 2 and 10 hz and shows weak time-dependent spectral peaks associated with P, S and Lg arrivals. The spectral peak near 25-28 hz on most of the spectrograms is apparently a noise signal, since it exists prior to the expected arrival of the explosions.

Explosions N1, N2 and N3 (Figures 22 and 23) are all at the same location. The largest of these N1 and N3 show a spectral band at 23-25 hz that is most obvious on the horizontal components for N1 (unfortunately the horizontal components for N3 are not available). The smallest explosion, N2, does not show any consistent banding above 15 hz on the vertical. The spectral band at about 15-18 hz on the horizontals could be due to variations in delay times of up to about 30 %, but is more likely related to higher noise in this band. It is reported that seasonal noise during May is higher (especially at high frequencies) due to melting snow causing increased flow in a river near the site (Feyen, 1987).

More complete information was available to us regarding a ripple-fired explosion at Åheim about 353 km NW of NORESS (Figure 21). Different amounts of explosive were used in each subshot, with the largest subshot of 2.1 ton. Distribution of maximum charge in each subshot and the resulting spectral modulation are depicted in Figure 24. Even though the signal noise level for this event is even lower than in Figure 22, a broad spectral band at about 23 hz is observed on all three components (see Figure 25).

This analysis of ripple-fired explosions whose basic detonation characteristics were known *a priori* shows that even when the signal-to-noise ratio is very low it is possible to observe spectral bands due to source multiplicity resulting from ripple-firing. Care must be taken, however, to first identify background noise, from electronic or cultural sources, that may also produce spectral banding.

DISCUSSION

The high-frequency seismic spectra of characteristic crustal phases, such as Pn, Pg and Lg, on regional records provide important data for determining attenuation in the crust and for studying seismic source properties. During the Advanced Research Project Agency's project "VELA UNIFORM" in the early '60s, many researchers studied seismic records from chemical explosions and earthquakes (e.g. Devine & Duvall, 1963; Frantti, 1963; Pollack, 1963; Willis, 1963). Most of these earlier works were based on the seismic signal in the lower part of the short period band, usually below 10 hz.

Recently, high-frequency spectra (up to 30 to 40 hz) from regional events have been advocated as a crucial tool in seismic verification of low-yield coupled and fully decoupled underground nuclear explosions (e.g. Evernden et al., 1986). The possibility of a reduced threshold test ban treaty, which could bring the magnitudes of the largest permitted nuclear explosions down to those of large industrial explosions, has renewed interest among seismologists in the seismic signals from chemical explosions, particularly from ripple-fired explosions. Data from recently installed high quality, high-frequency seismograph stations and networks now make it possible to investigate whether high frequencies can improve the ability to discriminate between different types of explosions and earthquakes.

Ripple-fired explosions are particularly interesting to seismologists, since they are usually large enough to excite strong seismic signals and since they produce complex signals rich in high-frequencies. Spectral modulation due to the repetitive source in ripple-fired explosions has been observed at high-frequencies by several researchers. Baumgardt & Ziegler (1988) found spectral modulation in events believed to involve ripple-firing, but not in the spectra computed from earthquake records. Greenhalgh (1980) and Smith (1989) observed prominent spectral peaks in the P wave spectra produced by ripple-fired mining explosions in the Mesabi Iron Range, northern

Minnesota. Hedlin et al. (1989, 1990) observed similar spectral modulation in the high-frequency spectra of suspected quarry blasts in eastern Kazakhstan, USSR, but not in the spectra of multiple-hole instantaneous calibration shots detonated at similar ranges. Hedlin et al. (1989) found that the modulation was independent of time from the onset arrival to well into the Lg coda and demonstrated the usefulness of spectrograms (time-frequency plots) in deciphering time-independent spectral bands. These researchers all suggested that the spectral bands due to ripple-firing could be used to discriminate quarry blasts from other seismic events, in particular from regional earthquakes.

In other studies related to the use of high-frequency regional seismogram data in seismic verification, several researchers (e.g. Bennett & Murphy, 1986; Evernden et al., 1986; Chael, 1989) used the spectral content of P phases, the character of depth sensitive phases such as Rg and the P to S spectral amplitude ratio from regional earthquakes and nuclear explosions in and near the Nevada Test Site (NTS) and in eastern Kazakhstan, USSR.

Ripple fired explosions and spectral banding The observations of clear spectral banding by Hedlin et al. (1989, 1990), Smith (1989) and in some of our examples (Figure 3, 5, 15 and 19) show that this feature can be used to identify certain types of ripple fired quarry blasts. From some of our observations, however, it is clear that banding is not a universal feature of all quarry blasts (e.g.,. Figure 16). Spectral banding will be most obvious when multiple, narrow bands appear as parallel lines on the spectrogram (e.g.,. Figure 3). This requires that there be little variation in the delay times used in the ripple firing sequence and that the length of the delays produce multiple bands that lie within the passband of the observing seismic equipment. Variations in the delay times broaden the peaks of the spectral bands, causing interference between adjacent bands and making individual bands difficult to distinguish. If the delays are very short, the blast becomes similar to an instantaneous explosion and the first multiple spectral band is likely to lie above the passband of the recording system. If the delay times are less than four times the sampling interval of the recording equipment, only one band can lie in the passband of the recording equipment. For long delays, the frequency separation between bands decreases and the interference between adjacent bands makes them difficult to observe. For longer delays, the duration of the source also increases, distributing the energy release over a longer time interval and decreasing the effective size of the source. In the frequency band observed at regional distances, it is unlikely that spectral bands closer together than 2-4 hz can be distinguished, placing an upper limit of a few hundred milliseconds on the delay times that can be identified. Thus for typical recording systems (digitizing rates of approximately 100 samples per second), observations of spectral banding may be limited to explosions with shooting delays on the order of a few tens to a few hundred milliseconds.

Even in those cases where irregular delay times in quarry explosions do not lead to clear individual spectral bands, there remains a strong enrichment of high frequencies (especially at later times in the seismogram) relative to instantaneous explosions (e.g.,. Figure 15). This spectral modulation appears to enhance the S wave energy at high frequencies more effectively than for P waves. This general enrichment of high frequencies for S waves causes the spectrograms from quarry explosions with irregular shooting delays to become more similar to those from earthquakes. Note that, because of the modification of the high frequency portion of the spectrum, seismogram data from unknown industrial explosions should be used with caution in studies of attenuation.

In attempting to use spectral banding in the identification of ripple fired explosions, care must be taken to isolate other sources of time independent spectral bands. Mechanical, cultural and electronic sources of monochromatic noise can produce spectral bands that can be identified by careful analysis of background noise.

The spectrogram method also should be used with caution at lower frequencies in areas with near surface sedimentary layers, since resonances in these layers can also produce distinct spectral bands. The excitation of Rg and an enhancement of S waves relative to P waves are closely associated with the presence of low velocity surface layers along the path. Sedimentary layers appear to have a stronger effect when they occur near the source rather than along the path or close

to the receiver. This can be explained as efficient P to S conversion occurring in the sedimentary layer. The conversion to S is more efficient near to the source simply because more convertible P energy is available near the source region than for later parts of the path with longer elapsed time. Thus, the decrease in frequency content of the P wave is much more substantial than for the S wave.

Instantaneous Explosions In Table 7 we summarize the frequency characteristics of the instantaneous explosions we have analyzed. Instantaneous explosions in competent bed rock produce strong P waves with high frequency content (NYNEX shots #7 and #3, Figure 10 and Figure 17), while explosions in sediments (Chemex 1, Figure 2; NYNEX shot #10, Figure 13) and in the subsoil (Newark explosion, Figure 18) generated P waves with much lower frequency content (Table 7). The differences are greater than can be explained only by stronger attenuation for paths in sedimentary structures. Differences in both frequency content and amplitude can be explained in terms of the material properties surrounding the shot holes (Appendix A). NYNEX shot #10 in sediments has f_c of about 10 hz, while NYNEX shot #7 in competent bed rock has f_c of at least 20 hz. From equation A.2, elastic radii of 90 and 45 m may be deduced for shots #10 and #7, respectively. These are probably over-estimates, since the corner frequencies are not corrected for attenuation and other effects during propagation. Equation A.3 shows that the displacement amplitude is proportional to the cube of the elastic radius of the explosion and inversely proportional to the rigidity. Consequently, shots in a low rigidity medium produce larger amplitudes than shots in a medium with greater rigidity. This explains the large amplification (a factor of about 5) for shot #10 when compared with shots with similar charge sizes from the competent rock sites during the NYNEX experiment.

If spectral banding is observed, it provides an excellent diagnostic to discriminate ripple fired explosions from other types of seismic sources. This diagnostic does not, however, distinguish between instantaneous explosions and earthquakes. In analysis of spectrograms from a variety of sources, we have found that the spectral amplitude ratio of P to S, especially at high frequencies, provides a complementary tool for discriminating between instantaneous explosions and earthquakes. At lower frequencies (less than 10 hz) there is little difference between the P/S ratio for instantaneous explosions and earthquakes - the S wave amplitudes are almost always much greater than the P wave from both type of events. At higher frequencies, however, we observe that the P waves are stronger and that the P/S ratio is much higher for the explosions than for earthquakes. The P/S ratios from the contained instantaneous explosions (NYNEX, Chemex#1 and R2 in the Adirondack Mountains) are usually higher than 0.5, while the ratios are generally much lower than 0.5 for the data from the earthquakes in the Adirondack Mountains and southern New York and New Jersey area. This characteristic of the P/S ratio shows consistent behavior over several different shot hole rock types and conditions (water saturated or dry) as well as over a wide variety of paths. Therefore, we believe that the P/S (or Pg/Lg) spectral amplitude ratio at high frequencies can be a robust discriminator between earthquakes and instantaneous explosions.

The P/S ratio does not always distinguish ripple fired explosions from earthquakes. Some ripple-fired quarry blasts show apparently stronger S waves than P waves (Figure 14) and the seismograms appear to be similar to those from earthquakes. The corresponding spectrograms, however, clearly show that the strong S wave energies, especially at high frequencies, are due to reinforcement of spectral amplitudes from ripple-firing. When clear spectral banding is observed, the spectrogram technique provides a method for initially identifying these events as ripple fired explosions. If irregular delays in the shooting sequence result in broad spectral enhancement at high frequencies, instead of clear spectral bands, these ripple explosions become difficult to distinguish from earthquakes. Since earthquake source functions may consist of individual sub events, irregularly spaced in time, this similarity between earthquakes and explosions with irregular firing delays is not surprising.

CONCLUSIONS

Temporal variations in the spectra of regional seismograms can be used to discriminate between various types of seismic sources, including instantaneous explosions, ripple fired explosions and earthquakes. The spectrogram technique provides a convenient method to display the time dependent variations in spectra. An advantage of the spectrogram methods over other techniques is the use of the complete regional seismogram trace rather than isolated phases, such as Pn, Pg and Lg. However, like other discriminators based on spectral estimates, the method requires data with high signal-to-noise ratio, especially at high frequencies, and the use of stations where the spectral response is well known and there is minimal spectral contamination from local resonances.

The diagnostic features of regional waveforms that can be identified using the spectrogram technique include high frequency spectral banding, excitation of Rg and spectral variations in the ratio of P to S energy. Table 8 summarizes the application of these features to discrimination between different types of seismic sources.

The observation of regular spectral banding at high frequencies is the most reliable discriminant and distinguishes between ripple fired explosions and other types of seismic sources. This banding is clearly observed only for explosions in which the delay times between sub-explosions are stable and on the order of tens to hundreds of milliseconds.

The presence of Rg on regional seismograms is diagnostic of a shallow source in sediments. This usually implies an explosive source, but it is possible that very shallow earthquakes can also produce Rg. The Rg phase may be weak or absent from explosions in areas without sedimentary cover. Thus the use of Rg as a discriminant requires knowledge of the geology and crustal structure near the source.

The P/S spectral amplitude ratio at high frequencies provides a complementary tool to discriminate between instantaneous explosions and earthquakes. At frequencies below 10 hz, instantaneous explosions and earthquakes have similar spectral characteristics. Above 10 hz, the instantaneous explosions produce stronger P waves relative to S. A high P/S spectral ratio above 10 hz appears to be a stable characteristic of instantaneous explosions, distinguishing them from earthquakes. This diagnostic is less useful at longer distances for paths with significant sedimentary cover, when conversion of P to S wave energy along the path enhances the S waves and diminishes P.

The least reliable discrimination is between earthquakes and ripple fired explosions with irregular delays. Explosions with irregular delays produce spectral enhancement at high frequencies, especially for S, but do not produce the diagnostic spectral banding. The enriched S at high frequencies produces spectra that are more similar to those from earthquakes. This similarity between earthquakes and irregular explosions presumably results from the similarity in the temporal nature of a multiple earthquake rupture and a random multiple explosion source. In these cases, discriminators based on source depth (such as the presence of Rg) may assist in the identification of the source type.

APPENDIX A

SOURCE SPECTRA FROM CHEMICAL EXPLOSIONS

Single-hole explosion

A common method of generating seismic waves for land seismic exploration or of cracking rocks for extracting useful ores is to detonate an explosive charge at some depth in a cylindrical hole or in a spherical cavity. In order to interpret the seismic data collected from such chemical explosions, a mathematical model of the source is required. In this Appendix, we briefly summarize the characteristics of the source spectra of two source models pertinent to chemical explosion. The basic features of the source spectra from explosions are similar to those from earthquakes. The source spectra from models for explosions in a cylindrical or spherical cavity are characterized by a flat spectral level from low frequencies up to the neighborhood of the corner frequency ($f_c \approx k\ V_P/a$, where k=constant, a=radius of cavity) after which the spectrum decays with f^{-2} at high frequencies. These models for the seismic radiation are for the far-field, that is, the cavity radius is small compared with the smallest wavelength of interest and the observations are made at distances that are large compared with the cavity radius.

Spherical cavity model - A simple explosive source model suggested by Sharpe (1942) and Latter et al. (1961) assumes that the explosives are loaded in a spherical cavity of radius, a, in a homogeneous, perfectly elastic medium. Assuming that a uniform initial pressure, p_0, is applied to the interior surface of the cavity, this model yields the far-field P wave displacement spectrum at distance r (Evernden et al. 1986),

$$U(r, \omega) = \frac{p_0\, a^3}{4\mu}\frac{1}{r}\left(\frac{Vp}{Vp^2 - 0.75\, a^2\omega^2 + iVp\, a\, \omega}\right)e^{i\omega Vp/r} \qquad (A.1)$$

where $\omega=2\pi f$, p_0=initial pressure, μ=rigidity, a=elastic radius, Vp=P wave speed. The elastic radius or *radius of the equivalent cavity* is a function of the strength of the material and the size of the charge detonated. For the same charge sizes in different media, the elastic radius is inversely proportional to the rigidity of the medium surrounding the shot hole.

The corner frequency, f_c, of the P wave spectrum produced by an explosion in a circular cavity is given by (Sharpe, 1942),

$$f_c = \frac{\sqrt{2}}{3\pi}\frac{Vp}{a} \approx 0.15\,\frac{Vp}{a} \qquad (A.2)$$

The corner frequency may be used as a measure of frequency content of the single-hole explosions. The above relation predicts that smaller elastic radius (≈ smaller charge size) should produce higher corner frequency. Note that the earthquake source spectrum based on the circular fault model (Brune et al., 1979) has the corner frequency,

$$f_c = \frac{1}{3}\frac{Vs}{a_0} \approx \frac{\sqrt{3}}{3}\frac{Vp}{a_0} \approx 0.58\,\frac{Vp}{a_0}$$

where a_0 =radius of the circular fault model.

From the eq. (A.1), the low-frequency spectral level is,

$$|\,U\,(\omega\rightarrow 0)\,| \propto \frac{p_0}{4\mu}\,a^3 \qquad (A.3)$$

For this simple model, there is no angular dependence for the seismic radiation. Note that Sharpe(1942) gives $U(\omega\rightarrow 0) \propto p_0 a^2/\mu$.

Cylindrical cavity model - Heelan (1953) and Abo-Zena (1977) obtained expressions for the far-field seismic radiation from an infinite, circular cylindrical hole filled with explosives in an isotropic, elastic material, while Glen et al. (1986) obtained a far-field displacement from an axisymmetric, cylindrical cavity with radius a_0 and length 2b. Assuming that the pressure p is applied to the interior surface as uniform step in time with no spatial variation, that is, $p = p_0 H(t)$, the Fourier transform of the displacements are (Glen et al., 1986),

$$| U(\omega, \theta) | = \frac{1}{V} \frac{p_0}{2\mu} \, b \, a_0^2 \, R_{P,S} \left(\frac{1}{1+(1-2\beta)\eta_0^2+\beta\eta_0^4} \right)^{\frac{1}{2}} \left| \frac{\sin x}{x} \right| \qquad (A.4)$$

where $\eta_0 = \omega a_0 / V_{P,S}$, $x = \omega b \cos\theta / V_{P,S}$ and $\beta = (1-\nu)/2(1-2\nu)$, ν=Poisson's ratio. $R_{P,S}(\theta)$ are the P and SV wave low-frequency radiation pattern. For an instantaneous explosion on a finite length of the cylinder, the P wave radiation is a function of the Poisson's ratio, ν, (ν=1/4 for crustal material with Vp=6 km/s and Vs=3.5 km/s) and angular position (take-off angle), θ, while SV wave radiation is a function of angular position (Abo-Zena, 1977). For ν=1/4, the low-frequency radiation $R_{P,S}(\theta)$ are (Heelan 1953; Abo-Zena, 1977; Glen et al., 1986),

$$R_P(\theta) = (1 - \frac{1}{3}\cos^2\theta)$$

$$R_S(\theta) = \sin^2\theta$$

The P wave radiation pattern is a doughnut shape in 3 dimensions and is similar to the radiation from a dipole without torque. The SV radiation pattern is four-lobed and has a maximum at θ =45° and is similar to the one obtained from a vertical strike-slip motion (Kennett, 1983, 90p).

The spectral amplitude at low-frequencies (as $\omega \rightarrow 0$), is:

$$| U(\omega \rightarrow 0, \theta) |_{\theta \neq 0} = \frac{p_0}{2\mu} \, b \, a_0^2 \, R_{P,S}(\theta)$$

Thus, the low-frequency spectral amplitude from a cylindrical cavity shows dependence on cylinder length b and angular position, θ.

In case of the cylindrical cavity, the corner frequency is dependent on θ and aspect ratio, $A = b/a_0$. For a fixed radius, the corner frequency, f_c is inversely proportional to the cavity length b (Glen et al., 1986),

$$f_c = \frac{Vp}{4b}$$

More realistic source process involves a progression of the detonation with velocity, V_e (6 to 7 km/s for high-speed explosives, Telford et al., 1970, 310pp) and exponential decay of the initial pressure (p_0) with time as, $p(t) = p_0 H(t+z/Ve) \, e^{-b(t+z/Ve)}$. For this case, the source radiation is more complex and dependent on length of cylinder and detonation velocity. The radiation is stronger in the direction of progression (Abo-Zena, 1977).

Spectral modulation due to ripple-fired explosions

Most large commercial chemical explosions are ripple-fired for fragmenting bedrock during quarrying and open-pit mining. Ripple-fired explosions commonly consist of several rows of subshots detonated with time delays ranging from a few to hundreds of milliseconds. Often, an

individual row of charges may be treated as a sequence of single explosions f[illegible] almost simultaneously (within a few msec.) and may be considered as a multiple-hole ins[illegible]neous explosion. The time delay between rows may be significantly longer, leading to an [illegible]ended temporal source and spectral reinforcement at high frequencies.

Assuming a constant time delay, δt, between each subshot and ignoring (for the moment) the finite spatial extent of an actual quarry blast, the ripple-firing can be viewed as a comb function in which each spike is separated by δt and represents a subshot. The Fourier transform of this function is another comb function in the frequency domain. The spectral peaks occur at the harmonics of $1/\delta t$. The frequency spacing, δf, between these spectral peaks is $\delta f = f_i - f_{i-1} = 1/\delta t$. Thus, the time delay is equivalent to the inverse of the frequency spacing of the spectral peaks.

The total duration, t_n, of an entire blast sequence, consisting of n subshots (or rows), is $(n-1)\ \delta t$. Due to the finite duration of the blast sequence,the width of the spectral peaks is $2/t_n$, since the finite duration is equivalent to a multiplication of the comb function by a box-car function of finite duration, t_n, which has a finite width of $2/t_n$ in the frequency domain (see Smith, 1989).

Assuming a uniform source spectra for all subshots, the source spectrum of the ripple-fired explosion can be represented as the source spectrum of a subshot multiplied by a comb function. Thus, the spectral reinforcement associated with the time delay in ripple-firing yields apparent amplification at the preferred frequencies. However, the spectral peaks at frequencies higher than the corner frequency of the source spectrum may not be easily discernable on observed spectra, since the source spectrum will roll off as f^{-2} at higher frequencies.

Additional time delays are introduced in ripple-firing due to the spatial pattern of the shot holes. Assuming that the location of the i-th shot is specified by $(x_i, y_i, 0)$ in a uniform half-space in the Cartesian coordinate system with origin at the initiation point of the quarry and let x = North, y = East and z = vertically down. For a station lying at azimuth, ϕ (measured clockwise from the North), the total time delay T_i for the i-th shot hole is,

$$T_i = -\sin\theta/V\ (x_i \cos\phi + y_i \sin\phi) + t_i$$

where θ=take-off angle for the ray from source to receiver, $\sin\theta/V = p$ is the ray parameter, t_i=shot's delay time relative to the initiation point. Note that a similar formula, eq. (5) of Smith (1989), eq. (7) of Hedlin et al., (1989) and eq. (3) of Hedlin et al., (1990),

$$T_i = p\ (x_i^2 \sin^2\phi + y_i^2 \cos^2\phi)^{\frac{1}{2}} + t_i\ ,$$

is incorrect and the maximum error from the equation is a factor of about $\pm\sqrt{2}$.

When the time delays are short enough (as in multiple-hole instantaneous shots), the spectral amplitude undergoes a simple scaling which is approximately equal to the number of single-hole shots in a row. This linear superposition of single explosions is observed for small-scale explosions in alluvium (Stump and Reinke, 1988) and in large mining explosions (Greenhalgh, 1980). It is used as a practical amplitude scaling relation for ripple-fired explosions, known as "maximum charge per delay interval" (Devine & Duvall, 1963). This amplitude scaling is explained easily by the fact that the source spectrum of a ripple-fired explosion is the product of the source spectrum of a subshot multiplied by a comb function in the frequency domain as discussed earlier. Thus, the spectral amplitude from ripple-fired explosion is not scaled to the "total charge" of the whole blast sequence, but to the "maximum charge per delay interval".

APPENDIX B

SPECTROGRAM ANALYSIS

The requirements for a reliable spectrogram are a fine resolution in frequency with unbiased representation of true spectral estimates and a smooth sampling in time. However, it is difficult to achieve good resolution in time and in frequency simultaneously, since the sampling in frequency, Δf, and time window length, T, are inversely related to each other ($\Delta f = 1/T$). In order to have good sampling in time, it is necessary to take short time windows and, therefore, it is desirable to have a reliable algorithm to calculate unbiased spectral estimates for short time windows. Recently, the adaptive multitaper spectral estimation method has been successfully used in various seismological applications requiring reliable spectral estimates for short time series (e.g., Park et al., 1987a, 1987b; Menke et al., 1990). In this Appendix, we summarize aspects of the multitaper algorithms we used in the spectral estimates.

Multitaper spectral estimation algorithm

The procedure is based on properties of the discrete form of prolate spheroidal wavefunctions which are simultaneously time- and band-limited (Slepian, 1978). The method uses several of these lowest-order prolate spheroidal wavefunctions as data tapers in an adaptive sense and it provides optimum spectral leakage when used for short time series (Thomson, 1982). Park et al.(1987a) called the method "multitaper". The multitaper spectral estimates are formed as a weighted sum of the eigenspectra. The essence of the method is that it provides protection against the biases due to the leakage of spectral energy at high frequencies and gives variance reduction to the spectral estimates. The discrete Fourier transform of an untapered record yields a poor estimates of the high frequency roll-off due to spectral leakage, while the commonly used single taper (e.g.,. Hanning or cosine taper) minimizes the leakage, but tends to misrepresent nonstationary seismic data by applying unequal weights to the data.

The seven lowest-order 4π prolate spheroidal wavefunctions are used as data tapers (eigentapers) for the spectral estimate in all spectrogram calculations. The 4π prolate eigentapers used were generated using a time-frequency band width product of 4 (e.g. for a time length, N, of 128 points at S samples per second, the frequency band width, W, is 4S/N. The eigentapers for other time lengths used were obtained through a spline interpolation as described in Park et al. (1987a). The first six eigentapers were used in this study, since there is little to be gained by using more than the first 2NW (i.e., 8 in this study) eigentapers (Thomson, 1977). Further details of the method are given in Thomson (1977; 1982) and Park et al. (1987a, 1987b).

Time window and frequency resolution

The time window length, T, determines the resolution in frequency, since $\Delta f=1/T$. However, the 4π prolate eigentaper used in this study reduces the resolution and a conservative estimate of its resolution is on the order of 4/T (Thomson, 1977). The choice of time window length depends on the fine structure of the spectrum to be estimated. Time windows which are too long will obscure time-dependent information associated with arrivals of characteristic crustal phases such as, Pn, Pg, Sn and Lg. Windows which are too short yield poor resolution in frequency and, consequently, give poor results in discerning any time-independent spectral bands. Minimum window lengths should be longer than the expected total duration of any source multiplicity. Large ripple-fired quarry blasts in Norway, for example, are known to have total durations of up to 1.12 sec (see section 3). In this study, we found that window lengths of about 4 sec gave the best results for the regional seismograms we analyzed. The time window lengths were adjusted for the records from near-by events ($\Delta < 100$ km) to separate P and S wave arrivals when the S-P time was shorter than about 4 sec. The shortest window length used was 2.5 sec.

The maximum frequency limit was set by the sampling rate of the data used and the frequency band over which the instrument response was flat. In most cases, the maximum frequency we analyzed was about 1/2 Nyquist frequency . We found that there was no significant seismic energy at higher frequencies and the signal-to-noise ratio deteriorated very quickly above half of the Nyquist frequency. For the seismograms recorded at larger distance ranges ($\Delta > 100$ km), there was very little seismic energy above the noise level at frequencies higher than one half of the Nyquist frequency, primarily due to stronger attenuation at higher frequencies. Records from short ranges showed substantial high frequency energy above noise level up to very close to the Nyquist frequency, however, the signal-to-noise ratio deteriorated very quickly above half of the Nyquist frequency.

The high frequency portion of the spectra may be enhanced relative to lower frequencies by using the first derivative of the velocity record as in Hedlin et al. (1989) and Smith (1989). However, we have chosen to use the recorded time series without taking the first derivative in order to preserve overall spectral characteristics of the observed regional phases. The times series used were uncorrected for instrument responses and thus all data presented correspond to ground velocity, since all the instrument characteristics were almost flat to velocity over the frequency band of interest.

Overlapping method

In order to achieve better resolution in time, successive time windows were overlapped. The choice of the offset, or relative spacing between time windows, is not straightforward and needs some consideration. If the windows are spaced closely in time relative to their length, no information is missed, but the time windows are highly correlated with each other and the additional processing results in computational inefficiency. If the time windows are spaced too far apart, the procedure is statistically inefficient. The relative spacing between time windows depends largely on the choice of the data taper. The 4π prolate eigentaper we used has optimum information recovery when the offset is about 0.25-0.3 of their length (Thomson,1977).

If the offset between adjacent time windows is more than 0.57 of the window length, the spectral estimates of each time window will be essentially uncorrelated at any given frequency (Thomson, 1977). To obtain statistically unbiased spectral estimates, we have imposed a condition that the correlation between successive windows be minimal. Thus, we have used a relatively large offset of 0.75. In most of the data analyzed, the identification of spectral banding due to source multiplicity was unaffected by using this longer offset. As pointed out by Thomson (1977), the covariance between spectral estimates from two time windows having very narrow resonances results in the spectral estimates being correlated for large values of the offset. Shorter offsets of 0.29, 0.43 and 0.57 were tested and there was not sufficient improvement in resolution to warrant using the shorter offsets.

ACKNOWLEDGMENTS

We thank Art Lerner-Lam who helped us in the early stages of this work. Javier Pacheco provided his subroutines for multitaper spectral estimates. Russell Such assisted us throughout the project providing us with much of the NYSSN data used. Doug Johnson helped us with instrument responses for stations of the NYSSN. NRDC data were provided by researchers at the University of California, San Diego. Jerry Carter of Center for Seismic Studies, Washington D.C. provided seismograms of controlled chemical explosions. Doug Anderson of Vibra-Tech Engineers, Inc., explained practical and theoretical features of delays. We thank Roger Hansen, Anders Dahle and Frode Ringdal of NORSAR for providing us with NORESS high-frequency element seismogram data and detailed information regarding mining operation in Norway. This research was sponsored by the Defense Advanced Research Projects Agency and monitored by the Air Force Geophysics Laboratory (now Phillips Laboratory) under Contract No. F19628-88-K-0041.

REFERENCES

Abo-Zena, A. M. (1977). Radiation from a finite cylindrical explosive source, *Geophysics*, **42**, 1384-1393.

Baumgardt, D. A. and K. Ziegler (1988). Spectral evidence for source multiplicity in explosion: application to regional discrimination of earthquakes and explosions, *Bull. Seism. Soc. Am.*, **78**, 1773-1795

Bennett, T. J. and J. R. Murphy (1986). Analysis of seismic discrimination capabilities using regional data from western United States events, *Bull. Seism. Soc. Am.*, **76**, 1069-1086.

Berger, J., H. K. Eissler, F. L. Vernon, I. L. Nersesov, M. B. Gokhberg, O. A. Stolyrov and N. T. Tarasov (1988). Studies of high-frequency seismic noise in eastern Kazakhstan, *Bull. Seism. Soc. Am.*, **78**, 1773-1758.

Blakeslee, S. and P. Malin (1991). High-frequency site effects at two Parkfield downhole and surface stations, *Bull. Seism. Soc. Am.*, **81**, 332-345.

Brune, J. N., R. J. Archuleta and S. Hartzell (1979). Far-field S-wave spectra, corner frequencies, and pulse shapes, *J. Geophys. Res.*, **84**, 2262-2272.

Chael, E. P. (1989). Spectral discrimination of NTS explosions and earthquakes in the southwestern United States using high-frequency regional data, *Geophys. Res.Lett.*, **16**, 625-628.

Cranswick, E. (1988). The information content of high-frequency seismograms and the near-surface geologic structure of "hard rock" recording sites, PAGEOPH, **128**, 333-363.

Devine, J. F. and W. I. Duvall (1963). Effect of charge weight on vibration levels for millisecond delayed quarry blasts, *Earthquake Notes*, **34**, No. 2, 17-24.

Frantti, G. E. (1963). Spectral energy density for quarry explosions, *Bull. Seism. Soc. Am.*, **53**, 989-996.

Evernden, J. F., C. B. Archambeau and E. Cranswick (1986). An evaluation of seismic decoupling and underground nuclear test monitoring using high-frequency seismic data, *Rev. Geophys.*, **24**, 143-215.

Feyen, J. (1987). NORESS noise spectral studies, noise level characteristics, *Semiannual Technical Summary*, NORSAR Scientific Report No. 2-86/87, Kjeller, Norway, 46-58.

Given, H. K., N. T. Tarasov, V. Z. Huravlev, F. L. Vernon, J. Berger and I. L. Nersesov (1990). High-frequency seismic observations in eastern Kazakhstan, USSR, with emphasis on chemical explosion experiments, *J. Geophys. Res.*, **95**, 295-307.

Glen, L. A., B. Moran, A. J. C. Ladd, K. A. Wilson and J. A. Rial (1986). Elastic radiation from explosively-loaded axisymmetric cavities, *Geophys. J. R. astr. Soc.*, **86**, 119-136.

Gurrola, H., J. B. Minster, F. L. Vernon, H. K. Given, J. Berger, and R. Aster (1990). Analysis of high-frequency seismic noise in the western United States and eastern Kazakhstan, *Bull. Seism. Soc. Am.*, **80**, 951-970.

Greenhalgh, S. A. (1980). Effects of delay shooting on the nature of P-wave seismograms, *Bull. Seism. Soc. Am.*, **70**, 2037-2050.

Haskell, N. A. (1962). Crustal reflection of plane P and SV waves, *J. Geophys. Res.*, **67**, 4751-4767.

Hauksson, E., T-L. Teng and T. L. Henyey (1987). Results from a 1500 m deep, three-level downhole seismometer array: site response, low Q values, and fmax, *Bull. Seism. Soc. Am.*, **77**, 1883-1904.

Hedlin, M. A., J. B. Minster and J. A. Orcutt (1989). The time-frequency characteristics of quarry blasts and calibration explosions recorded in Kazakhstan, USSR, *Geophys. J. Int.*, **99**, 109-121.

Hedlin, M. A., J. B. Minster and J. A. Orcutt (1990). An automatic means to discriminate between earthquakes and quarry blasts, *Bull. Seism. Soc. Am.*, **80**, 2143-2160.

Heelan, P. A. (1953). Radiation from a cylindrical source of finite length, *Geophysics*, **18**, 685-696.

Kafka, A. L (1990). Rg as a depth discriminant for earthquakes and explosions: a case study in New England, *Bull. Seism. Soc. Am.*, **80**, 373-394.

Kennett, B. L. N. (1983). *Seismic wave propagation in stratified media*, Cambridge Univ. Press, 342pp.

Latter, A. L., R. E. LeLevier, E. A. Martinelli and W. G. McMillan (1961). A method of concealing underground nuclear explosions, *J. Geophys. Res.*, **66**, 943-946.

Luetgert, J. H., S. Hughes, J. Cipar, S. Mangino, D. Forsyth and I. Asudeh (1990). Data report for O-NYNEX: The 1988 Grenville-Applachian seismic refraction experiment in Ontario, New York and New England, Open-file report 90-426, US.Dept. Interior, Geological Survey, Menlo Park, CA., 21pp.

Mangino, S and J. Cipar (1990). Data report for the 1988 Ontario-New York-New England Seismic refraction experiment: Three-component profiles, GL-TR-90-0039, Geophysics Laboratory, Hanscom ABF, MA. 143 pp. ADA221898

Menke, W., A. Lerner-Lam, B. Dubendorff and J. Pacheco (1990). Polarization and coherence of 5 to 30 hz seismic wave fields at a hard-rock site and their relevance to velocity heterogeneities in the crust, *Bull. Seism. Soc. Am.*, **80**, 430-449.

Park, J., F. L. Vernon III and C. R. Lindberg (1987a). Frequency dependent polarization analysis of high-frequency seismograms, *J. Geophys. Res.*, **92**, 12664-12674.

Park, J., C. R. Lindberg and F. L. Vernon III (1987b). Multitaper spectral analysis of high-frequency seismograms, *J. Geophys. Res.*, **92**, 12675-12684.

Pollack, H. N. (1963). Effect of delay time and number of delays on the spectra of ripple-fired shots, *Earthquake Notes*, **34**, No. 1, 1-12.

Press, F. (1966). Seismic velocities, in *Handbook of Physical Constants*, S. P. Clark Jr. ed., *Geol. Soc. Am.*, Memoir **97**, 587 pp.

Priestly, K. F., G. Zandt and G. E. Randall (1988). Crustal structure in Eastern Kazakh, U.S.S.R. from teleseismic receiver functions, *Geophys. Res. Lett.*, **15**, 613-616.

Richards, P. G., D. A. Anderson and D. W. Simpson (1991). A survey of blasting activity in the United States, Manuscript, May, 1991, 27 pp, submitted for publication in *Bull. Seism. Soc. Am.*

Ringdal, F., B. K. Hokland and T. Kværna (1986). Initial results from the NORESS high frequency seismic element (HFSE), *Semiannual Technical Summary*, NORSAR Scientific Report No. 2-85/86, Kjeller, Norway, 31-39.

Sbar, M. L and L. R. Sykes (1977). Seismicity and lithospheric stress in New York and adjacent areas, *J. Geophys. Res.*, **82**, 5771-5786.

Sereno, T. J., Jr. and J. A. Orcutt. (1985). Synthesis of realistic oceanic Pn wave trains, *J. Geophys. Res.*, **90**, 12755-12776.

Shearer, P. M. and J. A. Orcutt (1987). Surface and near-surface effects on seismic waves - theory and borehole seismometer results, *Bull. Seism. Soc. Am.*, **77**, 1168-1196.

Sherief, R. E. and L. P. Geldart (1986). *Exploration Seismology*, vol. 1, Cambridge Univ. Press, 253pp.

Sharpe, J. A. (1942). The production of elastic waves by explosion pressures, I. Theory and empirical field observations, *Geophysics*, **7**, 144-154.

Slepian, D. (1978). Prolate spheroidal functions, Fourier analysis and uncertainty -IV: the discrete case, *Bell Sys. Tech. J.*, **57**, 1371-1429.

Smith, A. T. (1989). High-frequency seismic observations and models of chemical explosions: implications for the discrimination of ripple-fired mining blasts, *Bull. Seism. Soc. Am.*, **79**, 1089-1110.

Smith, W. H. F. and Wessel, P. (1990). Gridding with continuous curvature splines in tension, *Geophysics*, **55**, 293-305.

Stanley R. S. and N. M. Ratcliffe (1985). Tectonic synthesis of the Taconian orogeny in western New England, *Geol. Soc. Am. Bull.*, **96**, 1227-1250.

Stump, B. W. and S. K. Reinke (1988). Experimental confirmation of superposition from small-scale explosions, *Bull. Seism. Soc. Am.*, **78**, 1059-1073.

Taylor, S.R. (1989). Geophysical framework of the Appalachians and adjacent Grenville Province, in *Geophysical Framework of the Continental United States*, eds: L.C. Pakiser and W.D. Mooney, Geol. Soc. Am. Memoir, 172, 317-348.

Thomson, D. J. (1977). Spectrum estimation technique for characterization and development of WT4 waveguide-I, *Bell Sys. Tech. J.*, **56**, 1769-1815.

Thomson, D. J. (1982). Spectrum estimation and harmonic analysis, *IEEE Proc.*, **70**, 1055-1096.

Thurber, C., H. Given and J. Berger (1989). Regional seismic event location with a sparse network: application to eastern Kazakhstan, USSR, *J. Geophys. Res* , **94**, 17767-17780.

US Department of the Interior, Bureau of Mines (1984). Minerals Available System Domestic Deposit Listing, US Department of Labor, Mine Safety & Health Administration, HSAC-MSHA Mailing Addresses.

Weinstein, M. S. (1968). Spectra of acoustic and seismic signals generated by underwater explosions during Chase experiment, *J. Geophys. Res.*, **73**, 5473-5476.

Willis, D. E. (1963). Comparison of seismic waves generated by different types of source, *Bull. Seism. Soc. Am.*, **53**, 965-978.

Yang J.-P. and Y. P. Aggarwal (1981). Seismotectonics of Northeastern United States and adjacent Canada, *J. Geophys. Res.*, **86**, 4981-4998.

Table 1. Explosions from Eastern Kazakhstan, USSR

Event id	Origin time Date	(h: m: s)	Latitude (°N)	Longitude (°E)	Charge weight (kg)	Area
Chemex #1[a]	09/02/87	07:00:00.3	50.2806	72.1722	10000	Karaganda
Chemex #2[a]	09/02/87	09:27:04.95	50.000	77.3367	20000	Degelen Mtn
c[b]	05/15/87	10:35:00	49.304	72.717	-	Karaganda
d[b]	05/21/87	09:16:43	50.744	73.279	-	Karaganda
m[c]	08/27/87	08:52:14	51.21	74.30	-	Ekibastuz

[a] Event time, location and charge weight from Given et al., 1990.

[b] Event id, time and location from Thurber et al., 1989.

(c) Origin time and location are approximate.

Table 2. NYNEX shots and their locations

Shot id	Origin time Date	(h: m: s)	Latitude (°N)	Longitude (°E)	Charge weight (kg)	Remark
1	09/17/88	06:04:01	44.590	69.746	2100	bed rock
7	09/17/88	04:04:00	44.179	72.237	1225	bed rock
8	09/24/88	04:00:00	44.151	72.577	910	bed rock
10	09/17/88	08:04:00	44.054	73.386	1360	sediment
13	09/24/88	06:04:00	43.968	74.2615	1040	bed rock
20	09/24/88	04:08:00	44.477	77.658	1360	water-filled
	09/30/88	04:00:00	44.477	77.658	900	water-filled

Table 3. Quarries in Upstate New York & Vermont[a]

Event id	Origin time date	(h: m:s)	Latitude (°N)	Longitude (°W)	Area Quarry	(County, State)
R1	10.23.89	21:58:37	44.14	72.48	Rock-of-ages	Washington, Vermont
R2	06/10/89	23:36:31	44.32	73.64	Lewis	Essex, NY
	10/07/89	18:19:23	44.32	73.64	Lewis	Essex, NY
	11/28/89	19:02:47	44.32	73.64	Lewis	Essex, NY
R3	05/10/88	20:40:55	44.77	72.53	Lowell	Orleans, Vt

[a] Quarry and locations from the U.S. Department of the Interior, Bureau of Mines (1984).

Table 4. Earthquakes in New York[a]

Event	Origin time date	(h: m: s)	Latitude (°N)	Longitude (°W)	Depth (km)	Magnitude	Area
E1	10/07/83	10:48:39	43.938	74.258	7.5	2.0	Goodnow aftershock
E2	10/07/83	10:59:04	43.952	74.258	7.5	2.9	Goodnow aftershock
E3	10/19/85	10:05:46	40.990	73.820	-	2.3	Ardsley foreshock
E4	01/22/89	08:27:15.9	40.884	73.942	-	2.0	Englewood Cliffs, NJ
E5[b]	10/23/90	01:34:49.9	39.535	75.552	24.0	2.9	Chesapeake Bay, NJ
E6	04/12/91	11:12:12	41.136	73.654	-	2.0	NY

(a) Location, origin time, depth and magnitude are from Quarterly Seismicity Bulletin of the NY State Seismic Network, Lamont-Doherty Geological Observatory, except (b) from PDE.

Table 5. Quarries in southern New York-northern New Jersey[a]

Event id	Origin time date	(h: m: s)	Latitude (°N)	Longitude (°W)	Area Quarry	(County, State)
S1	01/07/83	05:14:25.5	40.7083	74.1250	chemical	Newark, NJ
S2	12/30/87	19:00:10	40.991	74.611	Hopatcong	Morris, NJ
S2	02/13/89	15:07:45	40.991	74.611	Hopatcong	Morris, NJ

(a) origin times are approximate.

Table 6. Mining Explosions in Norway recorded at NORESS

Id	Origin time Date	(h:m:s)	Latitude (°N)	Longitude (°E)	Charge weight (ton/shots)	Delay time (total delay/shots)	Area
N1	01/28/86	10:18:33	66.24	14.35	149.0/22[a]	945/22[c]	Storforshei
N2	05/09/86	17:14:34	66.24	14.35	102.2/26[a]	1125/26[c]	Storforshei
N3	12/01/87	12:55:30	66.24	14.35	217.6/22[a]	945/22[c]	Storforshei
N4	05/24/89	13:35:00	62.040	5.523	9.37/8[b]	315/8[c]	Åheim

(a) total charge per total number of subshots, max. charge/subshot is unknown

(b) total charge per total number of subshots, max. charge/subshot is known.

(c) total time duration of all subshots/(total number of subshots - 1) = 45 msec

Table 7. Frequency content of instantaneous shots in various site condition

Site Condition	Path Condition	Frequency content P (hz)	S (hz)	$\Delta^{(a)}$ (km)	Rg	area
clay (water-saturated)	sediments (?)	14	8	254	yes	Kazakhstan
quarry site (water-filled)	1/2 sediments	13	15	375	yes	NYNEX #20
sediments	1/2 sediments	5-15	2-15	157	yes	NYNEX #10
hard-rock	normal	5-20	1-15	132	-	NYNEX #7
		5-25	1-20	134	-	NYNEX #13
sub-soil	basin	5	5	230	yes	Newark

(a) Maximum epicentral range considered

Table 8. Characteristics of Explosive and Earthquake Sources

Type of source	High-frequency spectral bands	High-frequency P to S ratio	Excitation of Rg
Instantaneous explosion	No	>1.0	Yes
Ripple-fired quarry blast	Yes	-	Yes
Regional earthquake	No	0.5<	Rarely

Figure Captions

Figure 1. Locations of mining blasts (c, d & m), chemical explosion (Chemex 1 and Chemex 2) and seismic stations in Kazakhstan, USSR. Epicenters of underground explosions (ISC Bulletin) are plotted as small + symbols. Degelen Mt. and Shagan River test sites are denoted as DM and SR, respectively.

Figure 2. Three-component seismograms (*bottom*) and corresponding spectrograms (*top*) at stations BAY and KKL from (a) a controlled multiple-hole instantaneous explosion (Chemex 1, Table 1) and (b) an instantaneous explosion in a tunnel (Chemex 2, Table 1). Note that a spectral peak near 45 sec in the BAY NS component for Chemex 2 results from a noise spike. Spectral amplitudes are calculated from time series which correspond to the ground velocity and are displayed on a linear scale. Time is given starting from the origin time of the event. Event id, station, component as well as epicentral distance (Δ) and azimuth (ϕ) are indicated at the upper right hand corner of each frame. Unless otherwise indicated, all spectrogram plots in later figures follow the notation used here.

Figure 3. Rotated seismograms (Z, R and T) and corresponding spectrograms at station KKL and BAY from event *c* (presumably a ripple-fired quarry blast, Table 1).

Figure 4. Z-component accelerograms and corresponding spectrograms at station BAY from event *c* and Chemex 2. Note that spectrograms are calculated for ground acceleration as in Hedlin et al. (1989) for comparison.

Figure 5. Spectrograms at station BAY and KKL from event *d* (Table 1).

Figure 6. Spectrograms at station BAY from event *m* (Table 1).

Figure 7. Spectral amplitude ratios from surface sensors and from borehole sensors at station BAY and KKL from event *d*. Time series shown are the *difference* between the surface and borehole signals and plotted for reference.

Figure 8. Locations of New York State Seismic Network (NYSSN) stations (filled squares) and events used in this study. Open circles denote NYNEX shot points and closed circles indicate epicenters of earthquakes. Locations of quarries are indicated by crosses. (a) Adirondacks and western Vermont area and (b) southern New York and New Jersey.

Figure 9. Group velocity seismic section from NYNEX shot #20 recorded on the vertical components of the short-period seismographs of the NYSSN. Each seismic trace is plotted with group velocities between 9 and 2 km/sec. Note that the horizontal axis is group velocity, not the usual time axis. Apparent changes in frequency content at greater ranges are due to increasing compression of time scales with distance. Station code and azimuth are given at the end of each trace.

Figure 10. Spectrograms at HBVT, FLET and WNY from the controlled single-hole explosion, NYNEX shot #7 (competent bed rock site). Notice the strong P waves with high frequency content relative to S waves.

Figure 11. Spectrograms at MEDY, PTN, ECO and WNY from NYNEX shot #20 (water-filled quarry site). Notice clear spectral bands at about 5 and 7.5 hz, and a weak band at about 11 hz (e.g. MEDY) due to reverberation in the water.

Figure 12. Group velocity seismic section from a controlled single-hole explosion in sediments, NYNEX shot #10. Selected vertical-component seismograms in the epicentral distance range out to 157 km are plotted for clarity. Notice the strong Rg phase at short distances (out to 70 km). P waves consist of two packet of energy with the first arriving with velocity of 6.1 - 6.5 km/sec. The S waves arrive with group velocities of 3.6 km/s and 3.3-3.1 km/s and the Rg phase arrives with group velocity of 3.0-2.9 km/s.

Figure 13. Spectrograms at HBVT, WNY, CTR and PTN from NYNEX shot #10. Notice strong spectral peaks at about 1.5 hz due to the Rg phase, and stronger S waves than P.

Figure 14. A comparison of spectrograms from a presumed quarry blast from quarry R1 (Figure 8; Table 3) at HBVT, FLET and MIV with a single-hole explosion (NYNEX shot #7) at HBVT. Notice the presence of weak but clear spectral bands from the quarry blast.

Figure 15. A comparison of spectrograms from different blasts from the same quarry, R2 (Table 3; Figure 8) at MIV, HBVT, WNY and MDV. The blast on 11/28/89 shows evenly distributed spectral energy at high frequencies and well developed spectral bands. The blast on 06/10/89 shows very strong amplitudes at high frequencies (15-25 hz). The blast on 10/07/89 shows strong amplitudes as well as considerable energy between 5 and 10 hz. Note that the differences in frequency contents are also visible in the seismograms shown.

Figure 16. Spectrograms at HBVT, MIV and PTN from quarry R3 (Table 3; Figure 8). Notice the strong P waves with high frequency content and no clear spectral bands. The spectrograms are similar to those from the single-hole explosions (cf. NYNEX shot #7 in Figure 10).

Figure 17. A comparison of spectrograms from earthquakes with those from a single-hole instantaneous explosion (NYNEX shot #13, Figure 8) at MDV, PTN and FLET. Notice clear differences in P wave spectral amplitudes and frequency content.

Figure 18. Spectrograms at AMNH, PAL, TBR, and PRIN from a surface chemical explosion in Newark, NJ. Late arrival phase at AMNH at about 45 sec is the air pressure wave traveling with speed of about 332 m/s. There is a spectral band at 1.5-2 hz at all stations due to resonances in the Newark Basin

Figure 19 A comparison of spectrograms at TBR, PAL and CRNY from two quarry blasts at the same quarry (S2; Table 5, Figure 8). Both blasts show clear spectral bands but with a slight difference in their distribution in frequencies. Blast on 12/30/87 shows spectral energy between 5-25 hz, while blast on 02/13/89 shows spectral energy between 10-30 hz. Notice the presence of strong Rg phases at all stations. The spectral band at about 5-10 hz is stronger for the blast on 12/30/87 and this event also shows longer duration of S waves.

Figure 20. A comparison of spectrograms from four earthquakes in southern New York and New Jersey (Table 4, Figure 8) at station PRIN in the epicentral distance range 87 to 124 km. Note that P waves from all four earthquakes are much weaker than S waves over a broad frequency range (5-25 hz). There are weak spectral bands associated with P and S wave arrivals, but these are discontinuous and do not extend throughout the seismogram. This apparent spectral banding may be due to source-receiver paths which lies mostly in the Newark Basin.

Figure 21. Locations of NORESS and the Åheim and Storforshei mines in Norway (Table 6). Locations of two other mining areas in southern Norway, Titania and Blåsjø, are indicated.

Figure 22 Spectrograms at the NORESS high frequency element (HFE) from a 149 ton ripple-fired quarry blast (N1) and a 102 ton ripple-fired quarry blast (N2, Table 6) in northern Norway. Phase arrivals (Pn, Sn and Lg) are indicated by arrows along the time series and the expected spectral band at 22 hz is indicated by an arrow at the upper right hand edge of the spectrogram. Note that a spectral band with constant amplitude at about 30 hz on the Z and EW components is due to seismograph noise.

Figure 23 Spectrogram at NORESS from a 218 ton ripple-fired quarry blast (N3, Table 6) in northern Norway.

Figure 24 *(Top)* Diagram of a pattern of delay times of the 9.4 ton ripple-fired quarry blast (N4 Table 6) in western Norway. Vertical scale is proportional to charge size in each subshots in tons (max. charge/subshot is 2.1 ton, delay time=45 msec) and horizontal scale is the time in msec. *(Bottom)* Spectral modulation predicted from the charge distribution shown on top (solid line) and the spectral modulation resulting from uniform charge size (dashed line).

Figure 25 Spectrograms at NORESS from a 9.4 ton ripple-fired quarry blast (N4, Table 6) in western Norway.

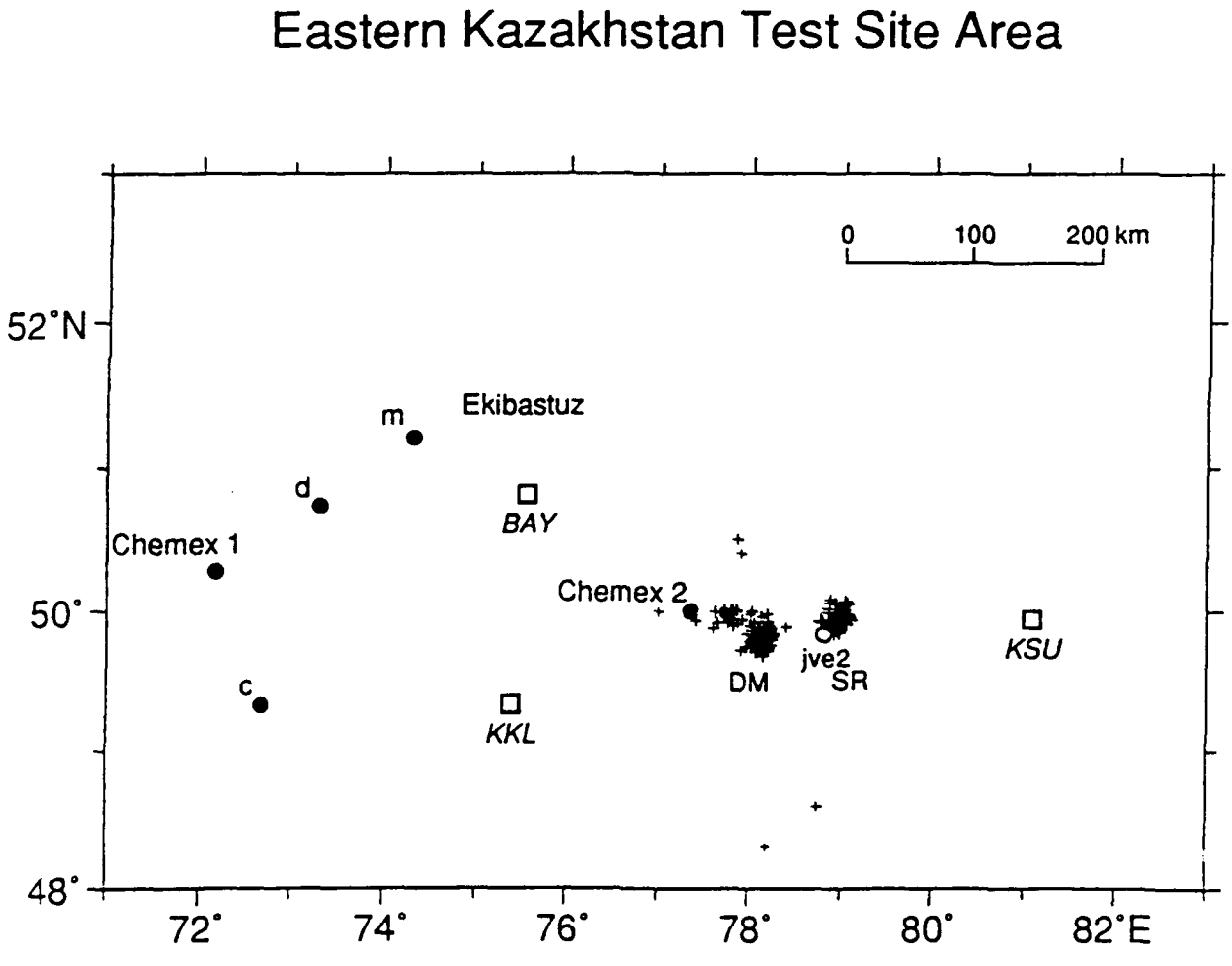
Eastern Kazakhstan Test Site Area
0
100
200 km
52°N
50°
48°
72°
74°
76°
78°
80°
82°E
m
Ekibastuz
d
BAY
Chemex 1
Chemex 2
c
KKL
DM
jve2
SR
KSU

Figure 1

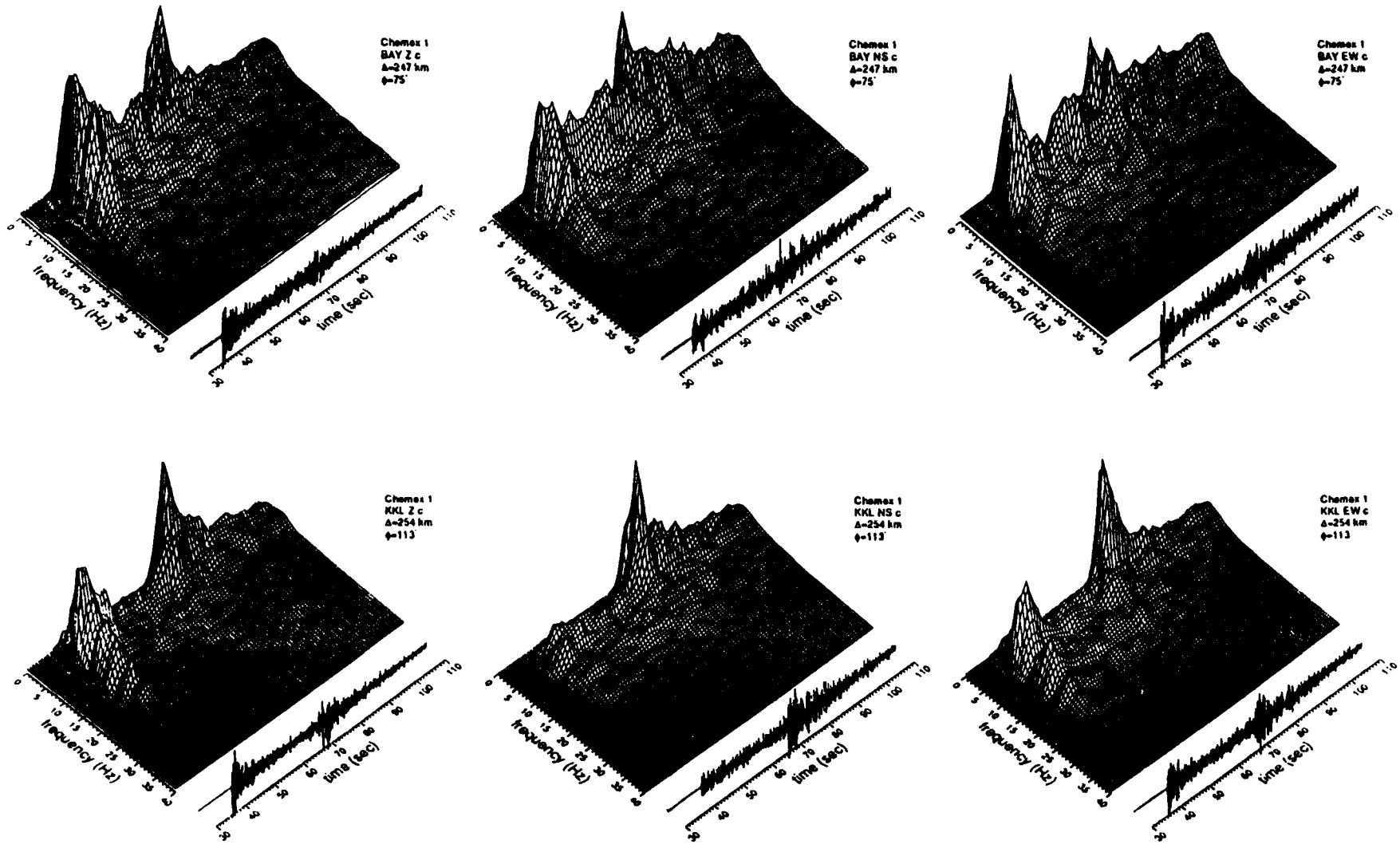
Chemex 1
BAY Z c
Δ=247 km
ϕ=75°
Chemex 1
BAY NS c
Δ=247 km
ϕ=75°
Chemex 1
BAY EW c
Δ=247 km
ϕ=75°
Chemex 1
KKL Z c
Δ=254 km
ϕ=113
Chemex 1
KKL NS c
Δ=254 km
ϕ=113
Chemex 1
KKL EW c
Δ=254 km
ϕ=113
frequency (Hz)
time (sec)

Figure 2a

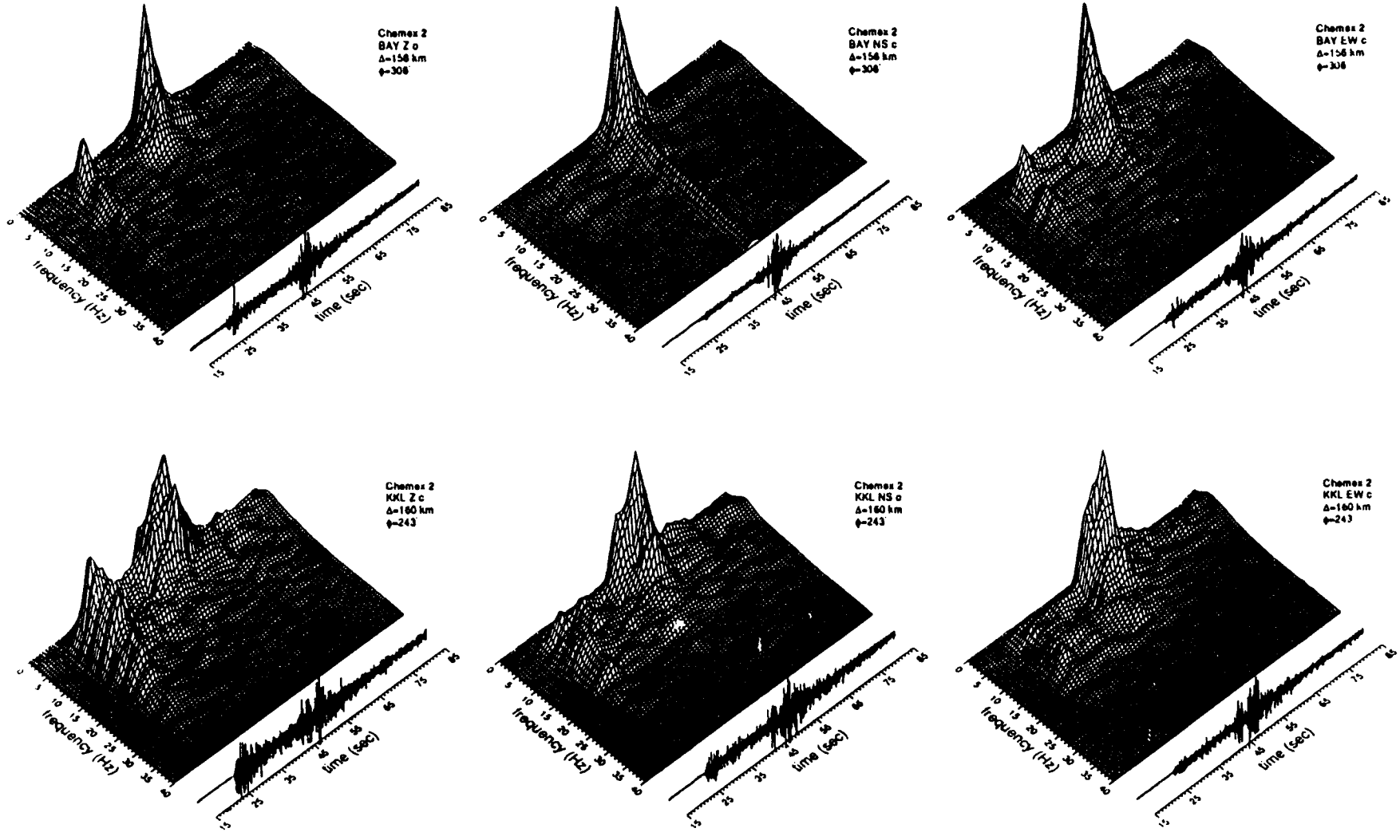
Chemex 2
BAY Z o
Δ=156 km
ϕ=308
Chemex 2
BAY NS c
Δ=156 km
ϕ=308
Chemex 2
BAY EW c
Δ=156 km
ϕ=308
Chemex 2
KKL Z c
Δ=160 km
ϕ=243
Chemex 2
KKL NS o
Δ=160 km
ϕ=243
Chemex 2
KKL EW c
Δ=160 km
ϕ=243
frequency (Hz)
time (sec)

Figure 2b

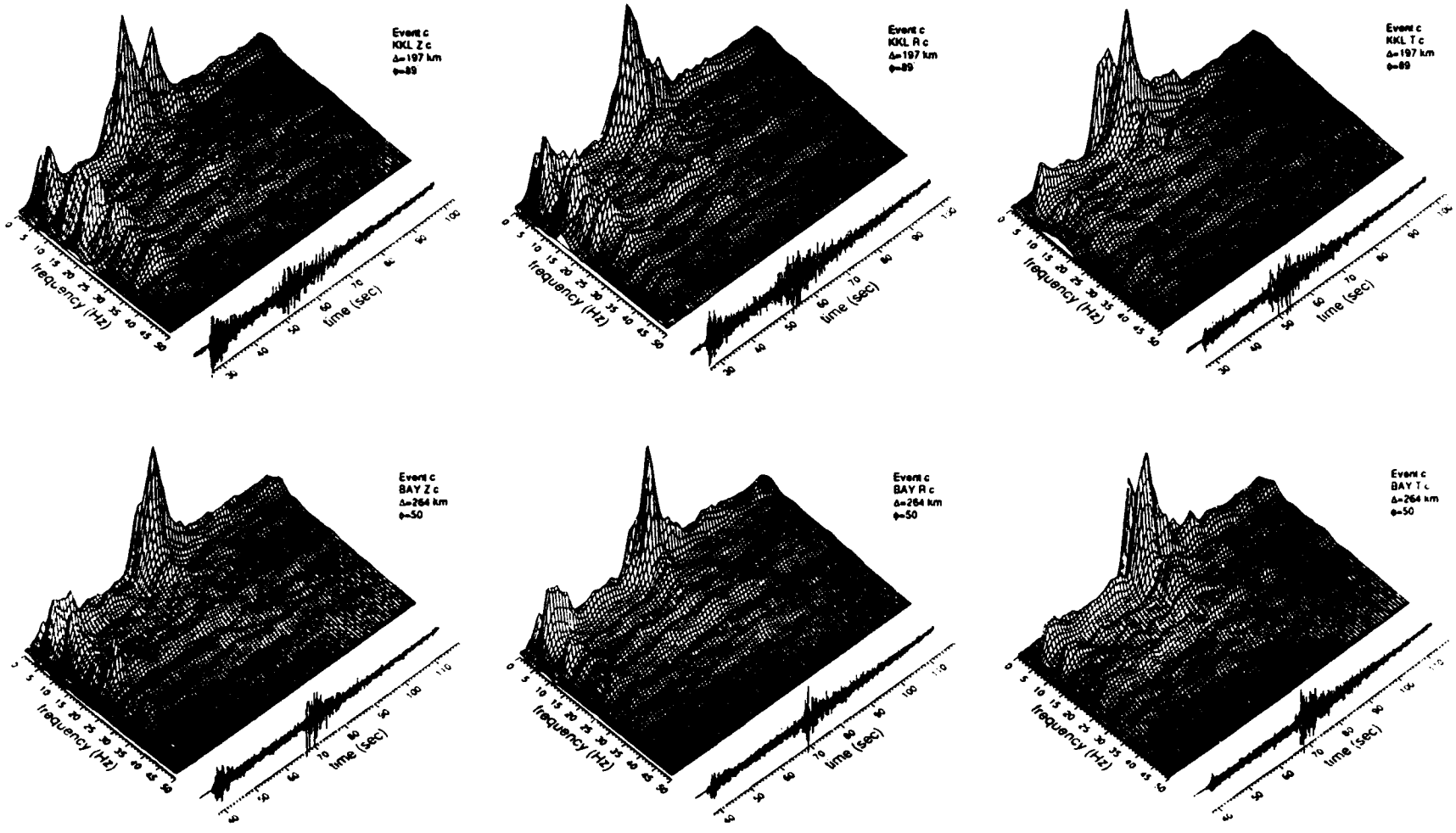
Event c
KKL Z c
Δ=197 km
Φ=89
Event c
KKL R c
Δ=197 km
Φ=89
Event c
KKL T c
Δ=197 km
Φ=89
Event c
BAY Z c
Δ=264 km
Φ=50
Event c
BAY R c
Δ=264 km
Φ=50
Event c
BAY T c
Δ=264 km
Φ=50
Frequency (Hz)
Time (sec)

Figure 3

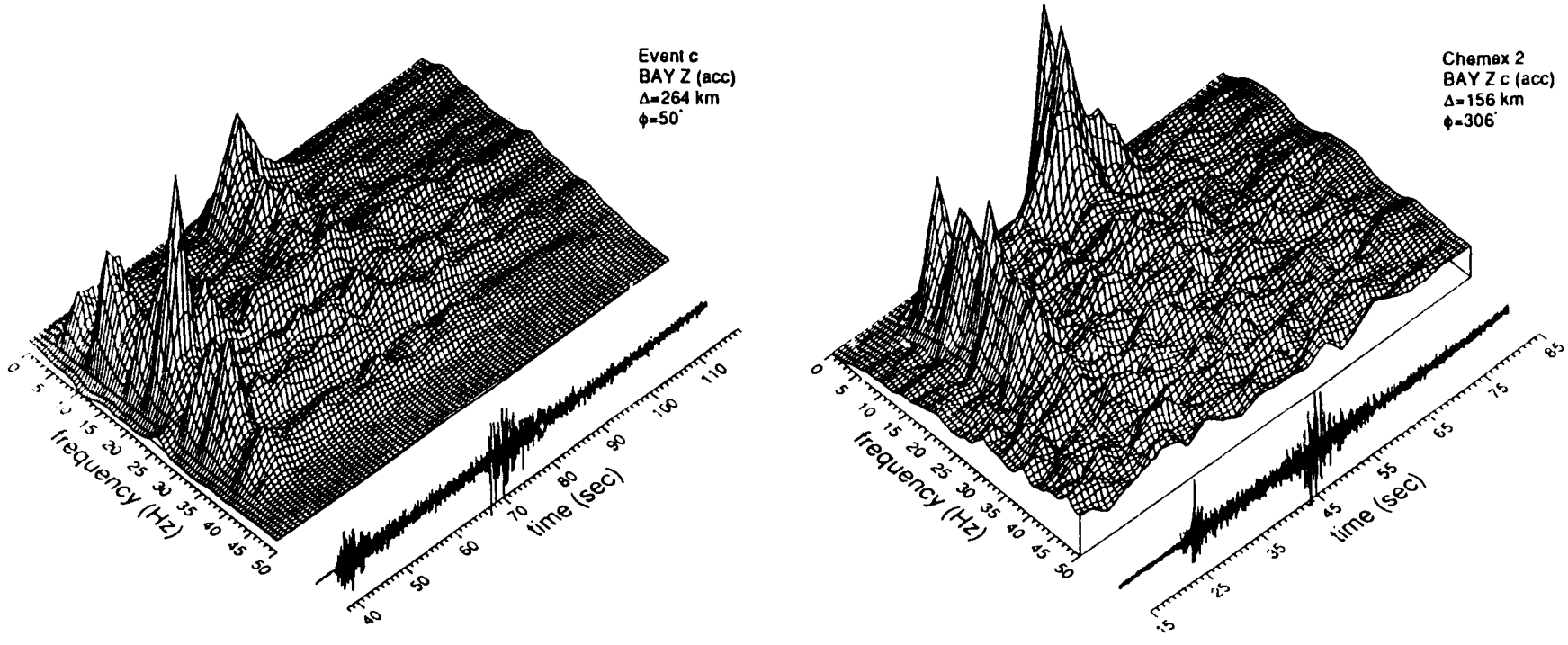
Event c
BAY Z (acc)
Δ=264 km
ϕ=50°
frequency (Hz)
time (sec)
Chemex 2
BAY Z c (acc)
Δ=156 km
ϕ=306°
frequency (Hz)
time (sec)

Figure 4

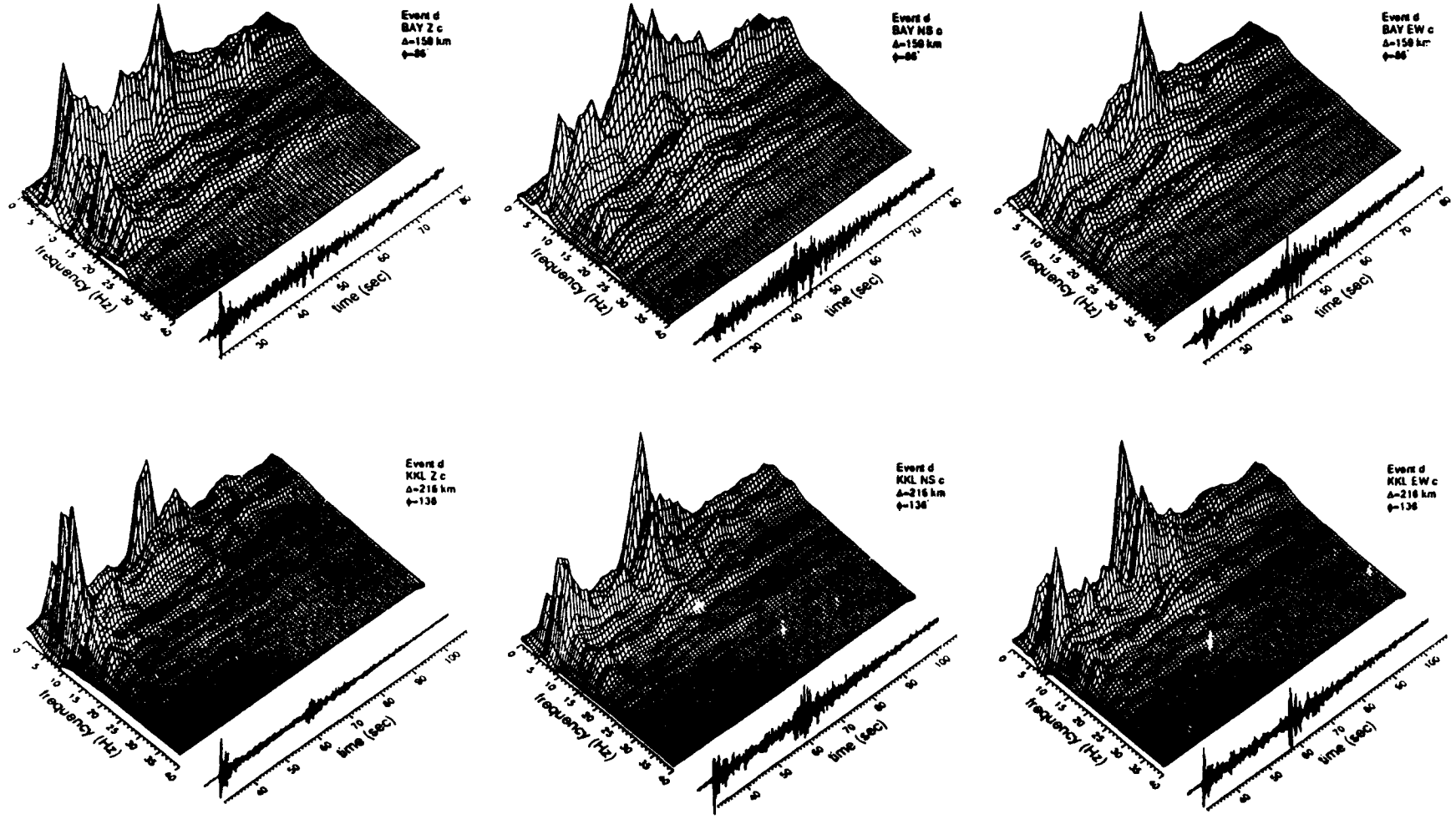
Event d
BAY Z c
Δ=158 km
Event d
BAY NS c
Event d
BAY EW c
Event d
KKL Z c
Δ=216 km
Event d
KKL NS c
Event d
KKL EW c
frequency (Hz)
time (sec)

Figure 5

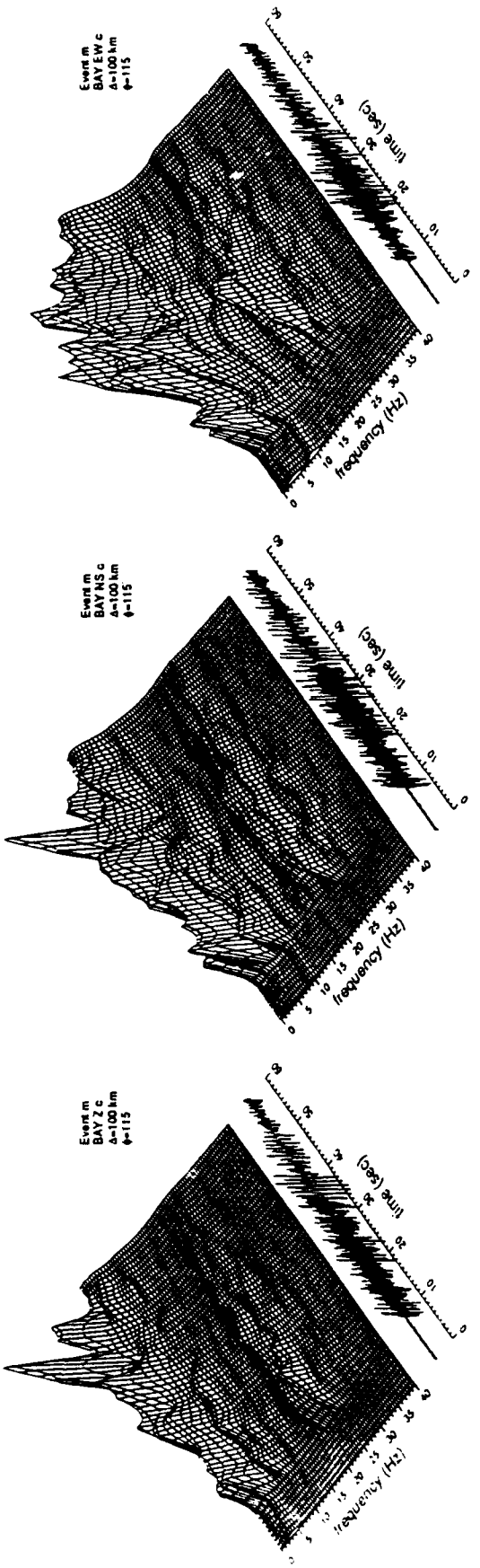
Event m
BAY EW c
Δ=100 km
φ=115
Event m
BAY NS c
Δ=100 km
φ=115
Event m
BAY Z c
Δ=100 km
φ=115
frequency (Hz)
time (sec)

Figure 6

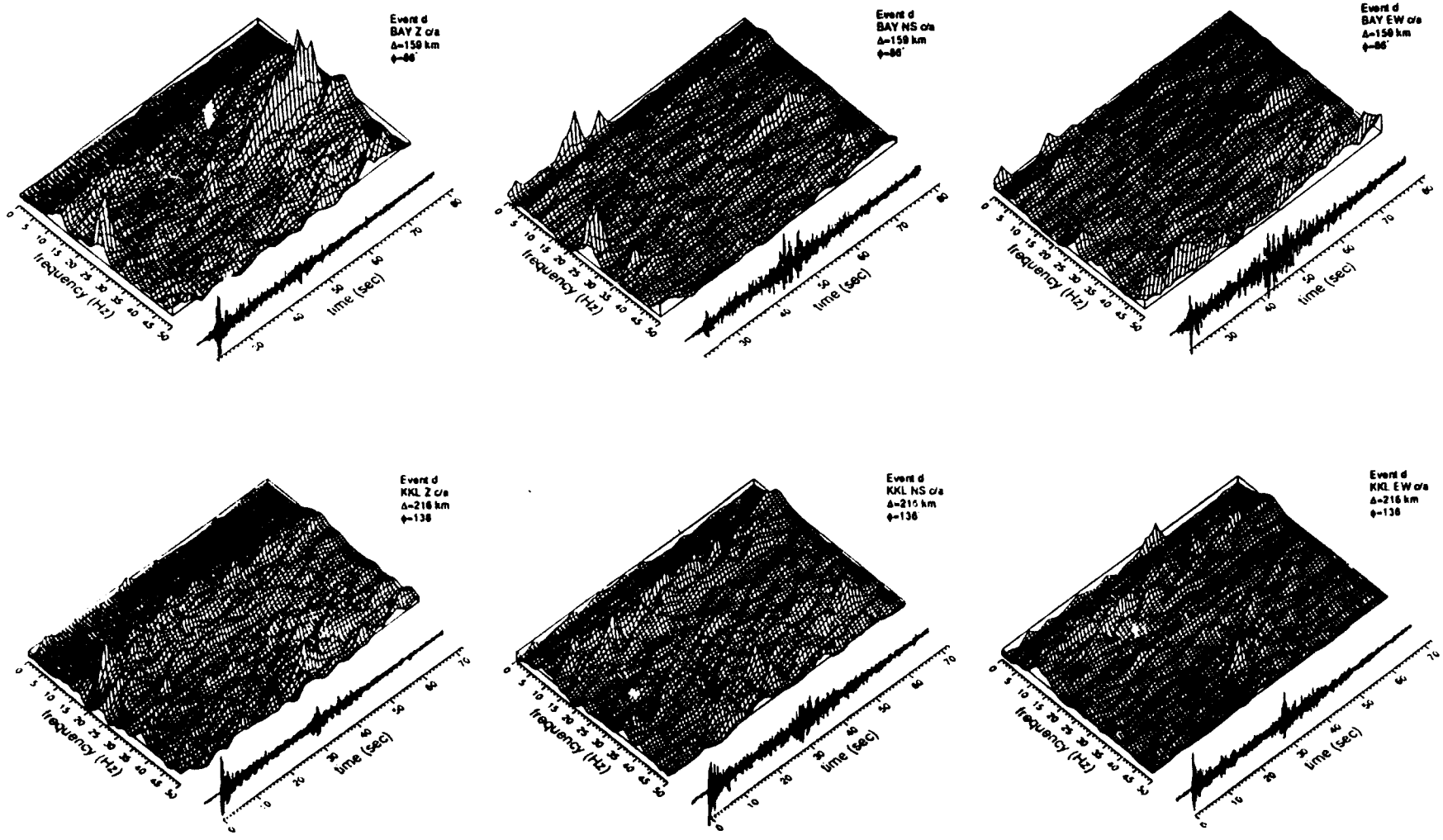
Event d
BAY Z c/a
Δ=158 km
Event d
BAY NS c/a
Δ=158 km
Event d
BAY EW c/a
Δ=158 km
Event d
KKL Z c/a
Δ=216 km
Event d
KKL NS c/a
Δ=215 km
Event d
KKL EW c/a
Δ=216 km
Frequency (Hz)
Time (sec)

Figure 7

New York State area

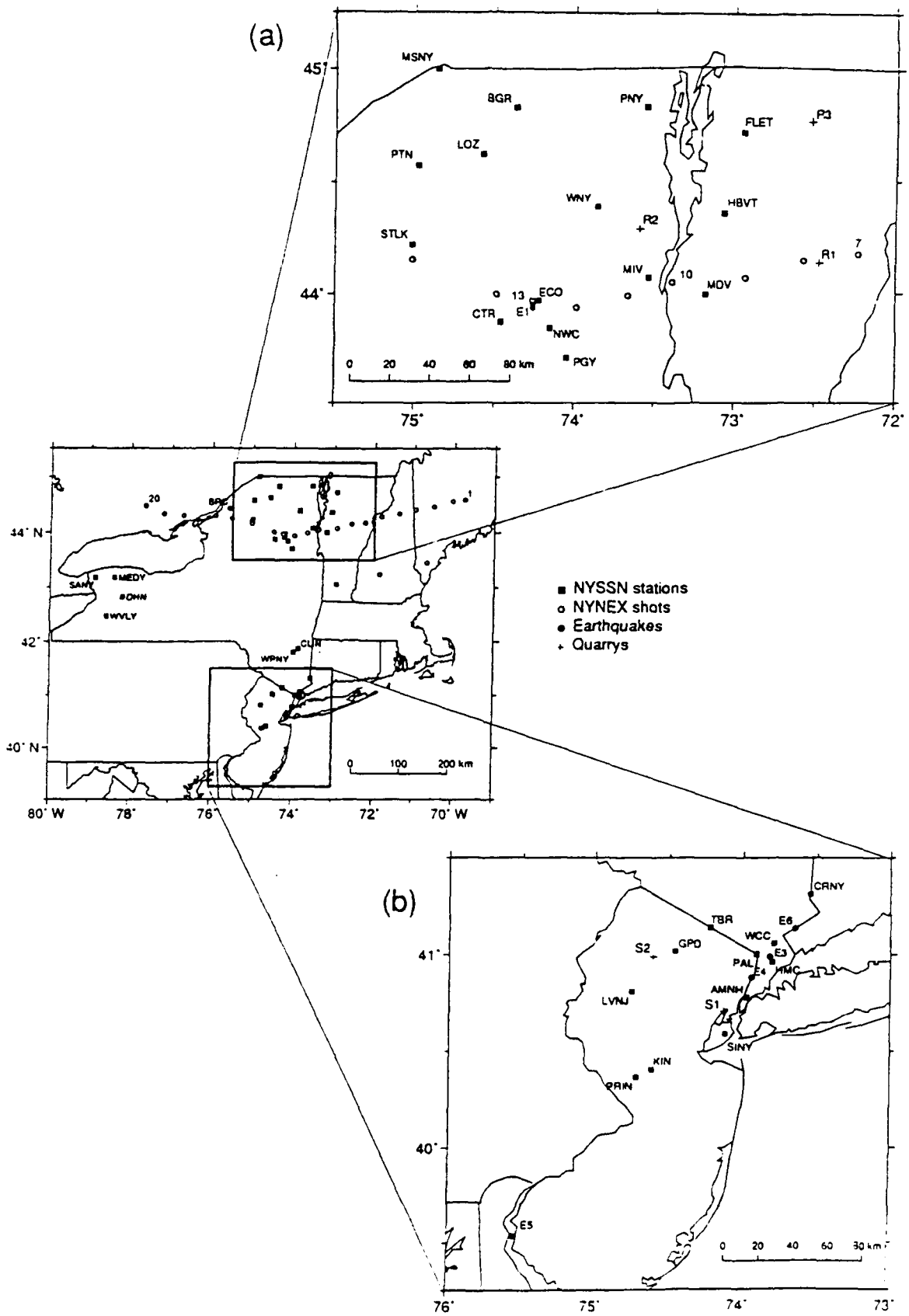

Figure 8

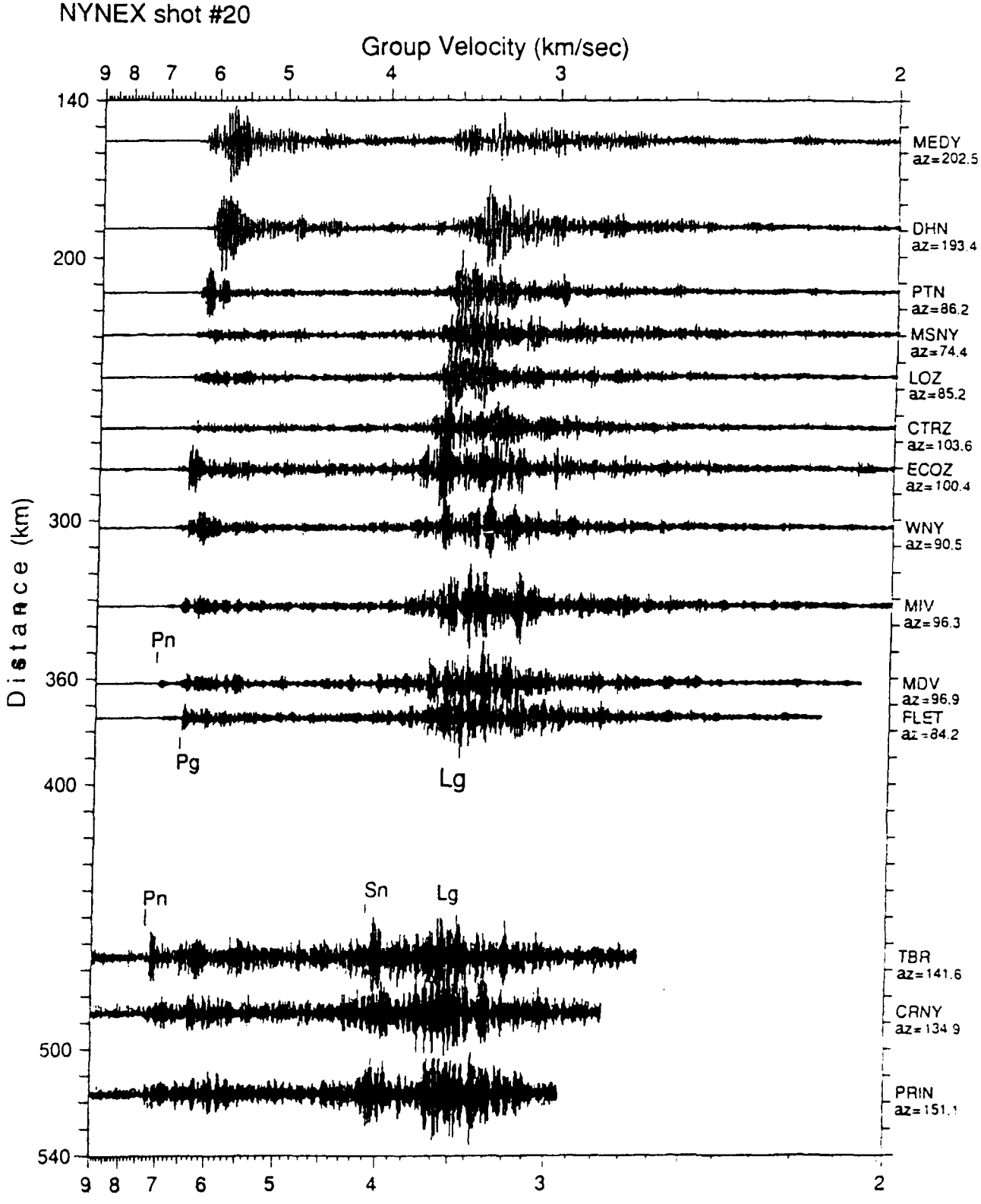
NYNEX shot #20
Group Velocity (km/sec)
9 8 7 6 5 4 3 2
Distance (km)
140
200
300
360
400
500
540
MEDY az=202.5
DHN az=193.4
PTN az=86.2
MSNY az=74.4
LOZ az=85.2
CTRZ az=103.6
ECOZ az=100.4
WNY az=90.5
MIV az=96.3
MDV az=96.9
FLET az=84.2
TBR az=141.6
CRNY az=134.9
PRIN az=151.1
Pn
Pg
Lg
Pn
Sn
Lg

Figure 9

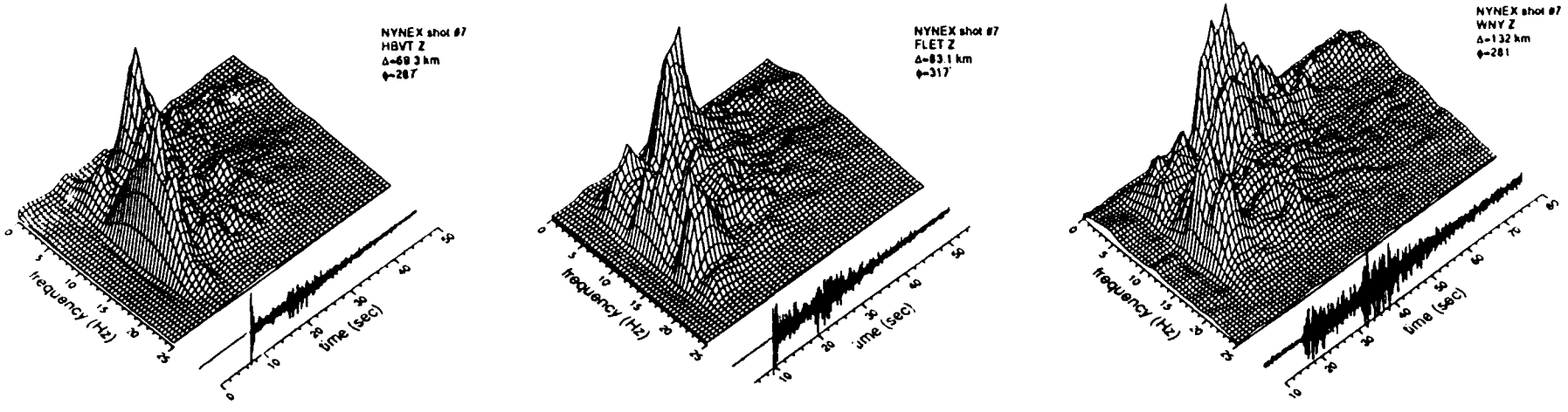
NYNEX shot #7
HBVT Z
Δ=69.3 km
ϕ=287
frequency (Hz)
time (sec)
NYNEX shot #7
FLET Z
Δ=83.1 km
ϕ=317
frequency (Hz)
time (sec)
NYNEX shot #7
WNY Z
Δ=132 km
ϕ=281
frequency (Hz)
time (sec)

Figure 10

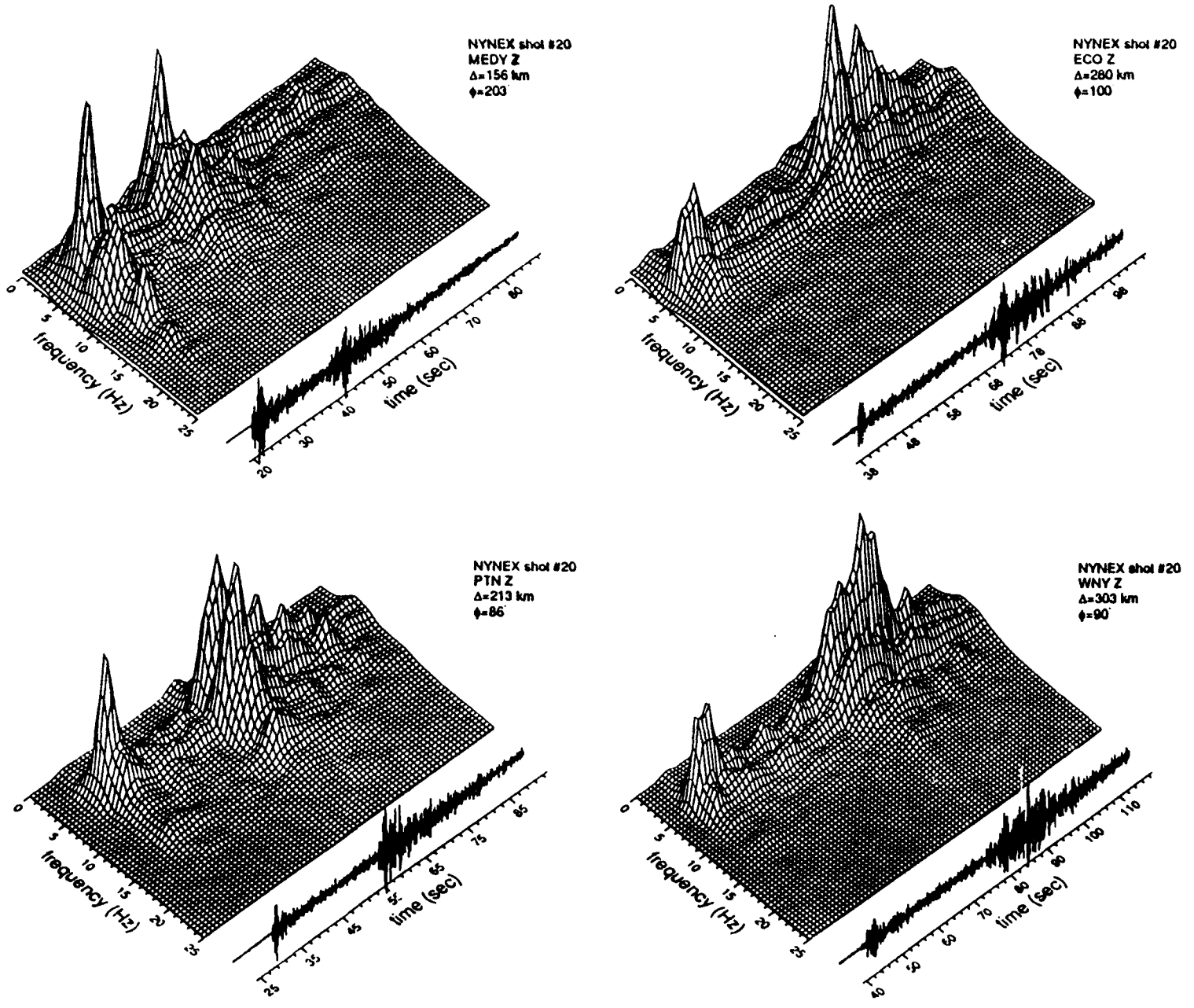
NYNEX shot #20
MEDY Z
Δ=156 km
ϕ=203
frequency (Hz)
time (sec)
NYNEX shot #20
ECO Z
Δ=280 km
ϕ=100
frequency (Hz)
time (sec)
NYNEX shot #20
PTN Z
Δ=213 km
ϕ=86
frequency (Hz)
time (sec)
NYNEX shot #20
WNY Z
Δ=303 km
ϕ=90
frequency (Hz)
time (sec)

Figure 11

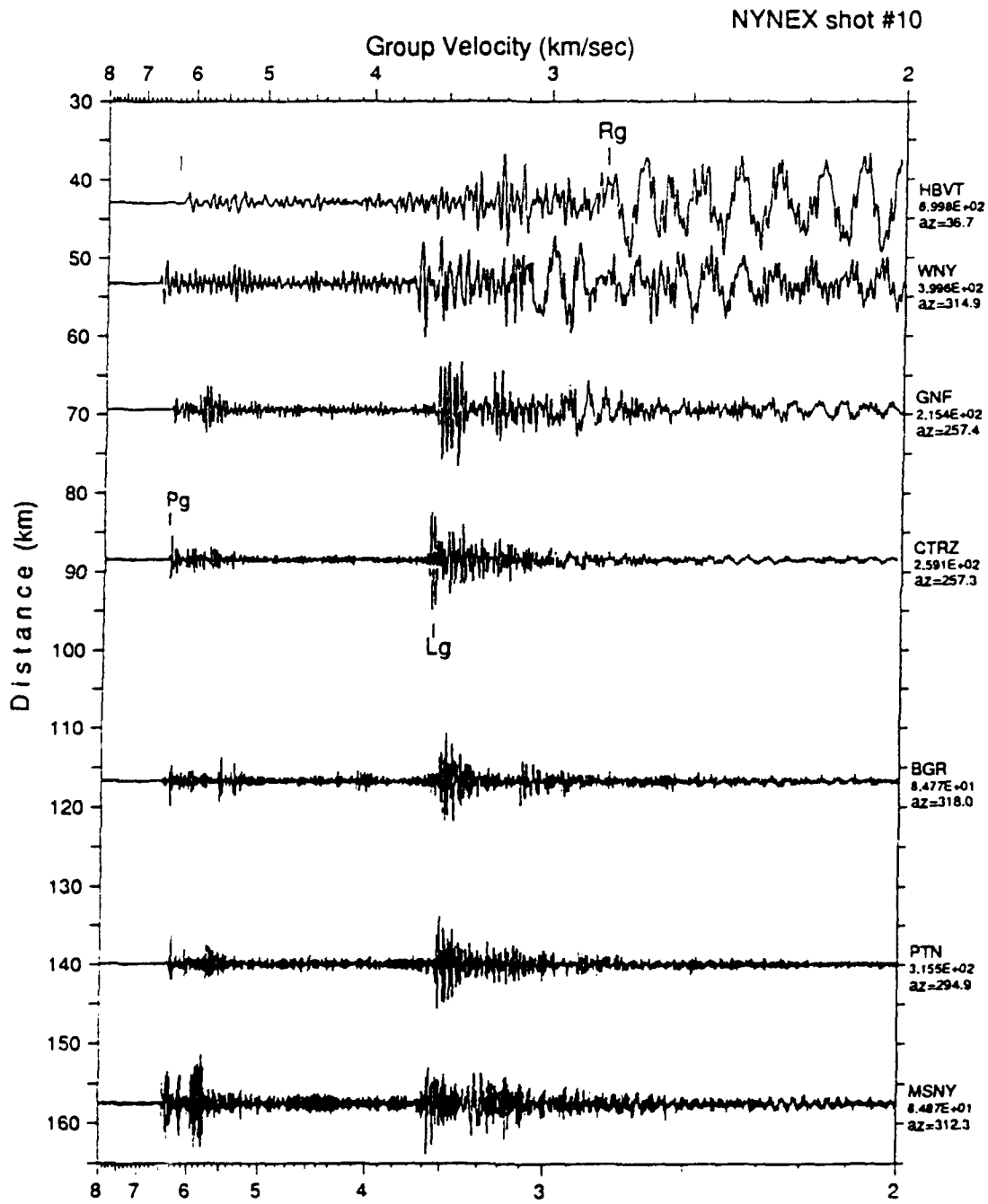
NYNEX shot #10
Group Velocity (km/sec)
8 7 6 5 4 3 2
Distance (km)
30 40 50 60 70 80 90 100 110 120 130 140 150 160
Rg
Pg
Lg
HBVT
6.998E+02
az=36.7
WNY
3.996E+02
az=314.9
GNF
2.154E+02
az=257.4
CTRZ
2.591E+02
az=257.3
BGR
8.477E+01
az=318.0
PTN
3.155E+02
az=294.9
MSNY
6.487E+01
az=312.3

Figure 12

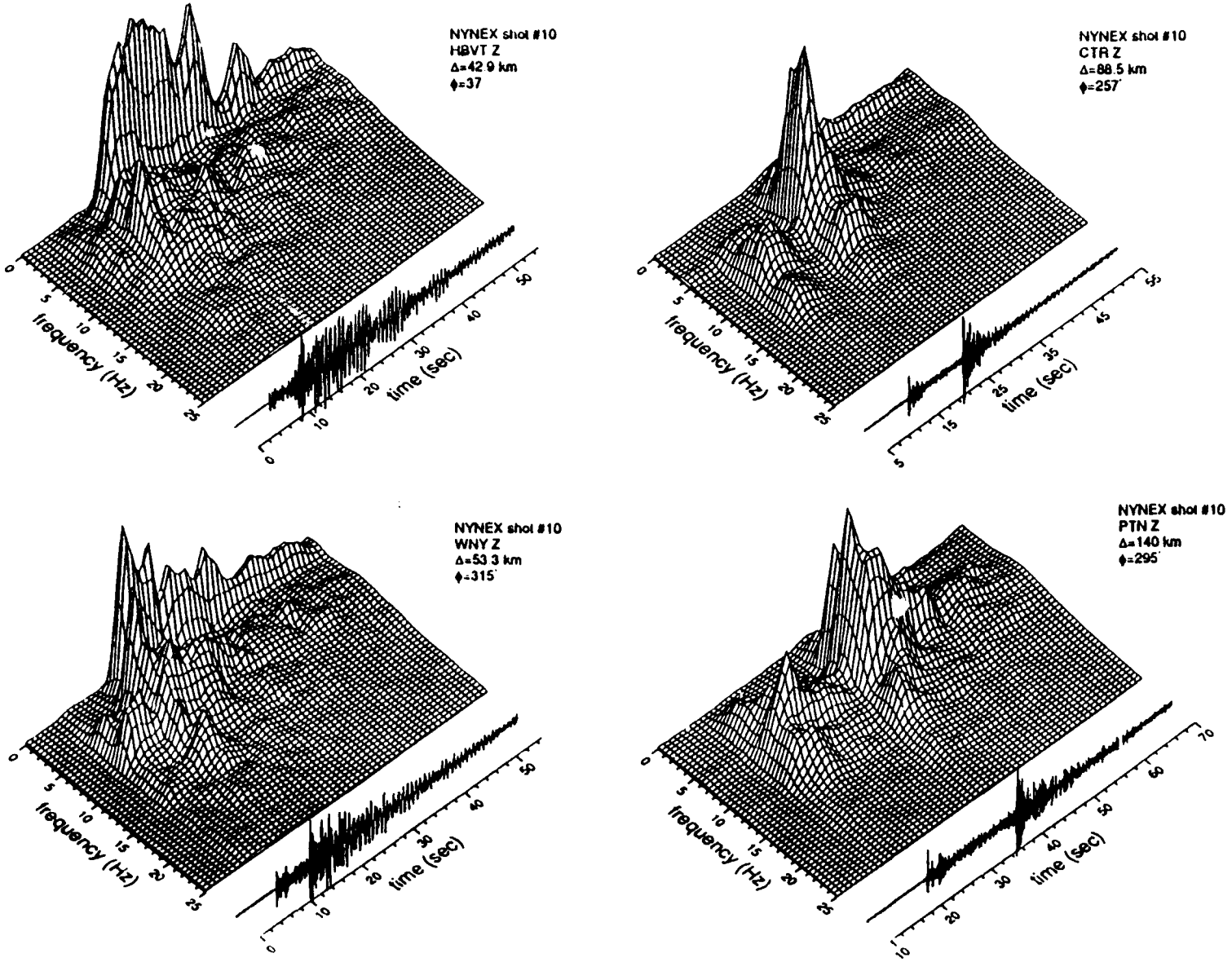
NYNEX shot #10
HBVT Z
Δ=42.9 km
♦=37
frequency (Hz)
time (sec)
NYNEX shot #10
CTR Z
Δ=88.5 km
♦=257°
frequency (Hz)
time (sec)
NYNEX shot #10
WNY Z
Δ=53.3 km
♦=315°
frequency (Hz)
time (sec)
NYNEX shot #10
PTN Z
Δ=140 km
♦=295°
frequency (Hz)
time (sec)

Figure 13

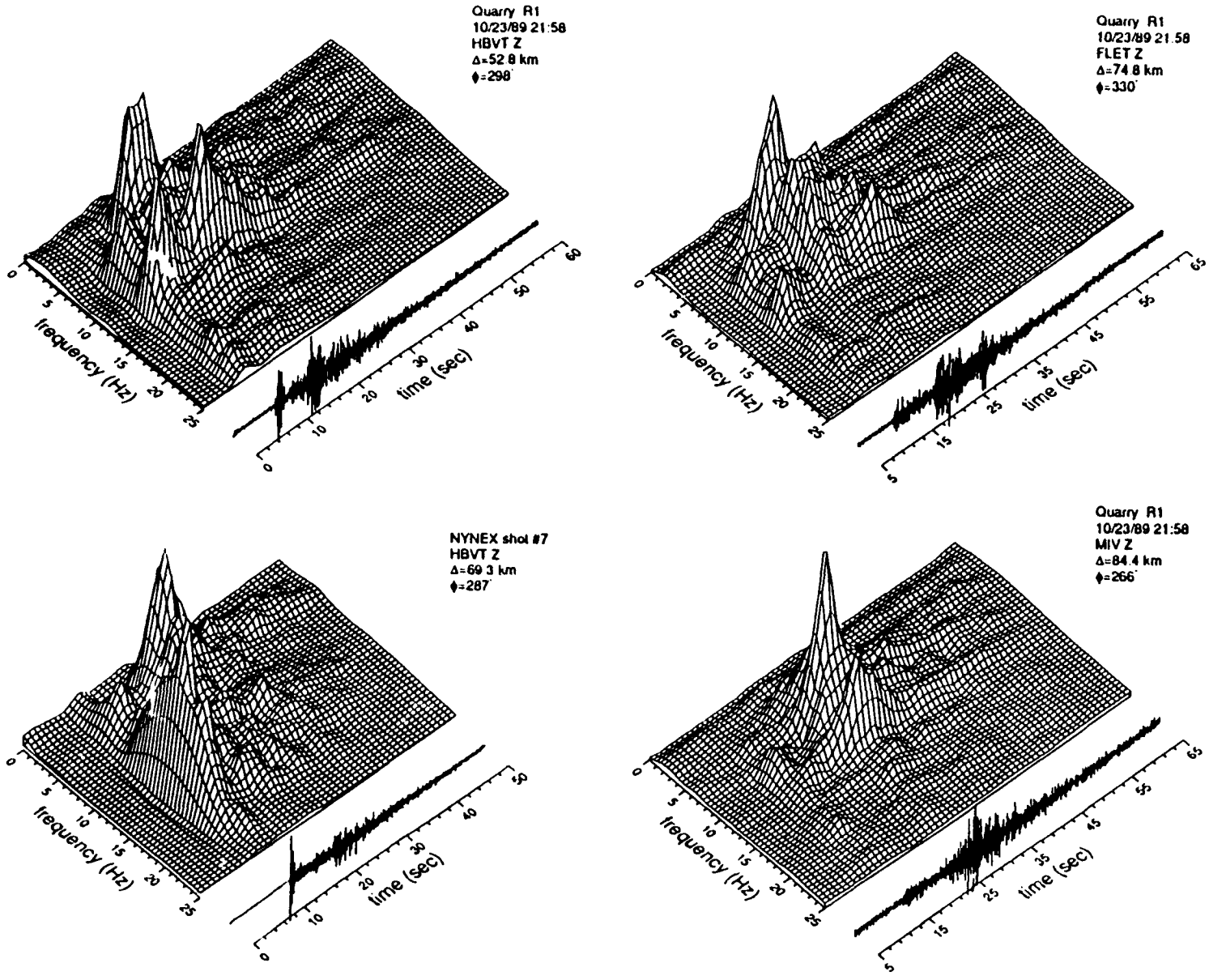
Quarry R1
10/23/89 21:58
HBVT Z
Δ=52.8 km
♦=298°
Quarry R1
10/23/89 21:58
FLET Z
Δ=74.8 km
♦=330°
NYNEX shot #7
HBVT Z
Δ=69.3 km
♦=287°
Quarry R1
10/23/89 21:58
MIV Z
Δ=84.4 km
♦=266°
frequency (Hz)
time (sec)

Figure 14

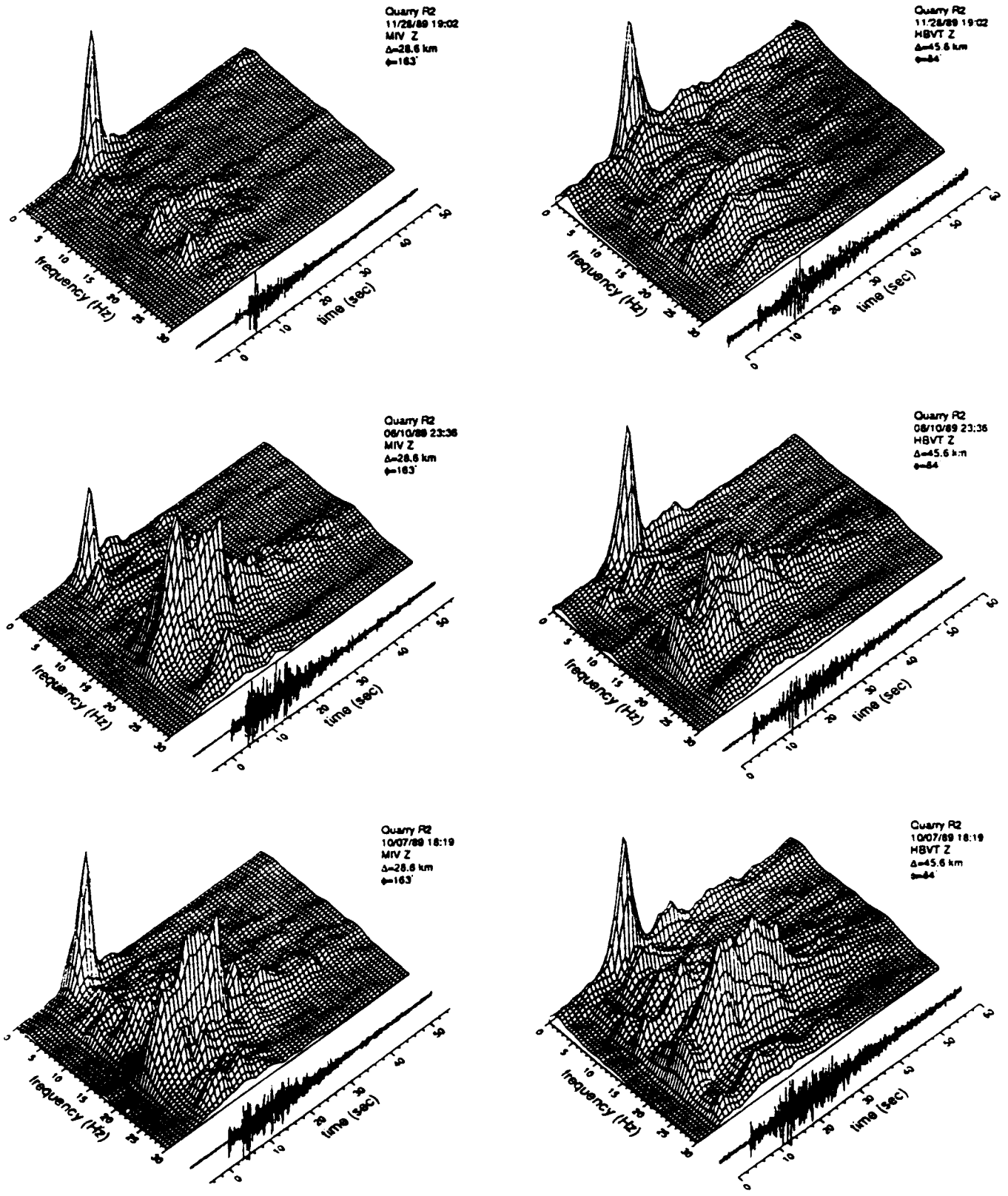
Quarry R2
11/28/89 19:02
MIV Z
Δ=28.6 km
Φ=163°
Quarry R2
11/28/89 19:02
HBVT Z
Δ=45.6 km
Φ=84°
Quarry R2
08/10/89 23:36
MIV Z
Δ=28.6 km
Φ=163°
Quarry R2
08/10/89 23:36
HBVT Z
Δ=45.6 km
Φ=84°
Quarry R2
10/07/89 18:19
MIV Z
Δ=28.6 km
Φ=163°
Quarry R2
10/07/89 18:19
HBVT Z
Δ=45.6 km
Φ=84°
frequency (Hz)
time (sec)

Figure 15

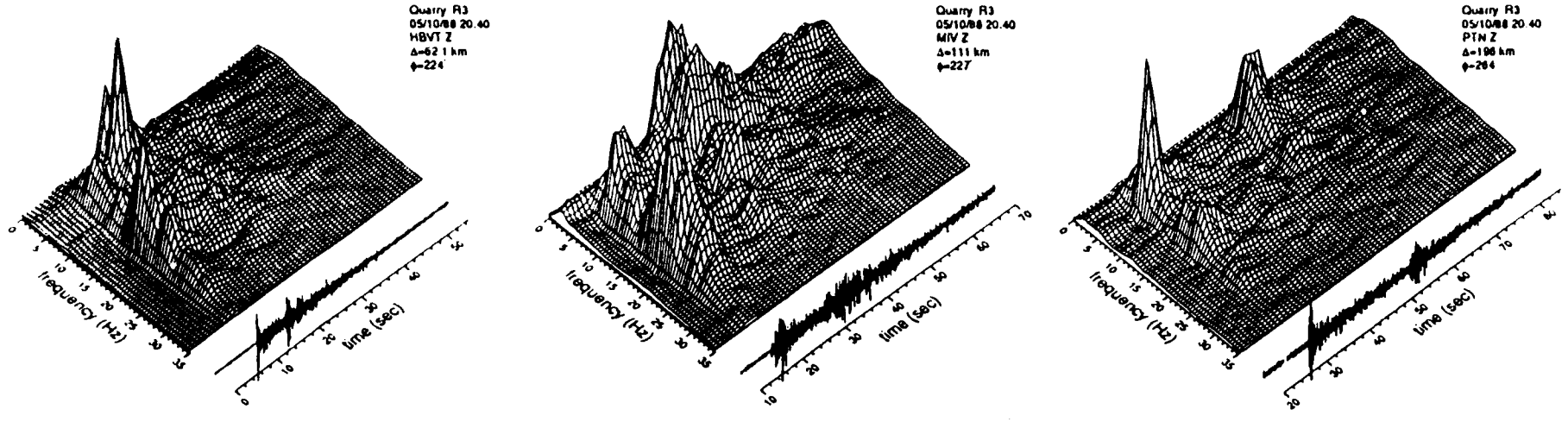
Quarry R3
05/10/88 20.40
HBVT Z
Δ=62.1 km
ϕ=224
Quarry R3
05/10/88 20.40
MIV Z
Δ=111 km
ϕ=227
Quarry R3
05/10/88 20.40
PTN Z
Δ=196 km
ϕ=264
frequency (Hz)
time (sec)

Figure 16

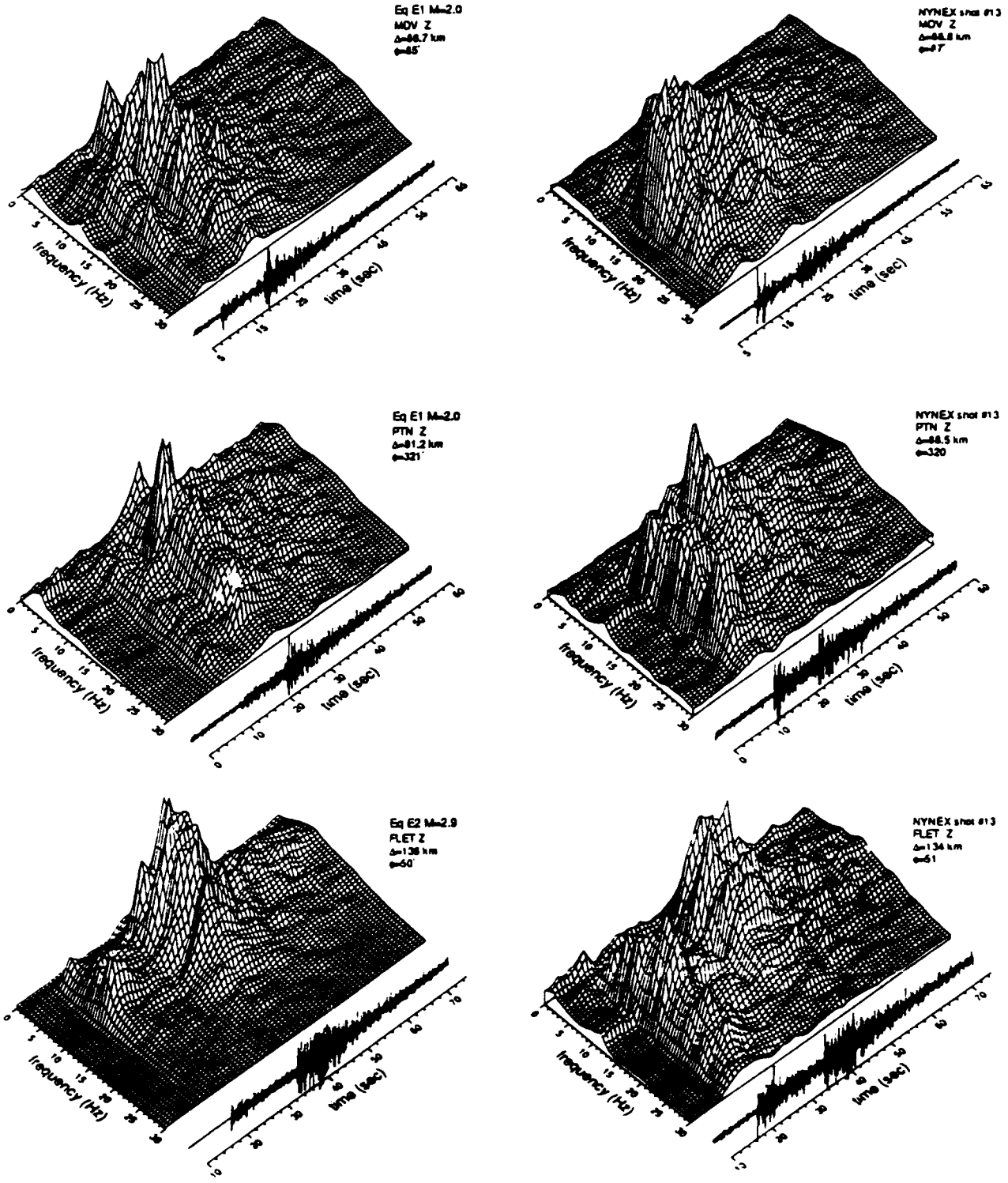
Eq E1 M=2.0
MDV Z
Δ=66.7 km
φ=65°
NYNEX shot #13
MDV Z
Δ=66.8 km
φ=67°
Eq E1 M=2.0
PTN Z
Δ=81.2 km
φ=321°
NYNEX shot #13
PTN Z
Δ=66.5 km
φ=320°
Eq E2 M=2.9
PLET Z
Δ=136 km
φ=60°
NYNEX shot #13
PLET Z
Δ=134 km
φ=61°
frequency (Hz)
time (sec)

Figure 17

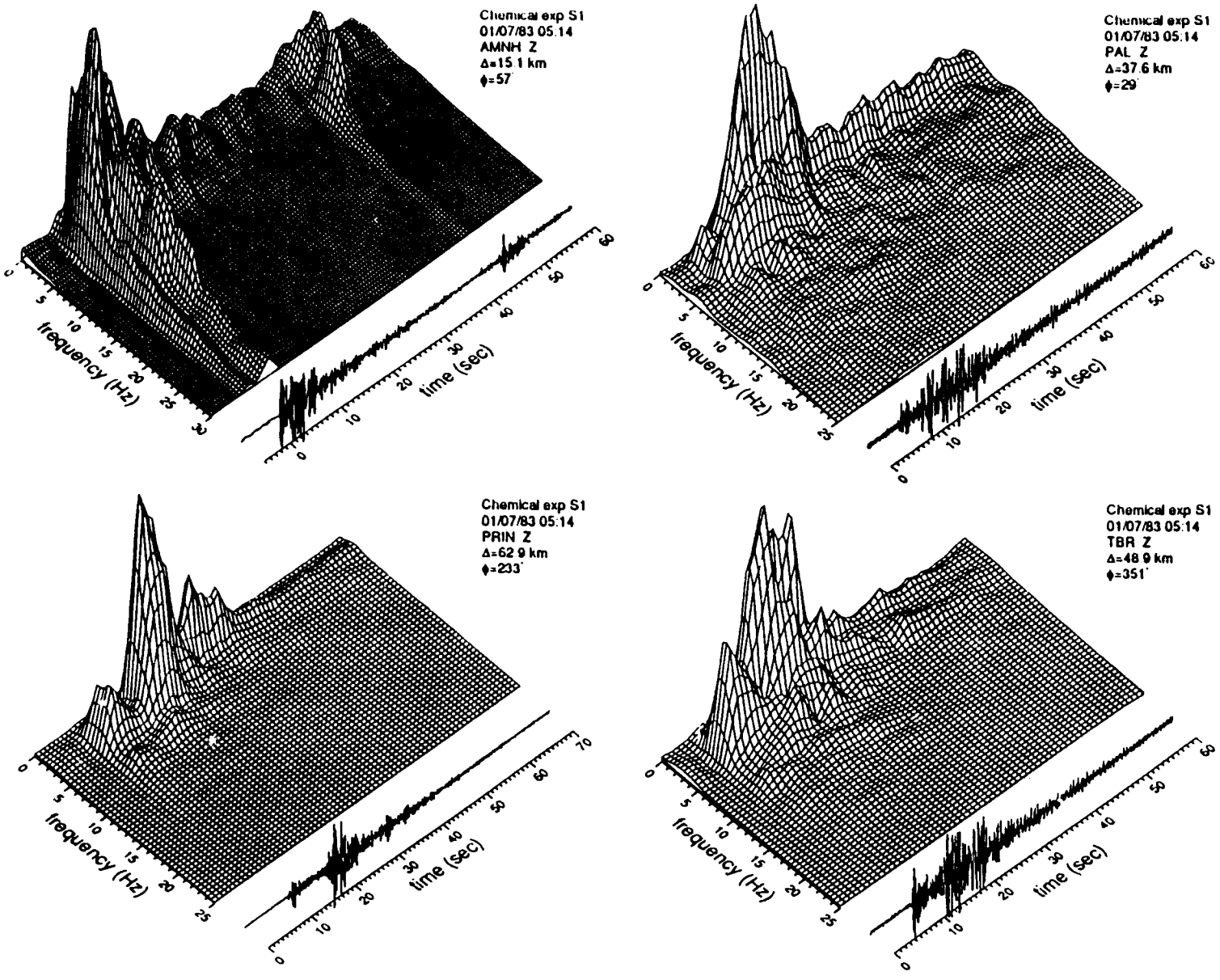
Chemical exp S1
01/07/83 05:14
AMNH Z
Δ=15.1 km
ϕ=57°
frequency (Hz)
time (sec)
Chemical exp S1
01/07/83 05:14
PAL Z
Δ=37.6 km
ϕ=29°
frequency (Hz)
time (sec)
Chemical exp S1
01/07/83 05:14
PRIN Z
Δ=62.9 km
ϕ=233°
frequency (Hz)
time (sec)
Chemical exp S1
01/07/83 05:14
TBR Z
Δ=48.9 km
ϕ=351°
frequency (Hz)
time (sec)

Figure 18

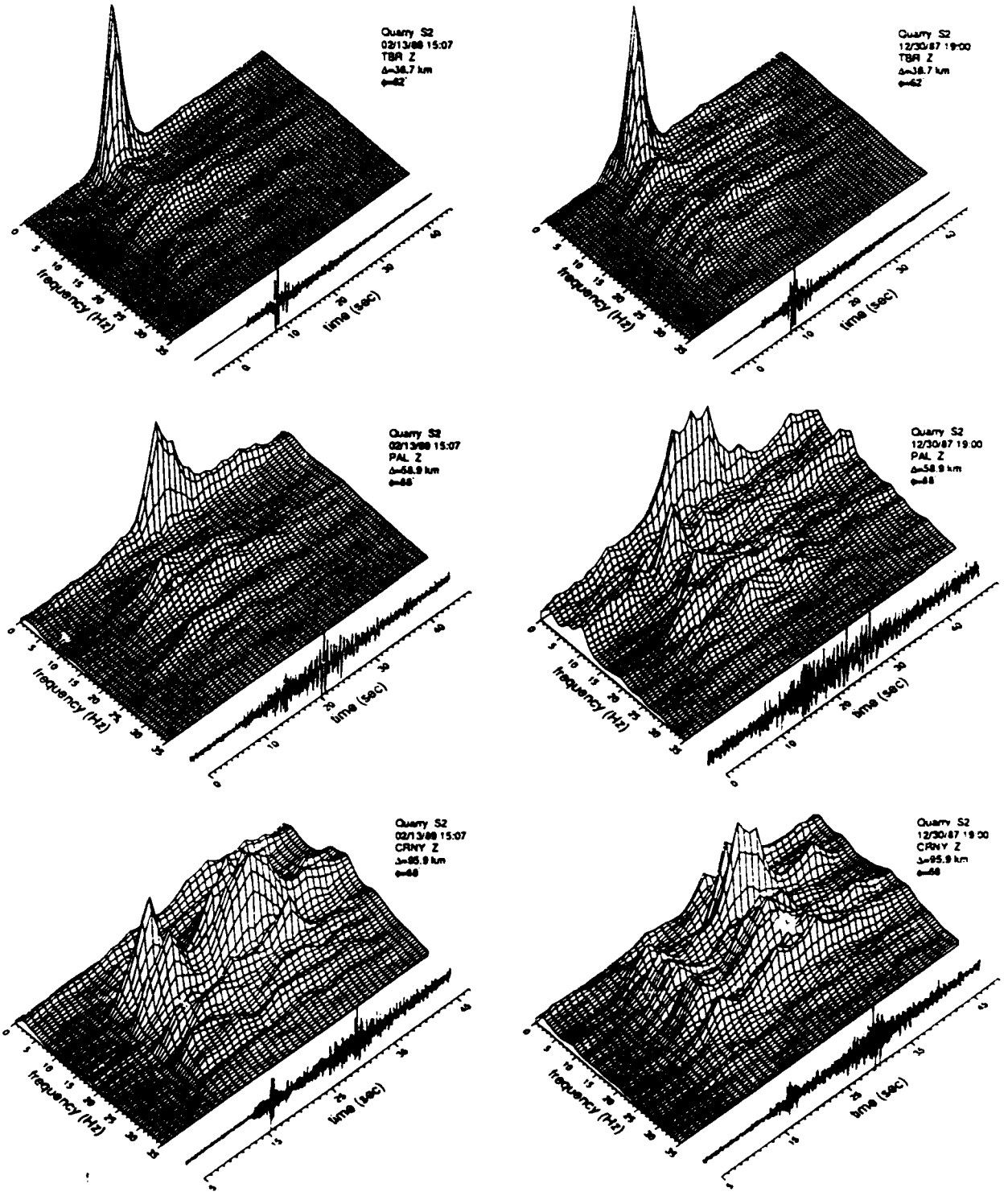
Quarry S2
02/13/88 15:07
TBR Z
Δ=38.7 km
Φ=62°
frequency (Hz)
time (sec)
Quarry S2
12/30/87 19:00
TBR Z
Δ=38.7 km
Φ=62°
frequency (Hz)
time (sec)
Quarry S2
02/13/88 15:07
PAL Z
Δ=58.9 km
Φ=68°
frequency (Hz)
time (sec)
Quarry S2
12/30/87 19:00
PAL Z
Δ=58.9 km
Φ=68°
frequency (Hz)
time (sec)
Quarry S2
02/13/88 15:07
CRNY Z
Δ=85.9 km
Φ=68°
frequency (Hz)
time (sec)
Quarry S2
12/30/87 19:00
CRNY Z
Δ=85.9 km
Φ=68°
frequency (Hz)
time (sec)

Figure 19

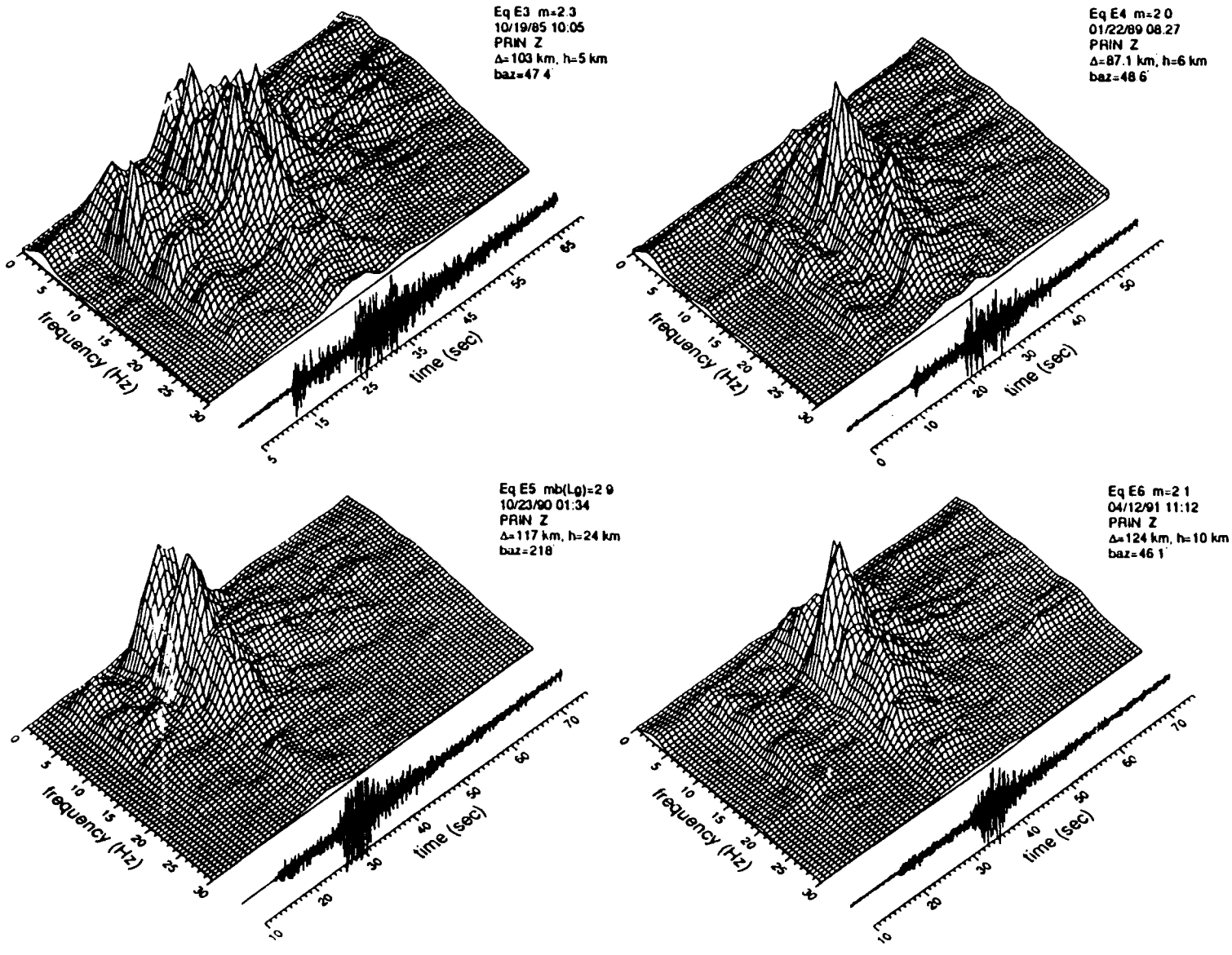
Eq E3 m=2.3
10/19/85 10:05
PRIN Z
Δ=103 km, h=5 km
baz=47.4
frequency (Hz)
time (sec)
Eq E4 m=2.0
01/22/89 08:27
PRIN Z
Δ=87.1 km, h=6 km
baz=48.6
frequency (Hz)
time (sec)
Eq E5 mb(Lg)=2.9
10/23/90 01:34
PRIN Z
Δ=117 km, h=24 km
baz=218
frequency (Hz)
time (sec)
Eq E6 m=2.1
04/12/91 11:12
PRIN Z
Δ=124 km, h=10 km
baz=46.1
frequency (Hz)
time (sec)

Figure 20

NORESS, Norway

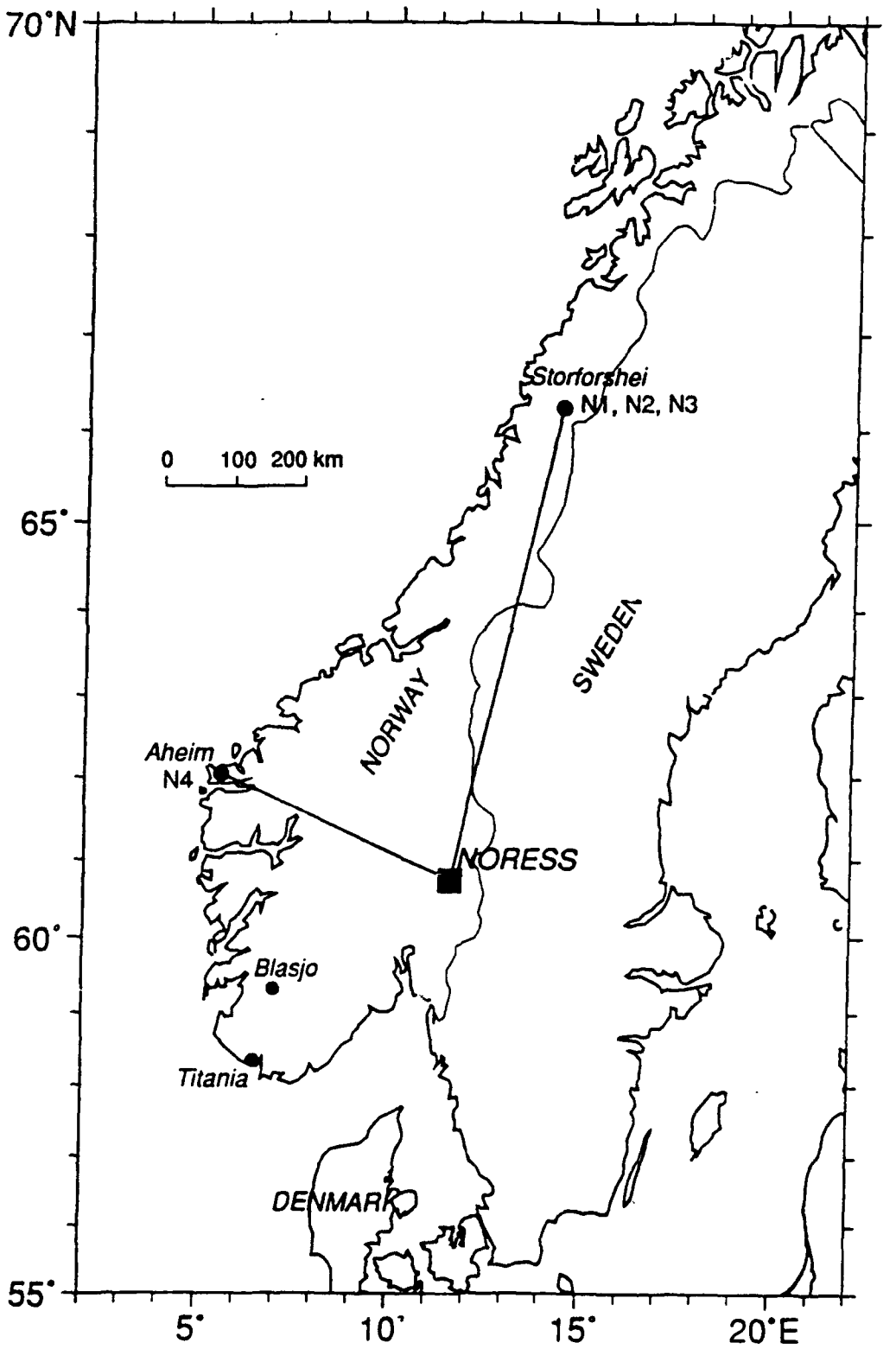

Figure 21

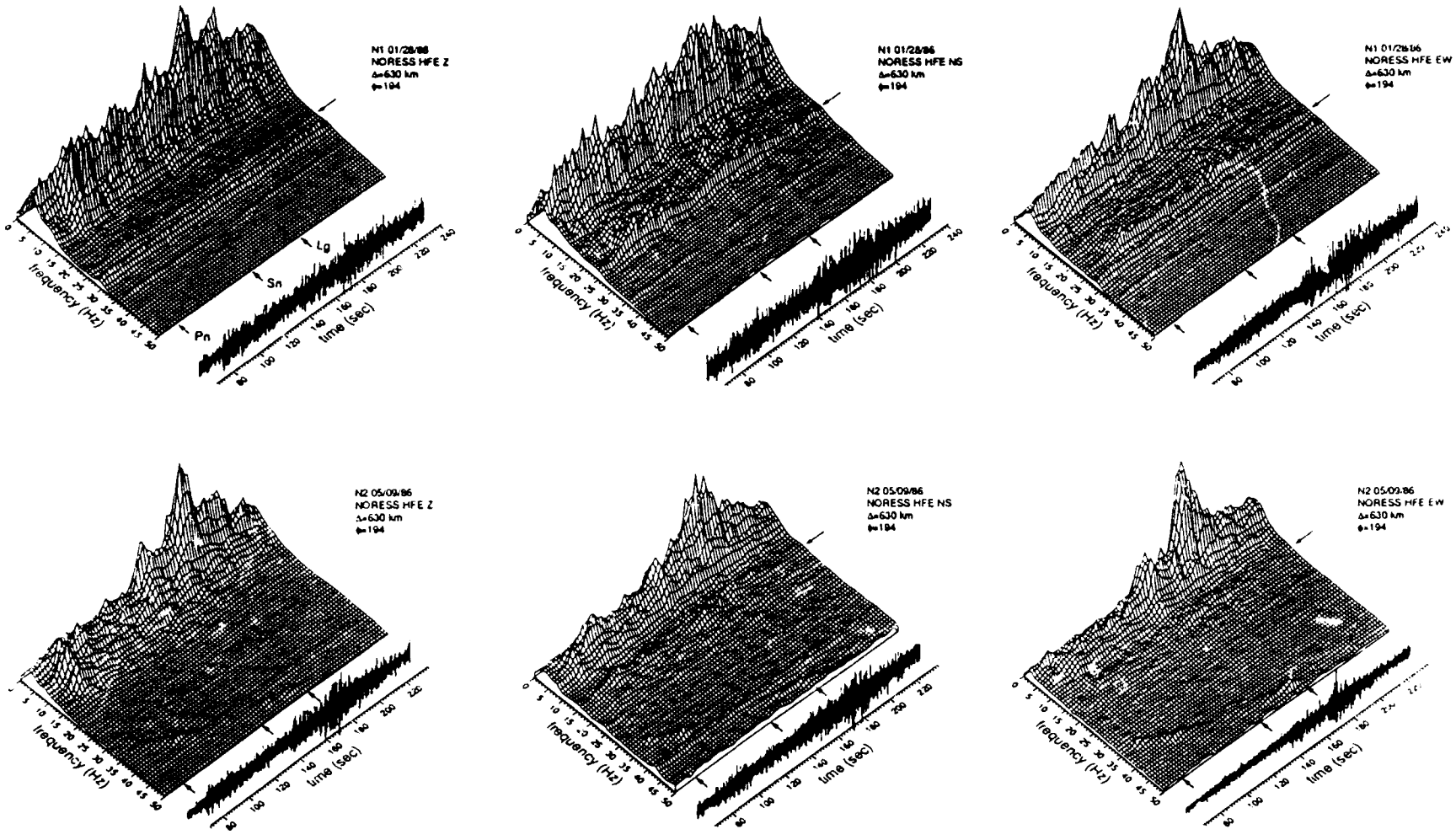
N1 01/28/86
NORESS HFE Z
Δ=630 km
Φ=194
Pn
Sn
Lg
Frequency (Hz)
Time (sec)
N1 01/28/86
NORESS HFE NS
Δ=630 km
Φ=194
Frequency (Hz)
Time (sec)
N1 01/28/86
NORESS HFE EW
Δ=630 km
Φ=194
Frequency (Hz)
Time (sec)
N2 05/09/86
NORESS HFE Z
Δ=630 km
Φ=194
Frequency (Hz)
Time (sec)
N2 05/09/86
NORESS HFE NS
Δ=630 km
Φ=194
Frequency (Hz)
Time (sec)
N2 05/09/86
NORESS HFE EW
Δ=630 km
Φ=194
Frequency (Hz)
Time (sec)

Figure 22

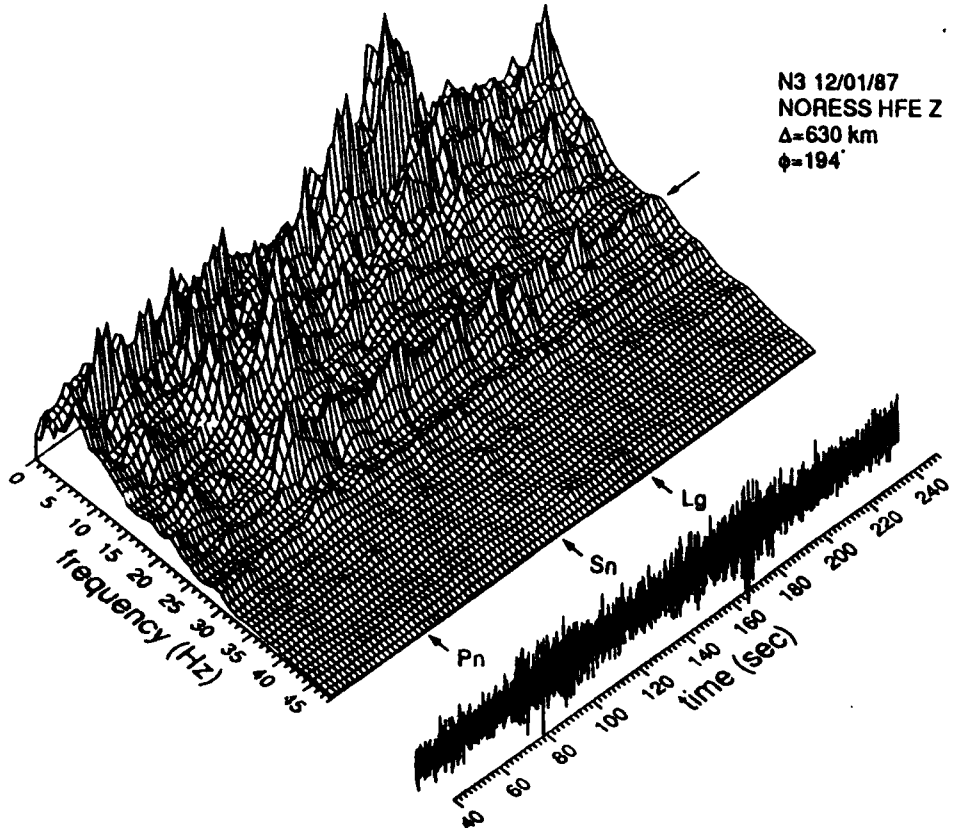
N3 12/01/87
NORESS HFE Z
Δ=630 km
ϕ=194°
Pn
Sn
Lg
frequency (Hz)
0
5
10
15
20
25
30
35
40
45
time (sec)
40
60
80
100
120
140
160
180
200
220
240

Figure 23

N4 05/24/89

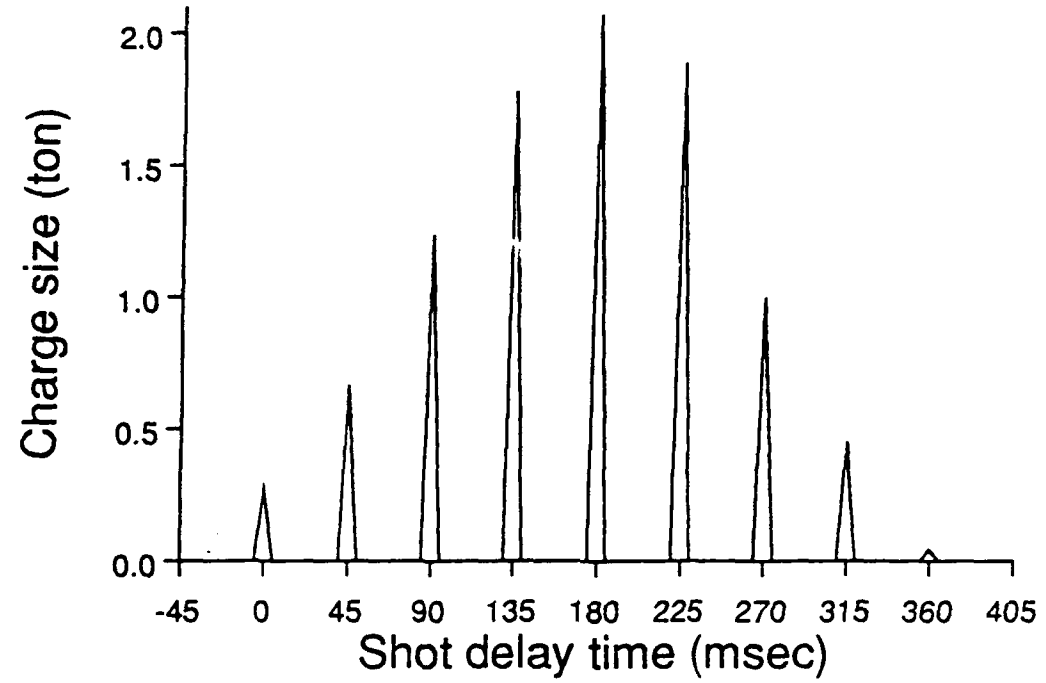

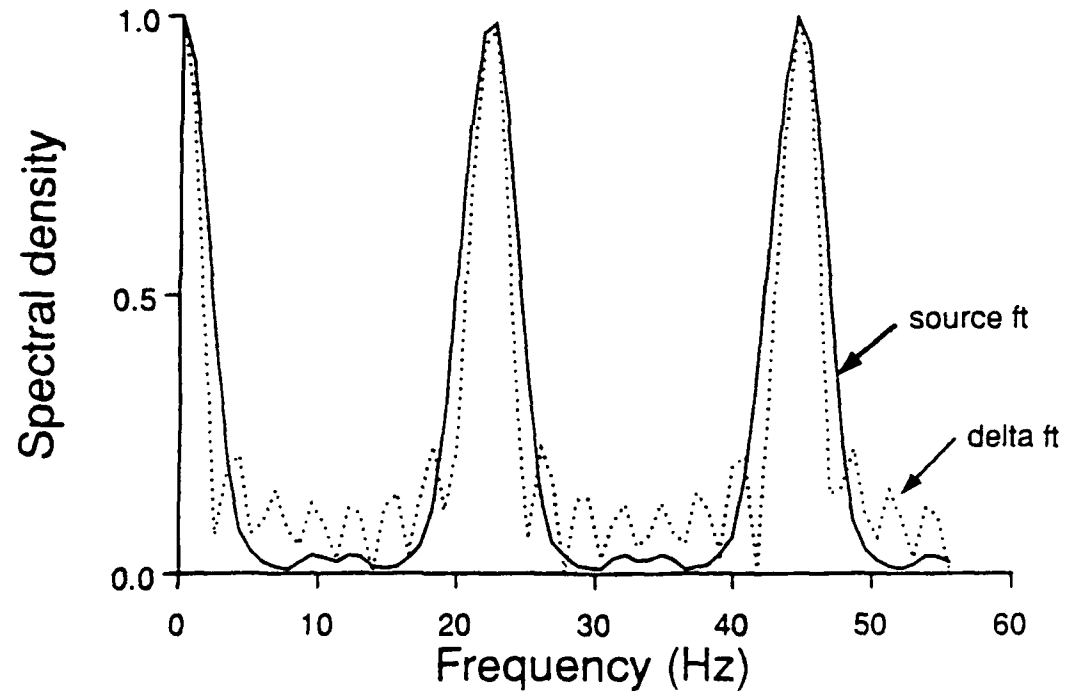

Figure 24

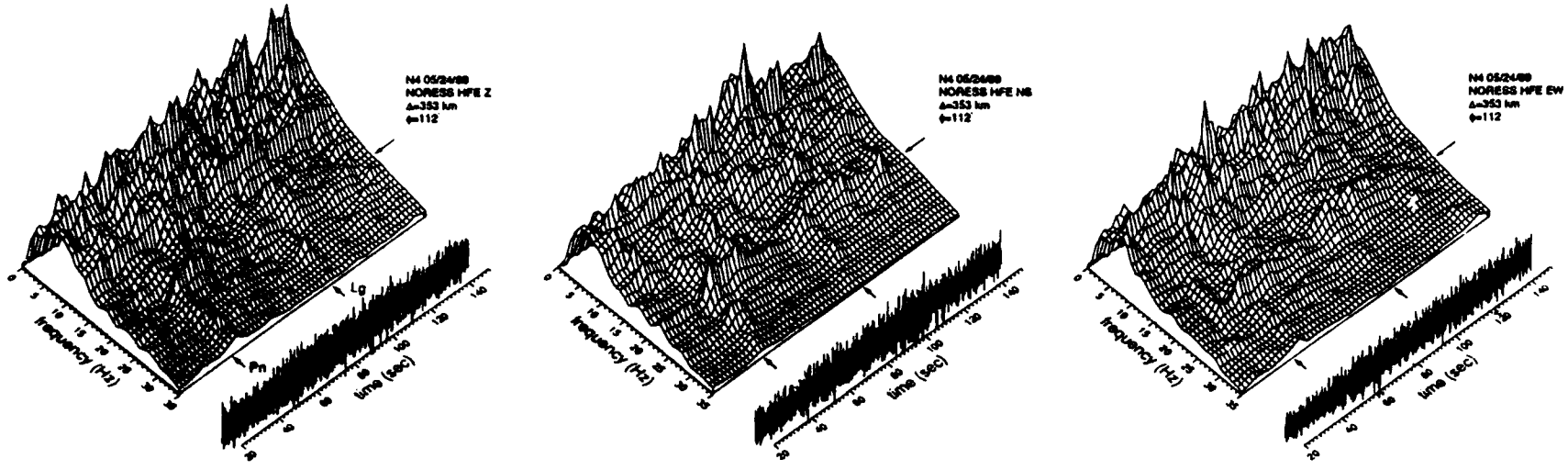
N4 05/24/89
NORESS HFE Z
Δ=353 km
Φ=112
Pn
Lg
frequency (Hz)
time (sec)
N4 05/24/89
NORESS HFE NS
Δ=353 km
Φ=112
frequency (Hz)
time (sec)
N4 05/24/89
NORESS HFE EW
Δ=353 km
Φ=112
frequency (Hz)
time (sec)

Figure 25

Prof. Thomas Ahrens
Seismological Lab, 252-21
Division of Geological & Planetary Sciences
California Institute of Technology
Pasadena, CA 91125

Prof. Keiiti Aki
Center for Earth Sciences
University of Southern California
University Park
Los Angeles, CA 90089-0741

Prof. Shelton Alexander
Geosciences Department
403 Deike Building
The Pennsylvania State University
University Park, PA 16802

Dr. Ralph Alewine, III
DARPA/NMRO
3701 North Fairfax Drive
Arlington, VA 22203-1714

Prof. Charles B. Archambeau
CIRES
University of Colorado
Boulder, CO 80309

Dr. Thomas C. Bache, Jr.
Science Applications Int'l Corp.
10260 Campus Point Drive
San Diego, CA 92121 (2 copies)

Prof. Muawia Barazangi
Institute for the Study of the Continent
Cornell University
Ithaca, NY 14853

Dr. Jeff Barker
Department of Geological Sciences
State University of New York
at Binghamton
Vestal, NY 13901

Dr. Douglas R. Baumgardt
ENSCO, Inc
5400 Port Royal Road
Springfield, VA 22151-2388

Dr. Susan Beck
Department of Geosciences
Building #77
University of Arizona
Tuscon, AZ 85721

Dr. T.J. Bennett
S-CUBED
A Division of Maxwell Laboratories
11800 Sunrise Valley Drive, Suite 1450
Reston, VA 22091

Dr. Robert Blandford
AFTAC/TT, Center for Seismic Studies
1330 North 17th Street
Suite 1450
Arlington, VA 22209-2308

Dr. G.A. Bollinger
Department of Geological Sciences
Virginia Polytechnical Institute
21044 Derring Hall
Blacksburg, VA 24061

Dr. Stephen Bratt
Center for Seismic Studies
1300 North 17th Street
Suite 1450
Arlington, VA 22209-2308

Dr. Lawrence Burdick
Woodward-Clyde Consultants
566 El Dorado Street
Pasadena, CA 91109-3245

Dr. Robert Burridge
Schlumberger-Doll Research Center
Old Quarry Road
Ridgefield, CT 06877

Dr. Jerry Carter
Center for Seismic Studies
1300 North 17th Street
Suite 1450
Arlington, VA 22209-2308

Dr. Eric Chael
Division 9241
Sandia Laboratory
Albuquerque, NM 87185

Prof. Vernon F. Cormier
Department of Geology & Geophysics
U-45, Room 207
University of Connecticut
Storrs, CT 06268

Prof. Anton Dainty
Earth Resources Laboratory
Massachusetts Institute of Technology
42 Carleton Street
Cambridge, MA 02142

Prof. Steven Day
Department of Geological Sciences
San Diego State University
San Diego, CA 92182

Marvin Denny
U.S. Department of Energy
Office of Arms Control
Washington, DC 20585

Dr. Zoltan Der
ENSCO, Inc.
5400 Port Royal Road
Springfield, VA 22151-2388

Prof. Adam Dziewonski
Hoffman Laboratory, Harvard University
Dept. of Earth Atmos. & Planetary Sciences
20 Oxford Street
Cambridge, MA 02138

Prof. John Ebel
Department of Geology & Geophysics
Boston College
Chestnut Hill, MA 02167

Eric Fielding
SNEE Hall
INSTOC
Cornell University
Ithaca, NY 14853

Dr. Mark D. Fisk
Mission Research Corporation
735 State Street
P.O. Drawer 719
Santa Barbara, CA 93102

Prof Stanley Flatte
Applied Sciences Building
University of California, Santa Cruz
Santa Cruz, CA95064

Dr. John Foley
NER-Geo Sciences
1100 Crown Colony Drive
Quincy, MA 02169

Prof. Donald Forsyth
Department of Geological Sciences
Brown University
Providence, RI 02912

Dr. Art Frankel
U.S. Geological Survey
922 National Center
Reston, VA 22092

Dr. Cliff Frolich
Institute of Geophysics
8701 North Mopac
Austin, TX 78759

Dr. Holly Given
IGPP, A-025
Scripps Institute of Oceanography
University of California, San Diego
La Jolla, CA 92093

Dr. Jeffrey W. Given
SAIC
10260 Campus Point Drive
San Diego, CA 92121

Dr. Dale Glover
Defense Intelligence Agency
ATTN: ODT-1B
Washington, DC 20301

Dr. Indra Gupta
Teledyne Geotech
314 Montgomery Street
Alexanderia, VA 22314

Dan N. Hagedon
Pacific Northwest Laboratories
Battelle Boulevard
Richland, WA 99352

Dr. James Hannon
Lawrence Livermore National Laboratory
P.O. Box 808
L-205
Livermore, CA 94550

Dr. Roger Hansen
HQ AFTAC/TTR
Patrick AFB, FL 32925-6001

Prof. David G. Harkrider
Seismological Laboratory
Division of Geological & Planetary Sciences
California Institute of Technology
Pasadena, CA 91125

Prof. Danny Harvey
CIRES
University of Colorado
Boulder, CO 80309

Prof. Donald V. Helmberger
Seismological Laboratory
Division of Geological & Planetary Sciences
California Institute of Technology
Pasadena, CA 91125

Prof. Eugene Herrin
Institute for the Study of Earth and Man
Geophysical Laboratory
Southern Methodist University
Dallas, TX 75275

Prof. Robert B. Herrmann
Department of Earth & Atmospheric Sciences
St. Louis University
St. Louis, MO 63156

Prof. Lane R. Johnson
Seismographic Station
University of California
Berkeley, CA 94720

Prof. Thomas H. Jordan
Department of Earth, Atmospheric &
Planetary Sciences
Massachusetts Institute of Technology
Cambridge, MA 02139

Prof. Alan Kafka
Department of Geology & Geophysics
Boston College
Chestnut Hill, MA 02167

Robert C. Kemerait
ENSCO, Inc.
445 Pineda Court
Melbourne , FL 32940

Dr. Max Koontz
U.S. Dept. of Energy/DP 5
Forrestal Building
1000 Independence Avenue
Washington, DC 20585

Dr. Richard LaCoss
MIT Lincoln Laboratory, M-200B
P.O. Box 73
Lexington, MA 02173-0073

Dr. Fred K. Lamb
University of Illinois at Urbana-Champaign
Department of Physics
1110 West Green Street
Urbana, IL 61801

Prof. Charles A. Langston
Geosciences Department
403 Deike Building
The Pennsylvania State University
University Park, PA 16802

Jim Lawson, Chief Geophysicist
Oklahoma Geological Survey
Oklahoma Geophysical Obseervatory
P.O. Box 8
Leonard, OK 74043-0008

Prof. Thorne Lay
Institute of Tectonics
Earth Science Board
University of California, Santa Cruz
Santa Cruz, CA 95064

Dr. William Leith
U.S. Geological Survey
Mail Stop 928
Reston, VA 22092

Mr. James F. Lewkowicz
Phillips Laboratory/GPEH
Hanscom AFB, MA 01731-5000(2 copies)

Mr. Alfred Lieberman
ACDA/VI-OA State Department Building
Room 5726
320-21st Street, NW
Washington, DC 20451

Prof. L. Timothy Long
School of Geophysical Sciences
Georgia Institute of Technology
Atlanta, GA 30332

Dr. Robert Masse
Denver Federal Building
Bos 25046, Mail Stop 967
Denver, CO 80225

Dr. Randolph Martin, III
New England Research, Inc.
76 Olcott Drive
White River Junction, VT 05001

Dr. Gary McCartor
Department of Physics
Southern Methodist University
Dallas, TX 75275

Prof. Thomas V. McEvilly
Seismographic Station
University of California
Berkeley, CA 94720

Dr. Art McGarr
U.S. Geological Survey
Mail Stop 977
U.S. Geological Survey
Menlo Park, CA 94025

Dr. Keith L. McLaughlin
S-CUBED
A Division of Maxwell Laboratory
P.O. Box 1620
La Jolla, CA 92038-1620

Stephen Miller & Dr. Alexander Florence
SRI International
333 Ravenswood Avenue
Box AF 116
Menlo Park, CA 94025-3493

Prof. Bernard Minster
IGPP, A-025
Scripps Institute of Oceanography
University of California, San Diego
La Jolla, CA 92093

Prof. Brian J. Mitchell
Department of Earth & Atmospheric Sciences
St. Louis University
St. Louis, MO 63156

Mr. Jack Murphy
S-CUBED
A Division of Maxwell Laboratory
11800 Sunrise Valley Drive, Suite 1212
Reston, VA 22091 (2 Copies)

Dr. Keith K. Nakanishi
Lawrence Livermore National Laboratory
L-025
P.O. Box 808
Livermore, CA 94550

Dr. Carl Newton
Los Alamos National Laboratory
P.O. Box 1663
Mail Stop C335, Group ESS-3
Los Alamos, NM 87545

Dr. Bao Nguyen
HQ AFTAC/TTR
Patrick AFB, FL 32925

Prof. John A. Orcutt
IGPP, A-025
Scripps Institute of Oceanography
University of California, San Diego
La Jolla, CA 92093

Prof. Jeffrey Park
Kline Geology Laboratory
P.O. Box 6666
New Haven, CT 06511-8130

Dr. Howard Patton
Lawrence Livermore National Laboratory
L-025
P.O. Box 808
Livermore, CA 94550

Dr. Frank Pilotte
HQ AFTAC/TT
Patrick AFB, FL 32925-6001

Dr. Jay J. Pulli
Radix Systems, Inc.
2 Taft Court, Suite 203
Rockville, MD 20850

Dr. Robert Reinke
ATTN: FCTVTD
Field Command
Defense Nuclear Agency
Kirtland AFB, NM 87115

Prof. Paul G. Richards
Lamont-Doherty Geological Observatory
of Columbia University
Palisades, NY 10964

Mr. Wilmer Rivers
Teledyne Geotech
314 Montgomery Street
Alexandria, VA 22314

Dr. George Rothe
HQ AFTAC/TTR
Patrick AFB, FL 32925-6001

Dr. Alan S. Ryall, Jr.
DARPA/NMRO
3701 North Fairfax Drive
Arlington, VA 22209-1714

Dr. Richard Sailor
TASC, Inc.
55 Walkers Brook Drive
Reading, MA 01867

Prof. Charles G. Sammis
Center for Earth Sciences
University of Southern California
University Park
Los Angeles, CA 90089-0741

Prof. Christopher H. Scholz
Lamont-Doherty Geological Observatory
of Columbia University
Palisades, CA 10964

Dr. Susan Schwartz
Institute of Tectonics
1156 High Street
Santa Cruz, CA 95064

Secretary of the Air Force
(SAFRD)
Washington, DC 20330

Office of the Secretary of Defense
DDR&E
Washington, DC 20330

Thomas J. Sereno, Jr.
Science Application Int'l Corp.
10260 Campus Point Drive
San Diego, CA 92121

Dr. Michael Shore
Defense Nuclear Agency/SPSS
6801 Telegraph Road
Alexandria, VA 22310

Dr. Matthew Sibol
Virginia Tech
Seismological Observatory
4044 Derring Hall
Blacksburg, VA 24061-0420

Prof. David G. Simpson
IRIS, Inc.
1616 North Fort Myer Drive
Suite 1400
Arlington, VA 22209

Donald L. Springer
Lawrence Livermore National Laboratory
L-025
P.O. Box 808
Livermore, CA 94550

Dr. Jeffrey Stevens
S-CUBED
A Division of Maxwell Laboratory
P.O. Box 1620
La Jolla, CA 92038-1620

Lt. Col. Jim Stobie
ATTN: AFOSR/NL
Bolling AFB
Washington, DC 20332-6448

Prof. Brian Stump
Institute for the Study of Earth & Man
Geophysical Laboratory
Southern Methodist University
Dallas, TX 75275

Prof. Jeremiah Sullivan
University of Illinois at Urbana-Champaign
Department of Physics
1110 West Green Street
Urbana, IL 61801

Prof. L. Sykes
Lamont-Doherty Geological Observatory
of Columbia University
Palisades, NY 10964

Dr. David Taylor
ENSCO, Inc.
445 Pineda Court
Melbourne, FL 32940

Dr. Steven R. Taylor
Los Alamos National Laboratory
P.O. Box 1663
Mail Stop C335
Los Alamos, NM 87545

Prof. Clifford Thurber
University of Wisconsin-Madison
Department of Geology & Geophysics
1215 West Dayton Street
Madison, WS 53706

Prof. M. Nafi Toksoz
Earth Resources Lab
Massachusetts Institute of Technology
42 Carleton Street
Cambridge, MA 02142

Dr. Larry Turnbull
CIA-OSWR/NED
Washington, DC 20505

Dr. Gregory van der Vink
IRIS, Inc.
16116 North Fort Myer Drive
Suite 1440
Arlington, VA 22209

Dr. Karl Veith
EG&G
5211 Auth Road
Suite 240
Suitland, MD 20746

Prof. Terry C. Wallace
Department of Geosciences
Building #77
University of Arizona
Tuscon, AZ 85721

Dr. Thomas Weaver
Los Alamos National Laboratory
P.O. Box 1663
Mail Stop C335
Los Alamos, NM 87545

Dr. William Wortman
Mission Research Corporation
8560 Cinderbed Road
Suite 700
Newington, VA 22122

Prof. Francis T. Wu
Department of Geological Sciences
State University of New York
at Binghamton
Vestal, NY 13901

AFTAC/CA
(STINFO)
Patrick AFB, FL 32925-6001

DARPA/PM
3701 North Fairfax Drive
Arlington, VA 22203-1714

DARPA/RMO/RETRIEVAL
3701 North Fairfax Drive
Arlington, VA 22203-1714

DARPA/RMO/SECURITY OFFICE
3701 North Fairfax Drive
Arlington, VA 2203-1714

HQ DNA
ATTN: Technical Library
Washington, DC 20305

Defense Intelligence Agency
Directorate for Scientific & Technical Intelligence
ATTN: DTIB
Washington, DC 20340-6158

Defense Technical Information Center
Cameron Station
Alexandria, VA 22314 (2 Copies)

TACTEC
Battelle Memorial Institute
505 King Avenue
Columbus, OH 43201 (Final Report)

Phillips Laboratory
ATTN: XPG
Hanscom AFB, MA 01731-5000

Phillips Laboratory
ATTN: GPE
Hanscom AFB, MA 01731-5000

Phillips Laboratory
ATTN: TSML
Hanscom AFB, MA 01731-5000

Phillips Laboratory
ATTN: SUL
Kirtland, NM 87117 (2 copies)

Dr. Michel Bouchon
I.R.I.G.M.-B.P. 68
38402 St. Martin D'Heres
Cedex, FRANCE

Dr. Michel Campillo
Observatoire de Grenoble
I.R.I.G.M.-B.P. 53
38041 Grenoble, FRANCE

Dr. Kin Yip Chun
Geophysics Division
Physics Department
University of Toronto
Ontario, CANADA

Prof. Hans-Peter Harjes
Institute for Geophysic
Ruhr University/Bochum
P.O. Box 102148
4630 Bochum 1, GERMANY

Prof. Eystein Husebye
NTNF/NORSAR
P.O. Box 51
N-2007 Kjeller, NORWAY

David Jepsen
Acting Head, Nuclear Monitoring Section
Bureau of Mineral Resources
Geology and Geophysics
G.P.O. Box 378, Canberra, AUSTRALIA

Ms. Eva Johannisson
Senior Research Officer
National Defense Research Inst.
P.O. Box 27322
S-102 54 Stockholm, SWEDEN

Dr. Peter Marshall
Procurement Executive
Ministry of Defense
Blacknest, Brimpton
Reading FG7-FRS, UNITED KINGDOM

Dr. Bernard Massinon, Dr. Pierre Mechler
Societe Radiomana
27 rue Claude Bernard
75005 Paris, FRANCE (2 Copies)

Dr. Svein Mykkeltveit
NTNT/NORSAR
P.O. Box 51
N-2007 Kjeller, NORWAY (3 Copies)

Prof. Keith Priestley
University of Cambridge
Bullard Labs, Dept. of Earth Sciences
Madingley Rise, Madingley Road
Cambridge CB3 OEZ, ENGLAND

Dr. Jorg Schlittenhardt
Federal Institute for Geosciences & Nat'l Res.
Postfach 510153
D-3000 Hannover 51, GERMANY

Dr. Johannes Schweitzer
Institute of Geophysics
Ruhr University/Bochum
P.O. Box 1102148
4360 Bochum 1, GERMANY